Integrated modeling of friction stir welding of 6xxx series Al alloys: Process, microstructure and properties

A. Simar, Y. Brechet, B. de Meester, A. Denquin, C. Gallais, T. Pardoen

Integrated modeling of friction stir welding of 6xxx series Al alloys: Process, microstructure and properties

A. Simar [a], Y. Bréchet [b], B. de Meester [a], A. Denquin [c], C. Gallais [c], T. Pardoen [a]

[a] *Institute of Mechanics, Materials and Civil Engineering, Université catholique de Louvain, B-1348 Louvain-la-Neuve, Belgium*
[b] *SIMaP/INP Grenoble, Domaine Universitaire, 1130 rue de la Piscine, B.P. 75, 38 402 Saint Martin d'Heres Cedex, France*
[c] *ONERA, BP72 – 29 avenue de la Division Leclerc, 92322 Chatillon Cedex, France*

Compared to most thermomechanical processing methods, friction stir welding (FSW) is a recent technique which has not yet reached full maturity. Nevertheless, owing to multiple intrinsic advantages, FSW has already replaced conventional welding methods in a variety of industrial applications especially for Al alloys. This provides the impetus for developing a methodology towards optimization, from process to performances, using the most advanced approach avail-able in materials science and thermomechanics. The aim is to obtain a guidance both for process fine tuning and for alloy design. Inte-grated modeling constitutes a way to accelerate the insertion of the process, especially regarding difficult applications where for instance ductility, fracture toughness, fatigue and/or stress corro-sion cracking are key issues. Hence, an integrated modeling frame-work devoted to the FSW of 6xxx series Al alloys has been established and applied to the 6005A and 6056 alloys. The suite of models involves an in-process temperature evolution model, a microstructure evolution model with an extension to heterogeneous precipitation, a microstructure based strength and strain hardening model, and a micro-mechanics based damage model. The presenta-tion of each model is supplemented by the coverage of relevant recent literature. The "model chain" is assessed towards a wide range of experimental data. The final objective is to present routes for the optimization of the FSW process using both experiments and models. Now, this strategy goes well beyond the case of FSW, illustrating the potential of chain models to support a "material by design approach" from process to performances.

1. Introduction

Light metallic alloys are facing a fierce competition against structural polymer-based composite materials in many structural applications, the most obvious being in aeronautical design. The search for lighter structure keeps motivating investigations towards the enhancement of specific material properties. If the mainstream effort in the case of Al alloys has long been based on the control of the microstructure to improve the yield stress, toughness, fatigue resistance and corrosion resistance

of the bulk, a modern approach must integrate also the primary and secondary manufacturing processes, like welding, within the material development strategy. The fact that "safety factors" associated with joining processes lead to significant limitations on the classical strengthening strategies has triggered a wide interest for a combined optimization of both alloy composition and welding process parameters. Along these lines, the limitations of classical arc welding or electron beam welding or even laser welding have generated research efforts for developing new innovative welding techniques. Friction stir welding (FSW) is a recent answer issued by the welding community to meet this need for more efficient processes providing high-quality joints. Nevertheless, partly due to the infancy of the process (patented in 1991 by TWI [1]), and in spite of numerous experimental and modeling studies, its optimization is still mainly based on trials and errors. The reason for the lack of a robust scientific methodology comes from the difficulties of modeling a process involving temperature variations, deformation, and microstructure evolutions being all spatially heterogeneous. The end users are looking for a systematic procedure through modeling and specific experiments. Among the key end-use properties, the ductility and fracture resistance of FSW joints, which are more difficult to address than the local hardness, have not yet been much covered. Recent progress towards physical, "microstructure based" damage models [2–8] has provided the impetus to transfer this knowledge to FSW.

Hence, the challenge is to develop an "integrated model" predicting the macroscopic properties of a joint (e.g. yield, fracture) as a function of alloy composition, thermodynamic features and process parameters in order to devise an optimization scheme both for the "alloy design" and for the process conditions. An "integrated model" procedure has the potential to significantly reduce (up to 50% according to Ref. [9]) the cost and duration of material and process development compared to a trial and error based approach. The first objective of this paper is to fill a gap between available computational tools and material models in order to provide an example of such an integrated stategy as applied to FSW.

In order to do so, a series of models must be developed, see Fig. 1. The thermomechanical history associated to the process is described by accounting for the heat transfer and for the material flow. In most materials, and particularly in age-hardened Al alloys, the thermal and strain history of the material affect the microstructure in the various regions of the weld. The evolution of the phases, precipitates, dislocations and other microstructural features has to be subsequently predicted. These microstructural evolutions inherently affect the mechanical properties in the processed region and hence the performances of the final product. As a matter of fact, the problem is even more complex.

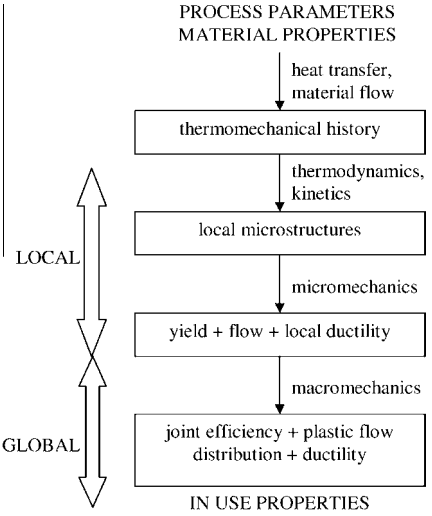

Fig. 1. Principle of the integrated process modelling.

Microstructural evolutions also affect the thermomechanical history leading to complex coupled effects. For instance, accounting for the change of the strength of the alloy when processed at high temperature can be important to correctly describe the flow of the material. Nevertheless, chaining simple models without true couplings often makes sense to reduce calculation time. Indeed, a full description of the entire complexity of the process leads to unreasonable calculation times, incompatible with an optimization procedure [9]. The thermal model used in this paper only treats pseudo steady-state conditions. The coupling of the microstructure evolution with the thermomechanical history and the complex material flow characteristic of the friction stir welding process are not taken into account. Furthermore, the damage model is not coupled to the finite element model predicting the deformation of the welded joint. Pardoen et al. [10] have shown that this simplification does not significantly affect the predictions of the fracture strain but very much reduces the calculation time. Nevertheless, owing to a direct and explicit connection with the physical mechanisms responsible for microstructure evolution and local plastic behavior, it will be shown that with a minimum number of experiments and a minimum level of complexity, one can reasonably well predict the effect of the process conditions on the properties of friction stir welds.

The model chain, as described in Fig. 1, requires some preliminary knowledge of the microstructure such as the initial distribution of the precipitates controlling the strength, the volume fraction and shape of the Fe-rich intermetallics controlling the damage development and the density of dispersoïds controlling the heterogeneous nucleation of precipitates and sometimes causing earlier fracture. These parameters are currently extracted experimentally. However, the initial state of the strengthening precipitates is affected by the solution heat treatment and by the pre-welding aging treatment. The size, composition and distribution of the dispersoïds and intermetallics are directly influenced by the upstream processes such as casting, homogenization and forming processes (e.g. extrusion and rolling). These processes and the associated internal evolution, such as recrystallization, are controlling the initial grain size depending on the alloy composition. An appropriate coupling with a solidification or a homogenization process model (such as Dons [11], Gandin et al. [12] and Grong and Shercliff [13]) would allow for an extra integration step which would be relevant when considering for instance recycled aluminum alloys with higher iron content. Similarly, in the present paper, we have neglected the grain size contribution to strengthening. This is a reasonable assumption for precipitation hardened materials. But, if one considers deformation hardened materials, such as 5xxx series Al alloys, the state of recrystallization in the nugget is an important feature and therefore a coupling with a dynamic recrystallization model at high strain rate, see e.g. Cram et al. [14], would be a necessary ingredient for those alloys. This illustrates that the model chain could be extended with models describing the upstream material processes.

Compared to earlier review papers [15–17] on FSW, the objective of this paper is to describe the progress in the field from the perspective of modeling each steps of the process with an emphasis, as explained above, on an integrated optimization of the mechanical properties in line of the contributions by Shercliff and Lovatt [18], Grong and Shercliff [13] and Kamp et al. [19]. The methodology is applied on 6005A and 6056 alloys welded with different equipments, having different microstructural evolutions and presenting different damage mechanisms. The 6005A alloy presents a low copper content compared to the 6056 which significantly affects the precipitation mechanisms. Furthermore, contrarily to the 6005A alloy, the damage mechanisms in the 6056 alloy involve the nucleation of secondary voids on dispersoïd particles, significantly decreasing the fracture strain. This ensures that the global procedure described in this paper is flexible enough and can be adapted to various specific situations.

The paper is structured as follows. In Section 2, the basis of the friction stir welding process is briefly described with reference to earlier review papers and literature on the topic. In Section 3, the thermal, microstructure evolution, yield strength, strain hardening, and damage models are presented, first by reviewing the different approaches proposed in the literature and then by particularizing to the specific choice made for the model chain. Furthermore, the parameters identification is addressed for the 6005A and 6056 welds. In Section 4, the model chain is integrated and assessed towards experimental data for the two alloys. The main differences between the two alloys are discussed. Finally, in Section 5, a process optimization analysis is performed using the full modeling chain.

2. The friction stir welding process

2.1. Principle of the friction stir welding process and its main features

Friction stir welding (FSW) is a solid state welding technique. The parts to be welded are rigidly clamped on a backing plate attached to the machine table. A rotating tool, composed of a threaded pin and a shoulder, is introduced into the material along the joint axis until the shoulder gets in contact with the upper surface of the plates. Heat generated by friction and deformation brings the material into a malleable state that promotes the forward displacement of the tool with the material flowing from the front to the back of the tool where it cools down, see Fig. 2. The weld is asymmetric since on one side of the weld, called the advancing side, the rotation of the tool is parallel to the advancing direction, while, on the other side, called the retreating side, the rotation is opposite to the direction of translation of the tool. The weld quality is very dependent on the welding parameters such as the speed, the advancing speed, the welding equipment (e.g. stiffness of the frame), and the tool geometry. Defects can be avoided owing to the presence of a thread or other features on the pin (see e.g. Ref. [20]).

Friction stir welding has been initially developed for welding Al alloys but other materials have been successfully joined with this process, such as copper, magnesium, titanium, thermo-plastics, steel and stainless steel (see references [175–232] of [15] and see also Nandan et al. [16]). Specific tooling made of very resistant materials is needed for welding higher melting point metals limiting up to now its industrial use. For instance, application to steel welding is a challenge, even though new solutions are under investigation [21,22]. Welding of dissimilar materials is a very attractive application of the FSW process. Efforts have been recently devoted to join different Al alloys [23–30] or Mg alloys [31]. The main problem for joining Al to steel is the formation of brittle intermetallic phase [32,33].

2.2. Microstructural zones in a friction stir weld

A FSW joint consists of the various zones represented in Fig. 3 involving different microstructures and mechanical properties. The heat affected zone (HAZ) is the most distant from the joint center line. It is not deformed during the process but the microstructure evolves due to the welding thermal cycles, influencing the mechanical properties. The thermo-mechanically affected zone (TMAZ) and the nugget are highly deformed by the material rotational flow. Contrarily to the TMAZ, the nugget is dynamically recrystallized [35,36]. Hence, the dislocation density in the nugget zone is low compared to the TMAZ [35,37–41]. The grains in the nugget are equiaxed with a much smaller size (several μm) than the base material. The grain size of the nugget has a second order effect on its hardness in age-hardenable Al alloys [39,42]. Under some welding conditions so-called onion rings are observed in the nugget (see Fig. 3).

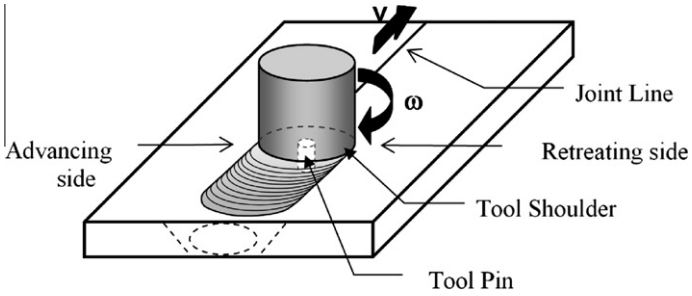

Fig. 2. Principle of the friction stir welding process (from Ref. [34]).

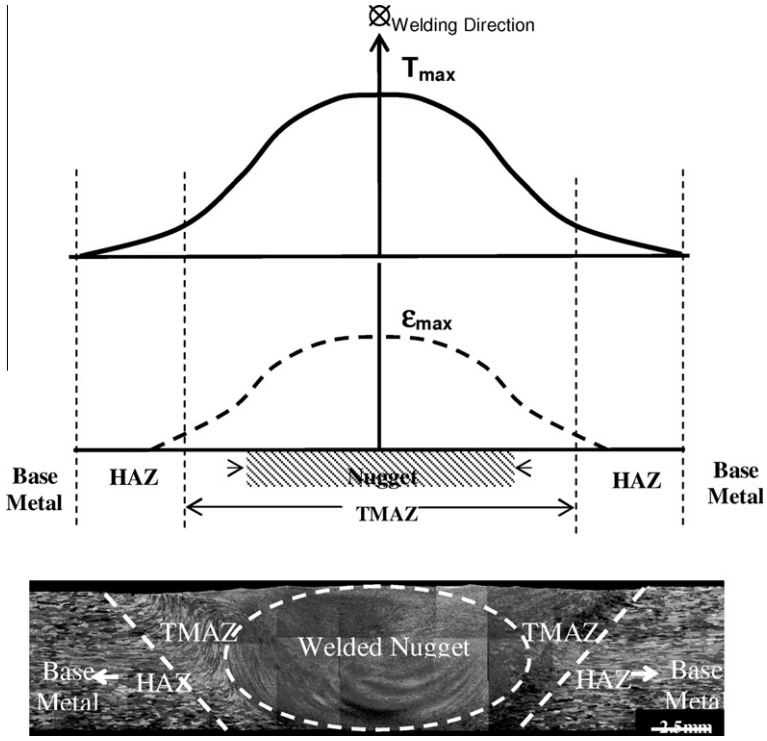

Fig. 3. Schematic of the temperature distribution, strain distribution and macrograph showing the microstructural zones in a friction stir weld (from Ref. [34]).

3. Individual model description and validation

3.1. Thermal model of the friction stir welding process

The local thermal history of welds plays a key role in controlling the microstructure evolution in friction stir welds. Indeed, the main contribution to hardening in age hardenable Al alloys is the strengthening by the nucleation and growth of nanosized precipitates. The mean size and size distribution of the precipitates are very much affected by the thermal cycles during the welding process. The thermal cycles in the process must thus be accurately predicted in order to capture the microstructural evolution in the various zones of the weld and the resulting impact on the weld mechanical properties. This is the first step of the integrated modeling procedure. In this section, an overview of literature on thermo-mechanical FSW process models is presented first. A specific thermal model of the process will be described next in details. Finally, the model parameters will be analyzed for an application to 6005A welds (performed at UCL-Belgium) and 6056 welds (performed at ONERA-Paris). Later, in Section 4.2.2, the model will be validated on measurements of temperature cycles during welding.

3.1.1. Overview of literature on thermo-mechanical process models

Modeling the FSW process is a complicated task since some of the physical mechanisms occurring during the process can hardly be fully quantified, in particular those concerning the contact conditions at the tool/workpiece interface, e.g. generation of heat and material sliding or not at that interface, and the heat transfer at workpiece/backing plate interface. Furthermore, there is no consensus on the type of law to be used for the constitutive behavior of the workpiece material at high temperatures and

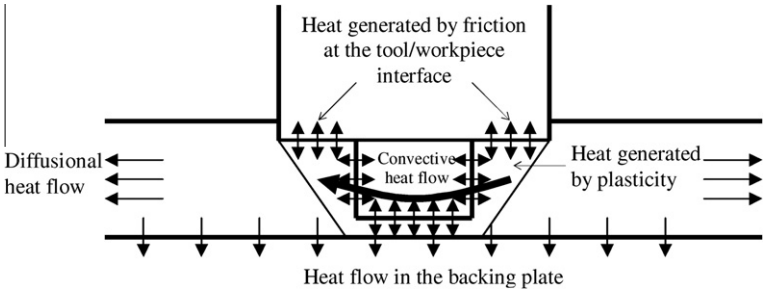

Fig. 4. Schematic of the heat generation and transfer in the friction stir welding process.

under high strain rates. This is why some early models were simply solving the heat transfer equation in order to estimate the temperature distribution, neglecting the material stirring. More sophisticated models are now available relying on three possible types of strategies: computational fluid dynamics, computational solid mechanics (also called thermomechanical models) or a combination of both types of models. As illustated in Fig. 4, the heat generation problem has two components: friction generated heat and bulk plasticity generated heat. The heat transfer has itself two contributions: diffusion and convection via material flow. Each model proposed in the literature is classified depending on the approximations made for dealing with the assumed dominant contributor to heat generation and heat flow.

3.1.1.1. Thermal models neglecting material flow. Early thermal models of the friction stir welding process neglected the intense material flow and assumed purely sliding frictional contact at the tool/workpiece interface [43–48]. By fitting experimental thermal cycles, Zahedul et al. [44] identified a low value for the friction coefficient leading to the conclusion that a purely frictional heating model was probably not adequate. Simar et al. [49] concluded also that the assumption of a purely frictional contact leads to an overestimation of the maximum temperature, above the melting point in Al alloy 6005A. Hence, the material flow involving a volume heat generation due to plastic deformation must be taken into account.

The generally accepted fact that friction stir welding is a solid-state welding process is sometimes artificially taken into account in the models. Frigaard et al. [50] limited the maximum temperature of their model to a value close to the eutectic temperature of the alloy by adapting the friction coefficient such as to prevent the rise of the temperature above the melting temperature. Song et al. [45] artificially set the heat generation term of the thermal equation to zero when the melting temperature was reached.

The problem of distributing the heat sources around the tool in simple thermal models, in order to take into account the power dissipated by friction and by material stirring, has been addressed in the literature in various ways. Shi et al. [51] distributed a total power input of 1600 W, obtained from direct torque measurement, between a surface heat source at the shoulder interface, involving 75% of the total power input, and a volume heat source inside the pin. Mc Cune et al. [52] proposed to reduce the contribution of the heat generation in the pin to 20% of the total power input in an application on thin Al sheets. The temperature measurements by Tang et al. [53] with a pinless tool gave only a 4% reduction of the maximum temperature leading to the conclusion that the pin has a minor influence on the heat input. Gallais et al. [54] performed similar tests but recorded the torque during the pinless tool experiment and concluded that only 17% of the heat generation during welding can be associated to the presence of the pin. Khandkar et al. [46] used the measured mechanical power as input to a FSW thermal model with surface heat sources distributed by assuming a uniform shear stress at the tool interfaces. Hamilton et al. [48,55] improved this model by accounting for the amount of slip at the tool/workpiece interface on the heat input based on an empirical relationship between the maximum temperature and the torque.

All these simple thermal models run very fast on a personal computer and predict relatively well the temperature fields for a wide variety of alloys welded under very different welding conditions. The major drawback of such models is the need for a calibration based on temperature measurements for every new conditions, or, sometimes for an experimental measurement of the torque or plunge force. Nevertheless, Ferro and Bonollo [56] developed a semi analytical model of the FSW process where the heat generation is not an input data. Generally, simple thermal models provide less accurate temperature predictions close to the stirred zone.

3.1.1.2. Models accounting for the convective heat flow. The problem of simulating the plastic flow and accompanying heat generation is extremely complex. In particular, at the strain rates of interest (of the order of 1000 s^{-1} according to Ref. [57] and 10 s^{-1} according to Ref. [58]), the proper constitutive relationships are not precisely known. Indeed, the plastic response rely on strain rate and on temperature dependent internal variables characterizing the hardening and softening behavior associated with precipitate dissolution, recrystallization and recovery. The effect of the material convection on the heat transfer can be accounted for by estimating the velocity field. Schmidt et al. [59–61], Heurtier et al. [62], Simar et al. [63] and Jacquin et al. [64] proposed simple distributions of material velocity fields in order to account for the effect of material convection on the temperature distribution. This kind of models remains very simple and does not require fully coupled simulations. As a consequence of not explicitly accounting for the plastic dissipation associated to the material flow, these models generally rely on a measured power input or plunge force, see discussion in Schmidt and Hattel [57]. The model by Jacquin et al. [64] provides a direct prediction of the power input but, consequently, relies on the quality of constitutive laws to describe the heat input.

3.1.1.3. Models accounting for material flow with coupling. Computational fluid dynamics models, based on an Eulerian formulation, have been developed by Bendzsak et al. [65], Shercliff and Colegrove [66], Ulysse [67], Seidel et al. [68], Askari et al. [69], Colegrove et al. [70–75], Nandan et al. [76], Bastier et al. [77,78], De Vuyst et al. [79] and Kim et al. [80]. These models assume that the heat input is due to viscous dissipation. An equivalent viscosity is generally extracted from experimental data such as stress versus strain rate and temperature results, see Refs. [73–75,79]. In the stepwise approach proposed by Bastier et al. [77,78], a fluid dynamics model is used first to determine the thermal and velocity fields and a solid mechanics model calculates next the strain and stress fields. This model predicts the input power as well as the residual stresses which is of course not possible with a pure fluid dynamics model.

The fluid dynamics models have to prescribe the tool/workpiece interface conditions assuming either full sticking [65,68,69,74] or sticking/sliding conditions at the tool/workpiece interface [77,76]. For instance, Bastier et al. [77] found that a material velocity at the tool/workpiece interface equal to only 1% of the tool velocity was giving the best results when comparing the predicted to the measured thermal fields.

Xu et al. [81], Fourment et al. [82–84], Buffa et al. [85], Schmidt and Hattel [86,87] and Zhang et al. [88] developed models based on solid mechanics (Lagrangian or Arbitrary Lagrangian Eulerian, ALE, formulations), which also provide an insight into the material flow during the process. The ALE formulation avoids the occurence of too large mesh distortions when modeling the material flow around the pin [81–84,86,87]. Nevertheless, still the major drawback of solid mechanics models is the large mesh distortions due to the large strains in the material during the welding process. Therefore, Tartakovsky et al. [89] proposed a smooth particle hydrodynamics (SPH) model, i.e. a Lagrangian particle method. The SPH models are particularly well adapted to the modeling of dissimilar friction stir welding.

Concerning the constitutive equations describing the material flow behavior, Ulysse [67], Colegrove et al. [74,75] and Nandan et al. [76] used an inverse hyperbolic sine function of the Zener-Hollomon parameter (law of Sheppard and Wright [90]) to express the strain rate and temperature dependence of the flow stress. The Johnson and Cook law, which is based on a linear dependence of the flow stress on the strain and on a logarithmic dependence on the strain rate, has often been applied as well (see e.g. Ref. [69,73,86,87]). The tool/workpiece interface can be treated by introducing an evolving friction law in order to take into account both the Coulomb and the limit of the linear friction (Tresca

limitation) at the tool/workpiece interface (see Ref. [88] for more details). Finally the loss of material resistance at the solidus temperature is sometimes explicitly accounted for in the constitutive models. Seidel et al. [68] and Colegrove et al. [75] decrease the viscosity in their fluid dynamics model when reaching the solidus temperature.

3.1.1.4. Contact conditions at the workpiece/backing plate interface. The loss of heat through the contact interface between the bottom of the workpiece and the backing plate has been introduced in numerical models following different approaches. Either the backing plate is not explicitly modeled and a prescribed convection coefficient is introduced under the workpiece, or the backing plate is explicitly modeled and contact conductances have to be evaluated.

When the backing plate is not explicitly modeled, the heat loss in the backing plate can be accounted for by introducing an equivalent convection coefficient h_{back} under the workpiece [43–45,82,83]. Chao et al. [43] proposed a value of 200 W/m^2 K for the bottom convection coefficient by comparing the results of a 3D finite element model to temperature measurements on 6061-T6 Al welds. Fourment et al. [82,83] used the same value for the bottom convection coefficient. Zahedul et al. [44] compared four different bottom convection coefficients and concluded that a high value equal to 4000 W/m^2 K leads to underestimating the maximum temperature but that adiabatic conditions, i.e. h_{back} = 0 W/m^2 K, lead to maximum temperatures far above the melting point. An intermediate value of h_{back} = 1000 W/m^2 K was thus chosen. Soundararajan et al. [47] implemented a contact conductance with the backing plate which is a function of the contact stress.

Some authors introduced a backing plate as part of the model which requires introducing a contact condition between the workpiece and the backing plate. Colegrove et al. [91] proposed a contact conductance equal to 1000 W/m^2 K between the workpiece and the backing plate. The bottom of the backing plate was set to a temperature of 300 K. In another study, Colegrove et al. [72] proposed to keep the same contact conductance over the whole interface surface except under the tool region where a perfect contact is introduced. Khandkar et al. [46] introduced an annular distribution of the contact conductance that simulates the heat loss in the backing plate when the contact pressure enhances the heat transfer. The contact between the workpiece and the backing plate in front of the tool is probably not perfect as a result of the backward inclination of the tool. Shi et al. [51] proposed a temperature-dependent contact conductivity between the workpiece and the backing plate. De Vuyst et al. [92] showed that such a variation of the contact conductance with temperature ensures a good correlation between experimental and modeling time–temperature curves for the friction stir welded 6005A-T6 and 2024-T3 Al alloys. More recently, De Vuyst et al. [79] proposed the use of a pressure dependent contact condition at the tool-workpiece interface. Simar et al. [49,63] proposed a distribution of the contact conductivity that will be described in Section 3.1.2.

3.1.2. Thermal model for an integrated process model

The thermal model is the first ingredient of the integrated approach. It is kept relatively simple in order to limit computation time. Earlier investigations [19,54,62] have proved that simplifications in the thermal model are possible and do not significantly affect the predictions of the mechanical properties of the weld. The main interest here is to quantify the temperature cycles, which affect microstructure evolution and hardening in age hardenable alloys. A simple velocity field is introduced, in order to take into account the effect of material flow on the difference in temperature between the advancing and the retreating side of the welds and on the convective heat flow. The model is purely thermal with no mechanical coupling; hence the residual stresses are not predicted. The step towards a mechanical coupling, as, for instance, in Bastier et al. [78], is relatively direct to make if reliable constitutive laws can be provided.

A pseudo steady state heat transfer problem is solved using the general-purpose finite element code ABAQUS [93]. The mesh consists of hexahedrons with a high density in the near tool region. The model is sufficiently long so that the thermal field around the tool is representative of steady state conditions. Room temperature is imposed upstream. Adiabatic conditions are enforced on the top and side surfaces. The effect of convection at these surfaces on the temperature distribution were found to be negligible. The model takes into account the heat loss through the backing plate by meshing a steel block under the workpiece. Room temperature is also imposed at the bottom of

the backing plate. The contact conditions between the workpiece and the backing plate are explained later. The pin was not explicitly modeled in order to avoid discontinuities in the material flow field.

3.1.2.1. Heat dissipated by friction at the tool/workpiece interface – surface heat sources. The heat generated by friction between sliding surfaces q_S (W/m^2) is equal to the work done by the interfacial shear stress $\tau_{contact}$:

$$q_S = \tau_{contact}(v_{tool} - v_{material}), \tag{1}$$

where v_{tool} is the tool velocity at the tool/workpiece interface and $v_{material}$ is the material velocity at the tool/workpiece interface. The tool velocity can be decomposed into the rotational velocity ωr_a and the velocity associated to the linear movement, where r_a is the radial distance from the tool axis. In most practical cases, the latter can be neglected. The material velocity at the tool/workpiece interface is unknown. For simplicity, the material velocity relative to the tool is introduced in the model as a fraction δ of the velocity of the tool at the tool/workpiece interface. The surface heat source due to friction at the tool/workpiece interface is expressed as

$$q_S = \tau_{contact}\omega r_a(1-\delta), \tag{2}$$

with $0 \leqslant \delta \leqslant 1$. The value of δ characterizes the type of contact at the tool/workpiece interface:

- if $\delta = 0$, the contact corresponds to perfect sliding conditions,
- if $\delta = 1$, the contact corresponds to perfect sticking conditions.

The total power dissipated at the tool/workpiece interface Q_S (W) is divided in three parts corresponding to the different surfaces of the tool (see Fig. 5): the shoulder (assumed to be a plane annular disk with an external radius equal to the shoulder radius r_o and an inner radius equal to the radius of the tool pin r_i), the lateral surface of the pin (assumed to be a cylinder with a radius equal to the tool pin radius r_i and a height equal to the height of the tool pin h_p) and the surface of the tool pin tip (assumed to be a plane disk with a radius equal to the tool pin radius r_i), i.e.

$$Q_S = Q_{S,shoulder} + Q_{S,pin} + Q_{S,pintip}, \tag{3}$$

with

$$\begin{aligned}
Q_{S,shoulder} &= \int_0^{2\pi}\int_{r_i}^{r_o} \tau_{contact}\omega r_a(1-\delta) r_a d\theta_a dr_a,\\
Q_{S,pin} &= \int_0^{2\pi}\int_0^{h_p} \tau_{contact}\omega r_a(1-\delta) r_a d\theta_a dz,\\
Q_{S,pintip} &= \int_0^{2\pi}\int_0^{r_i} \tau_{contact}\omega r_a(1-\delta) r_a d\theta_a dr_a.
\end{aligned} \tag{4}$$

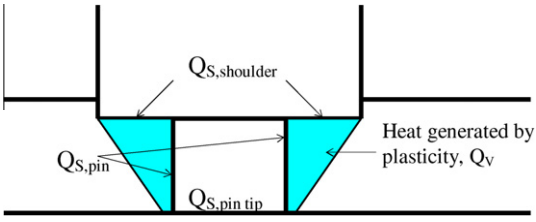

Fig. 5. Schematic of the heat generation by friction at the tool/workpiece interface and by plastic deformation in the TMAZ.

The assumption that $\tau_{contact}$ and δ are constant along the tool/workpiece interfaces leads to

$$\begin{aligned} Q_{S,shoulder} &= \tau_{contact}\omega(1-\delta)\frac{2}{3}\pi(r_o^3 - r_i^3), \\ Q_{S,pin} &= \tau_{contact}\omega(1-\delta)2\pi r_i^2 h_p, \\ Q_{S,pintip} &= \tau_{contact}\omega(1-\delta)\frac{2}{3}\pi r_i^3. \end{aligned} \tag{5}$$

The total power dissipated at the tool/workpiece interfaces is therefore equal to

$$Q_S = \tau_{contact}\omega(1-\delta)\frac{2}{3}\pi(r_o^3 + 3r_i^2 h_p). \tag{6}$$

The relative proportions of the friction heat dissipated on the shoulder, the pin and the tip of the tool are named respectively $C_{shoulder}$, C_{pin} and $C_{pin\ tip}$ and are given by Eqs. (7)–(9), respectively:

$$C_{shoulder} = \frac{Q_{S,shoulder}}{Q_S} = \frac{r_o^3 - r_i^3}{r_o^3 + 3r_i^2 h_p}, \tag{7}$$

$$C_{pin} = \frac{Q_{S,pin}}{Q_S} = \frac{3r_i^2 h_p}{r_o^3 + 3r_i^2 h_p}, \tag{8}$$

$$C_{pintip} = \frac{Q_{S,pintip}}{Q_S} = \frac{r_i^3}{r_o^3 + 3r_i^2 h_p}. \tag{9}$$

If the surface heat sources are distributed over the shoulder and the tip of the pin with a linear variation along the radius:

$$q_{S,shoulder} = \frac{C_{shoulder} Q_S r_a}{\frac{2}{3}\pi\left(r_o^3 - r_i^3\right)}, \tag{10}$$

with $r_i \leqslant r_a \leqslant r_o$ and $z = 0$,

$$q_{S,pin} = \frac{C_{pin} Q_S r_a}{\frac{2}{3}\pi r_i^3}, \tag{11}$$

with $r_a \leqslant r_i$ and $z = h_p$, and along the lateral surface of the tool pin:

$$q_{S,pintip} = \frac{C_{pintip} Q_S}{2\pi r_i h_p}, \tag{12}$$

with $0 \leqslant z \leqslant h_p$ and $r_a = r_i$.

3.1.2.2. Heat dissipated by plastic deformation – volume heat sources. Heat is also dissipated in the volume of the material by plastic deformation during the stirring process. The corresponding volume heat sources per unit volume q_V (W/m^3) are related to the plastic work by:

$$q_V = \zeta \dot{\varepsilon}_{ij}^p \sigma_{ij}, \tag{13}$$

where $\dot{\varepsilon}_{ij}^p$ and σ_{ij} are, respectively, the components of the plastic strain rate tensor and the Cauchy stress tensor and ζ is a parameter ranging between 0.8 and 0.99 [94], a small part of the energy being stored elastically in the material in the form of defects. A purely phenomenological approach is used in the present model. Little can be presumed at first concerning the location and the intensity of the heat dissipation through plastic deformation during FSW, except that it occurs in the TMAZ as confirmed experimentally and agreed upon in the literature. Dong et al. [95] concluded from their models that plastic slip at the surface due to mechanical interactions between the tool and the base material correlates with the friction stir weld profile obtained by macrographs. Lambrakos et al. [96] stated that there is a strong correlation between the physical shape of the stirred region and the distribution of volumic heat generation during the stirring process. The thermomechanical model of Askari et al.

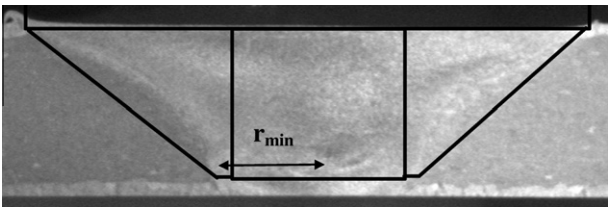

Fig. 6. Shape of the TMAZ and definition of r_{min}.

[69] showed that the deformed region is confined to the area immediately surrounding the pin, just under the shoulder. The deformation of the material is very large close to the friction stir welding tool but, due to heating, the flow stress is also the lowest. Conversely, away from the tool, the deformation is smaller but the material flow stress is higher, the temperature being lower.

In the absence of any other relevant information, an uniform distribution of the volume heat sources q_V resulting from plastic deformation in the TMAZ will be assumed. The TMAZ is assumed to have a trapezoidal shape (see Fig. 5). The total heat power dissipated through plastic deformation is imposed:

$$Q_V = q_V V_p, \tag{14}$$

where V_p (m^3) is the volume of the *TMAZ* and Q_V (W) is the volume heat source power.

The volume V_p of the TMAZ where plastic deformation takes place during FSW has been determined as a trapezoid from macrographic observations on a transverse section, see Fig. 6. The value of r_{min} (defined on Fig. 6) is chosen as $r_i + 0.5$ mm and assumed to be independent of the welding parameters.

3.1.2.3. Distribution of mechanical power between volume and surface heat sources. The total power dissipated by friction and plastic deformation during welding P_{in} can be calculated from the measurements of the force and of the torque. The power is almost entirely converted into heat. The energy stored in the material in the form of dislocations and other microstructural defects such as new grain boundaries for instance is usually less than 10%. The portion of the power lost within the tool was found to be only 5% of the total mechanical power and weakly dependent on the welding parameters [49]. The total power, reduced by this heat loss into the tool, is equal to the sum of the surface heat source and the volume heat source:

$$\eta P = P_{in} = Q_S + Q_V. \tag{15}$$

where η is the factor accounting for the power lost in the tool $\eta \approx 0.95$ [49]. The relative importance of Q_V and Q_S is unknown. In the present study, a parameter γ is introduced for that purpose:

$$\begin{aligned} Q_V &= \gamma P_{in}, \\ Q_S &= (1-\gamma) P_{in}. \end{aligned} \tag{16}$$

3.1.2.4. Material convection around the friction stir welding tool. A simple model for the velocity field around the tool is proposed in order to account for the effect of material convection on the heat flow. Material flow is considered only in the TMAZ and weld nugget. The local circumferential velocity caused by the shoulder increases with increasing distance from the tool axis and decreases with increasing depth from the tool shoulder. The local circumferential velocity due to the pin decreases with increasing distance from the tool axis. Fig. 7 represents the assumed velocity field. The parameter δ was defined previously as the ratio of the material velocity on the tool velocity at the material/tool interface (see Eq. (2)). Note that such a simple model for the circumferential velocity field introduces a discontinuity in the velocity at the outer radius of the shoulder.

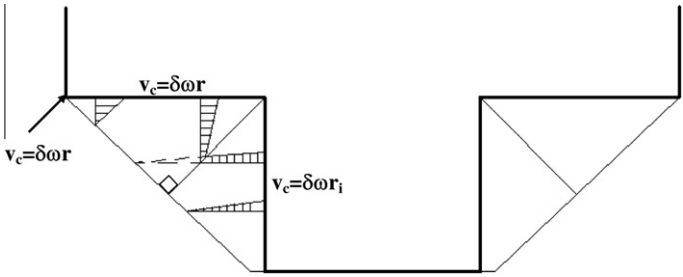

Fig. 7. Simple model of the circumferential velocity field.

The simple description of the heat generation and material flow proposed here is good enough considering that a more accurate distribution of the heat sources has only a minor effect on the temperature field away from this heat source. It will be shown later on that, in sound welds, fracture occurs in the heat affected zone of the weld, i.e. away from the weld center. Hence, the region of the nugget for which the heat generation distribution is important, is of limited relevance when addressing the mechanical behavior of the weld as a whole.

3.1.2.5. Contact condition at the workpiece/backing plate interface. The contact conditions between the workpiece and the backing plate constitute a critical ingredient in order to generate reliable temperature predictions. The contact under the pin is chosen to be perfect. The contact conductance under the shoulder CC_A ($W/m^2\,K$) is not as good. A good contact condition under the tool is motivated by experimental observations: the high pressure under the pin and in the surrounding leads to an indentation of the upper surface of the backing plate along a width approximately equal to the diameter of the tool shoulder, justifying very good contact. The indentation is more pronounced under the pin region. At the back of the tool, the contact is not as good as under the pin and very dependent on the experimental setup. Therefore a contact conductance parameter CC_B is introduced behind the tool. This parameter has been adapted for the two experimental setup addressed later. The value of parameter CC_A was identified based on the maximum temperature while the value of CC_B was identified based on the measured cooling rates [63]. Note that these parameters should ideally be calibrated based on temperature measurements in the backing plate right under the workpiece surface. Fig. 8 pictures the different contact conditions. The different contact conductances are introduced in the FE code by artificially inserting a material layer of 0.2 mm thickness between the workpiece and the backing plate, with a thermal conductivity equal to the chosen contact conductance multiplied by the layer thickness.

3.1.2.6. Model parameters. The various welds addressed in order to illustrate the integrated modeling approach were performed on a HERMLE 3-axis CNC milling machine at UCL-Belgium for the 6005A welds and on a PowerStir 315 (Smart Technology) dedicated FSW machine at ONERA-France for the 6056 welds. The 6005A welds were obtained using a simple threaded tool while the 6056 welds were

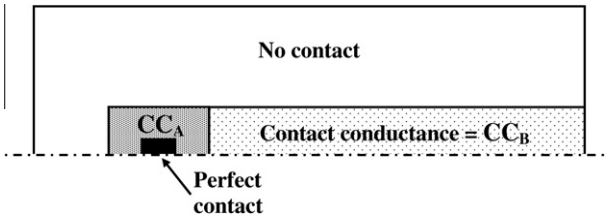

Fig. 8. Contact conditions between the workpiece and the backing plate (sketch not to scale) [63].

generated with a triflute^{TM} tool. The 6005A welds were produced with an advancing speed ranging from 50 mm/min to 1000 mm/min and a rotational speed ranging from 500 rpm to 1500 rpm. The 6056 welds involved an advancing speed ranging from 1100 mm/min to 1700 mm/min and a rotational speed ranging from 1100 rpm to 1700 rpm. Table 1 presents the model parameters for the series of welds performed on the 6005A alloy and on the 6056 alloy, from Simar et al. [49,63]. The values of the parameters γ and δ, equal to respectively 0.2 and 1, have been identified using an optimization procedure based on a variety of welding conditions for the 6005A welds [63]. It is reasonable for low rotational speed to consider sticking conditions (i.e. $\delta = 1$) as evidenced from thermomechanical modeling, see Schmidt et al. [86]. This assumption requires further assessment for higher rotational speeds at which partial sticking is probably taking place. The parameter γ controls the proportion of volume to surface heat source. The small value proposed in Table 1 (i.e. $\gamma = 0.2$) expresses that heat is mainly generated at the interface with the shoulder but, since the tool is assumed to be sticking, it should be interpreted as an indication that heat is generated within a small layer under the shoulder involving high shear strains. Table 2 presents the thermal properties as a function of temperature for the 6005A alloy. The main dimensions of the region represented by the finite element model is also given in Table 1. The backing plate in the 6005A welds consists of a 80 mm thick high carbon steel plate while the 6056 welds were performed using a 12 mm thick stainless steel plate on top of another

Table 1
Parameters of the thermal model.

Parameter	Symbol	Value 6005A welds	Value 6056 welds
Density of Al	ρ_a	Table 2	2710 (kg/m^3) [97]
Specific heat of Al	cp	Table 2	890(J/kg K) [97]
Thermal conductivity of Al	λ	Table 2	177 (W/mK) [97]
Shoulder radius	r_o	10 mm	11.25 mm
Pin radius	r_i	3.5 mm	5 mm
Plate thickness	h_p	6 mm	6 mm
Thickness of backing plate	h_B	80 mm	12 mm
Material of backing plate		High carbon steel	Stainless steel
ρ_a of backing plate		7700 (kg/m^3) [98]	7700 (kg/m^3) [98]
cp of backing plate		460 (J/kg K) [98]	460 (J/kg K) [98]
$\lambda$of backing plate		47 (W/mK) [98]	21 (W/mK) [98]
TMAZ shape parameter	r_{min}	r_i + 0.5 mm	r_i + 0.5 mm
Efficiency	η	0.95	0.95
Contact conductivity under the tool	CC_A	100 kW/m^2 K	5 kW/m^2 K
Contact conductivity at the back of the tool	CC_B	3 kW/m^2 K	5 kW/m^2 K
Q_u/P_{in}	γ	0.2	0.2
$v_{material}/v_{tool}$	δ	1	1

Table 2
Thermal properties used for the 6005A alloy as a function of temperature [49].

Temperature, T (°C)	Density, ρ_a (kg/m^3)	Specific heat, cp (J/kg K)	Thermal conductivity, λ (W/mK)
25	2680	–	–
50	2680	920	206.6
100	2670	930	208.3
150	2660	950	210.3
200	2650	970	210.3
250	2630	990	210.9
300	2620	1010	208.6
350	2610	1020	205.6
400	2600	1040	201.9
450	2590	1060	197.5
500	2580	1080	190.0
550	–	1110	182.8

steel clamping device. The steel clamping device is not taken into account in the model. The differences in the backing plate geometry and material might explain the difference in the parameters CC_A needed to correctly capture the temperature histories for the 6056 welds performed at ONERA-France compared to the 6005A welds performed at UCL-Belgium.

In Section 4.2.2, the thermal model predictions will be assessed towards experimental results on 6005A-T6 and 6056-T78 welds. Torque measurements made through a rotating dynamometer and temperature measurements by means of thermocouples inserted at various distances from the weld-line were systematically performed. The thermal model requires the total power P as input data. The total power is equal to the measured torque (expressed in Nm) multiplied by the rotational speed (expressed in s^{-1}).

3.2. Microstructure evolution in 6xxx series Al alloys

The Al alloys of the 6xxx series are age-hardenable, and the microstructure of these alloys can thus evolve during the welding process. The prediction of these evolutions requires a good knowledge of the precipitation sequence and associated thermodynamic driving and resistive forces. The precipitation sequence can include complex ternary or quaternary phases and the competition between various precipitation sites. Furthermore, microstructure evolution models of welds require, as an input, a reliable description of the thermal cycles. The thermal cycles can be predicted by the thermal model described in Section 3.1.2. The thermal cycles are profoundly anisothermal, hence the microstructure evolution model must be able to account for complex temperature histories. In this section, the precipitation sequence in 6xxx series Al alloys is described first. A literature review on the available microstructure evolution models for age-hardenable Al alloys is presented in a second section. Finally, the specific precipitation model selected for the integrated modeling chain is described in details as well as the model parameters identified for the Al alloys 6005A and 6056. Later, in Section 4.2.3, the model will be validated based on transmission electron microscopy (TEM) observations and differential scanning calorimetry (DSC) measurements performed on 6005A-T6 and 6056-T78 welds.

3.2.1. Hardening precipitation in 6xxx series Al alloys

6xxx series Al alloys are age hardenable alloys with magnesium and silicon as main alloying elements. Usual states of 6xxx series alloy delivery involve:

- T4 state: solution treated, quenched and naturally aged at room temperature; this state offers a good formability at the expense of a relatively low strength [99];
- T6 state: solution treated, quenched and artificial aged to peak strength;
- T78 state: slightly over-aged material, offers better corrosion properties for high Cu content alloys.

The decomposition sequence for quasi-binary Al–Mg_2Si compositions is the following: [100–102,99,103] (sss = supersaturated solid solution)

$$\text{sss} \rightarrow \text{clusters/GP zones} \rightarrow \beta'' \rightarrow \beta' \rightarrow \beta\text{-}Mg_2Si.$$

Copper addition or excess Si (Si > 1%) promotes the refinement of the size of the Mg_2Si particles and additional hardening precipitation. In alloys containing Cu, metastable versions of the quaternary Q phase $Al_5Cu_2Mg_8Si_6$ (also named B or λ) are reported to precipitate and more complex precipitation sequences have been proposed [104–106]. Another Q-like phase can also appear, presumably under a metastable isomorphous form (named M or type C), during over-aging of Si rich (Si > 1%) ternary Al–Mg–Si alloys [107]: this last result strongly supports the suggestion that the formation of the Q phase is also favored in overaged Si rich quaternary alloys, which is beneficial for desensitization to intergranular corrosion [108].

Miao and Laughlin [104] and Esmaeili et al. [105] demonstrated that the hardening β'' phase can be considered as a precursor of both β and Q phases in AlMgSi alloys containing Cu. The generally accepted precipitation sequence is therefore the following [54,104–106]

$$\text{sss} \rightarrow \text{clusters/GP zones} \rightarrow \beta'' \rightarrow \beta \text{ and/or Q } \rightarrow \beta\text{-}Mg_2Si + \text{Q-}Al_5Cu_2Mg_8Si_6.$$

The clusters or Guinier Preston (GP) zones are produced during low temperature artificial aging or natural aging at room temperature [109–111]. These small precipitates provide limited hardening. The β'' are fully coherent, needle shaped, precipitates lying along the $[100]_{Al}$ directions with a monoclinic crystallographic structure [99,103]. They are formed, in particular, during the artificial T6 heat treatment and are responsible for the peak hardness of ternary Al–Mg–Si alloys when reaching the optimum size (10–15 nm long in the 6061 Al alloy [102]). The composition of the β'' is probably Mg_5Si_6 [112], but may vary with alloy composition [113]. Over-aged conditions favor the appearance of the β' and Q phases, depending on the alloy composition. These precipitates are semi-coherent rod-like precipitates lying along the $[100]_{Al}$ directions [103], with a hexagonal structure. No definitive agreement exists on their composition which probably is $Mg_{1.7}Si$ [114] or $Mg_{0.44}Si$ [115]. Compared to the β'' precipitates, the β' have a much smaller hardening ability [103]. Q-$Al_5Cu_2Mg_8Si_6$ precipitates have a hexagonal crystal structure and form lath-like structures with the long direction lying along the $[100]_{Al}$ directions [106]. The β-Mg_2Si phase is formed by heterogeneous precipitation [116,117] at high temperature and presents a plate or platelets like structure lying on the $\{100\}_{Al}$ plane. It is worth mentioning that the concentration of alloying elements plays a major role on the quench sensitivity of a particular alloy, hence on its heterogeneous precipitation potential during welding. In particular, regarding the alloys specifically addressed in this paper, the 6005A has a limited amount of alloying elements, leading to homogeneous precipitation within the matrix [42]. Conversely, the 6056 alloy has a higher content of alloying elements and the precipitation is more heterogeneous, taking place also on dislocations and on dispersoïds[54,118]. This justifies the interest for addressing these two alloys in parallel.

Alloying elements can be also present as micro-constituents under the form of compounds which do not contribute to strengthening. These coarse intermetallic particles, usually in the 1–10 μm range, are formed during ingot solidification or during subsequent processing steps. Either because of an intrinsic brittleness or because of a lack of coherency with the matrix, these particles will be at the origin of damage initiation by the nucleation of small internal voids, which, under the effect of stresses, enlarge and develop into cracks (see Section 3.4.1). Two types of coarse second phases are observed in 6xxx series alloys: Al-Fe-Mn-Si type and Mg_2Si particles. Only the Mg_2Si, which dissolve at around 450–500 °C [101,103], can be affected by the thermal history within the TMAZ and within the weld nugget. The Al-Fe-Mn-Si particles can be broken into small parts by the stirring process, but the volume fraction should, in principle, be preserved [34,119] except if partial dissolution occurs, which is unlikely considering the thermodynamical stability of Al-Fe-Mn-Si type particles.

Smaller, submicron particles or dispersoïds are intermetallic compounds containing transition metals such as Mn, Cr or Zr. These particles retard recrystallization and grain growth [120,121] and may be active for heterogeneous precipitation [54], but can also constitute additional nucleation sites for a second population of voids (see Section 3.4.1).

3.2.2. Literature review on microstructure evolution models

Many types of models are available for modeling the precipitation evolution taking place during non-isothermal processes in metallic alloys. Analytical "internal variable" models involve only a simple numerical integration of the thermal cycles. The numerical "size class" models are more complex to implement especially if the precipitation sequence and composition of precipitates is accounted for. Finally, the Monte Carlo type models, involving atomistic calculations, are the most sophisticated. The model used in this work enters in the "size class" category; which will be described in more details in Section 3.2.3.

3.2.2.1. Internal variable approach. Many models for microstructure evolution in Al alloys have been proposed in the literature based on analytical expressions [122–135], as described in details in the review paper by Grong and Shercliff [13]. These analytical models use the Johnson-Mehl, Avrami, Kolmogorov (JMAK) formalism for the nucleation and growth of the precipitates and the Whelan formalism (i.e. see later Eq. (17), when neglecting the transient part) for the dissolution process. These models predict the evolution of the average volume fraction of precipitates relative to a reference volume fraction, generally the peak volume fraction. When expressed in an isokinetic manner [13,136],

application to non-isothermal heat treatments is possible through discretizing to infinitesimal steps of isothermal heat treatments [124–126,128]. When considering a welding process, the evolution of hardness with the heat treatment time or with the distance from the weldline is linearly related to the relative volume fraction [124,125,137]. The Liftshitz–Sloyozov–Wagner (LSW) formalism can be used to describe the coarsening kinetics [13]. A strong assumption in the LSW formalism is that no solute is lost in the surrounding matrix, i.e. the volume fraction of precipitates is assumed constant. This hypothesis is valid only if the maximum temperature reached is always far from the solvus temperature which is generally not true for welding processes. In these models, the nucleation, growth and coarsening of precipitates are not treated simultaneously.

3.2.2.2. Size class approach. More recently, Wagner and Kampmann [138] developed a numerical model which has been generalized to finite differences and extensively used to describe microstructural evolution in Al alloys [19,42,54,133,139–153]. These models describe the growth and dissolution of precipitates with the same kinetic equations. The coarsening stage arises naturally except in the study by Deschamps et al. [139] where the transition to the coarsening stage is explicitly modeled. Furthermore, the nucleation stage can be considered by increasing the precipitate density in the appropriate size class, as treated later with Eq. (31). This is essential to describe non-isothermal heat treatments, like in welding processes, where precipitates nucleated during one time step might dissolve after due to the variation of the thermodynamic parameters with temperature. Hence, all the mechanisms involved in the microstructure evolution simultaneously play a role in the final precipitate size distribution. Furthermore, in industrial heat treated age hardenable Al alloys, the precipitate size distribution needs to be explicitly modeled due to the interaction between different families of precipitates of different sizes that form at various temperatures (e.g. in 6xxx series GP zones, β'', β' and Q phases). The size class approach has been applied to the modeling of the microstructure evolution in welds [140–142,146,149]. The main drawback of these models is the need for a detailed description of the initial precipitate size distribution and for information about the precipitation sequence and relevant thermodynamic parameters.

The model initially proposed by Wagner and Kampmann [138] has been extended to account for several physical mechanisms associated to the precipitation in age hardenable Al alloys, following different lines:

- The heterogeneous precipitation of the hardening phases has been explicitly accounted for in studies dealing with the 6xxx series [54,142] and the 7xxx series alloys [139,145,149]. Myhr et al. [142] took into account the reduction of nucleation sites associated to the heterogeneous precipitation of β' precipitates on β'' precipitates and on dispersoïds as well as the equilibrium vacancy concentration in 6xxx series alloys. Deschamps et al. [139] and Robson et al. [145] introduced the competition between homogeneous precipitation and heterogeneous precipitation on dislocations in 7xxx series alloys. Gallais et al. [54] also modeled the heterogeneous precipitation on dispersoïds in addition to the homogeneous precipitation and heterogeneous precipitation on dislocations. Kamp et al. [149] and Gallais et al. [54] introduced a reduction of the energy barrier for heterogeneous nucleation by an effective interfacial energy.
- Some authors [142,149] have explicitly modeled the evolution of the various meta-stable precipitates leading to the stable phase. Myhr et al. [142] distinguished between two precipitate size distributions for respectively the β'' and β' precipitates in 6xxx series alloys. Kamp et al. [149] also introduced two size distributions in a 7xxx series alloy for the η' and η precipitates.
- Ternary or quaternary phases can be produced when three alloying elements are involved like in the 6xxx series alloys containing also a high Cu content or in the 7xxx series alloys containing a high content of elements different to Mg and Zn. Robson et al. [148] explicitly accounted for the precipitation of a ternary phase $Al_3(Sc,Zr)$. Gallais et al. [54] accounted for the formation of the Q phase in the 6056 alloy.
- As described in Section 3.2.1, meta-stable precipitates are not always spherical. The shape of the precipitate affects the thermodynamics of the nucleation and growth. Liu et al. [144] presented an extension of the size class model to elongated precipitates using the Whelan formalism in the case of plate-like precipitates (see Section 3.1.1. of Ref. [13]).

Owing to the development of more powerful computers, Monte Carlo type simulations [154] and cluster dynamics [155] constitute a new possibility for modeling microstructure evolution. Still nowadays, the duration of calculations remains long on classical computers making these models less adapted for incorporation in a process optimization modeling approach. Now, these models constitute remarkable tools for the fundamental understanding of microstructure evolution and are a useful guide for calibration and development of "size class" models.

3.2.3. Microstructure evolution model

The precipitation model used in the model chain is based on Wagner and Kampmann's method [138]. It consists of three parts:

- a rate law to calculate the dissolution or coarsening of the precipitates;
- a nucleation law to predict the number of stable precipitate nuclei that form at each time step;
- a continuity equation to record the amount of solute being involved in the precipitates.

The precipitate composition is an input of the model. The precipitates in the 6005A and 6056 Al alloys are assumed to have the composition of the stable phases β-Mg_2Si and Q-$Al_5Cu_2Mg_8Si_6$, respectively [42,54]. This is an important assumption since the composition of the meta-stable (β'', β') precipitates slightly differs from the chosen reference [112,114,115]. Nevertheless, different precipitate distribution nucleating and growing from the same solute could be treated, see for instance Ref. [142,149]. In the case of ternary or quaternary precipitates (e.g. Q-$Al_5Cu_2Mg_8Si_6$), the element controlling the precipitation has to be identified first (see e.g. Ref. [149]). In the case of the 6xxx series Al alloys, Mg is considered to be the diffusion-limiting element. The reader is referred to Porter and Easterling [156] for explanations regarding the meaning of the thermodynamic concepts used hereafter.

For the sake of clarity the following notations will be applied throughout the description of the model:

- the subscript i corresponds to the element composing the precipitate (e.g. Mg, Si, Cu or Al) out of a total of n_{el} elements;
- the subscript j corresponds to the type of precipitation in the case of heterogeneous precipitation (e.g. homogeneous precipitation versus precipitation on dislocations versus precipitation on dispersoïds) out of a total of n_{type} types of precipitates;
- the subscript k corresponds to the size class out of a total of n_{class} classes.

3.2.3.1. Rate law. The rate v_j (m/s) at which dissolution or coarsening of a precipitate of radius r_j occurs is given by the Whelan formalism, assuming diffusion control, as

$$v_j = \frac{\partial r_j}{\partial t} = \frac{C_{ss} - C_{int}}{C_p - C_{int}} \frac{D}{r_j}, \tag{17}$$

where C_{ss} is the concentration in the precipitation controlling element within the matrix at a distance remote from the precipitate, C_{int} is the concentration of the same element at the matrix/precipitate interface given by the Gibbs–Thomson equation (see Eqs. (19) and (23)), C_p is the concentration in the precipitate of the same element and D (m^2/s) is the diffusion coefficient. The diffusion coefficient of any element i can be expressed as a function of temperature as an Arrhenius law:

$$D_i = D_0^i exp\left(-\frac{Q_d^i}{R_g T}\right), \tag{18}$$

where D_0^i (m^2/s) is a parameter, Q_d^i (J/mol) is the activation energy for diffusion, R_g (8.314 J/K mol) is the universal gas constant, T (K) is the absolute temperature.

In the case of binary precipitates, the Gibbs–Thomson equation is given by

$$C_{int} = C_e exp\left(\frac{2\gamma_{int} V_m}{r_j R_g T}\right), \tag{19}$$

where C_e is the equilibrium solute content at the precipitate/matrix interface, γ_{int} (J/m^2) is the precipitate/matrix interface energy, and V_m (m^3/mol) is the molar volume of the precipitate. The equilibrium solute content C_e can be expressed as a function of the temperature as

$$C_e = C_{e0} exp\left(-\frac{Q_e}{R_g T}\right), \tag{20}$$

where C_{e0} is a parameter and Q_e (J/mol) is the apparent solvus boundary enthalpy (energy per mole needed for the dissolution of the precipitates); C_{e0} and Q_e are given by the equilibrium phase diagram of the precipitating phase.

In the case of ternary or quaternary precipitates, the Gibbs–Thomson equation must be generalized by using the solubility product [126,146,149,151]. Let us consider the "precipitation reaction" producing, from n_{el} elements A^i in solid solution, the precipitate of composition $A^1_{x1}A^2_{x2}\ldots A^{n_{el}}_{xn_{el}}$, i.e.

$$x_1 A^1 + x_2 A^2 + \ldots + x_{n_{el}} A^{n_{el}} \rightarrow A^1_{x1} A^2_{x2} \ldots A^n_{xn_{el}}. \tag{21}$$

Assuming high dilution, the activity of an element is close to its concentration, the solubility product of the precipitate $A^1_{x1}A^2_{x2}\ldots A^n_{xn_{el}}$ of radius r_j is defined as (see e.g. [146,151])

$$K(r_j) = \prod_{i=1}^{n_{el}} (C^i_{int})^{C^i_p}, \tag{22}$$

where C^i_p is the atomic fraction of the element i in the precipitate ($C^i_p = x_i / \sum_{i=1}^{n_{el}} x_i$) and $C_{int}{}^i$ is the concentration of element i at the matrix/precipitate interface. The Gibbs–Thomson Eq. (19) can be generalized as follows, see e.g. [146,151],

$$K(r_j) = K_\infty exp\left(\frac{2\gamma_{int} V_m}{r_j R_g T}\right) \quad , \tag{23}$$

where K_∞ is the equilibrium solubility product across a planar interface that can be expressed as a function of temperature as

$$K_\infty = \prod_{i=1}^{n_{el}} (C^i_e)^{C^i_p} = K_0 exp\left(-\frac{Q_e}{R_g T}\right) \quad , \tag{24}$$

where C^i_e is the equilibrium concentration of element i at the precipitate/matrix interface and K_0 is a parameter. The complementary equation needed to determine C^i_{int} takes into account the interfacial fluxes equality [146,148,149,157,158], see Eq. (17),

$$D_{i1} \frac{C^{i1}_{ss} - C^{i1}_{int}}{C^{i1}_p - C^{i1}_{int}} = D_{i2} \frac{C^{i2}_{ss} - C^{i2}_{int}}{C^{i2}_p - C^{i2}_{int}}. \tag{25}$$

3.2.3.2. Nucleation law. If the incubation period is neglected, the steady state nucleation rate J_{nucl} (#/m^{3}s) can be expressed as

$$J_{nucl} = Z\beta^* N_{j,0} exp\left(\frac{-\Delta G^*}{R_g T}\right), \tag{26}$$

where Z is the Zeldovitch factor, on the order of 1/20 to 1/40 and which can be expressed as a function of the temperature (see e.g. Ref. [151]), $N_{j,0}$ (#/m^3) is the number of potential nucleation sites for the precipitation of type j, ΔG^* (J/mol) is the activation barrier for nucleation and β^* (s^{-1}) is the atomic impingement rate. The parameter β^* is given by

$$\beta^* = \frac{4\pi r_c^2}{a^4} D C_0, \tag{27}$$

where D is the diffusion coefficient given by Eq. (18), r_c is the critical radius that will be defined in Eq. (31) and a is the lattice parameter of the matrix (i.e. aluminum). The activation barrier for nucleation ΔG^* (J/mol) can be written as

$$\Delta G^{*} = \frac{16\pi}{3} \frac{\varphi_j \gamma^3{}_{int} N_A}{(\Delta G_v + \Delta G_e)^2}, \tag{28}$$

where φ_j is the wetting function expressing the difference in capillary conditions for the various types of precipitation [54,157], γ_{int} is the precipitate/matrix interface energy also used in Eqs. (19) and (23), ΔG_v (J/m^3) is the volume free energy change, ΔG_e (J/m^3) is the strain energy change associated to the precipitate nucleation, and N_A is the Avogadro number equal to 6.02214×10^{23} mol^{-1}. If n_{el} elements compose the solid solution, ΔG_v can be expressed as [54,159]

$$\Delta G_v = \frac{R_g T}{V_m} ln \left[\prod_{i=1}^{n_{el}} \left(\frac{C^i_{ss}}{C^i_e} \right)^{C^i_p} \right] = \frac{R_g T}{V_m} ln \left[\frac{\prod_{i=1}^{n_{el}} (C^i_{ss})^{C^i_p}}{K_\infty} \right], \tag{29}$$

where C^i_e is the equilibrium concentration of the element *i*. In the case of binary precipitates, if the strain energy change associated to the precipitate nucleation is neglected, the expression of the nucleation rate (Eq. (26)) is often simplified [13,42,140–142,147,152] as

$$J_{nucl} = J_0 exp \left(- \frac{(A_0)^3}{(R_g T)^3 [ln(C_{ss}/C_e)]^2} \right) exp \left(- \frac{Q_d}{R_g T} \right), \tag{30}$$

where J_0 (#/m^{3}s) is a parameter and A_0 (J/mol) is another parameter related to the energy barrier for nucleation.

During a time step, newly nucleated precipitates appear with a radius equal to the critical radius r_c. If the change in the strain energy associated to the nucleation is neglected, the critical radius that corresponds to the radius of a precipitate that will neither grow nor dissolve is given by

$$r_c = - \frac{2\gamma_{int}}{\Delta G_v + \Delta G_e}. \tag{31}$$

3.2.3.3. Continuity equation and numerical discretization. If N_j (#/m^3) is the density of precipitates of type *j*, a precipitate balance in a given size class gives

$$\frac{\partial N_j}{\partial t} = - \frac{\partial (N_j v_j)}{\partial r_j} + J^j_{nucl}, \tag{32}$$

where J^j_{nucl} (#/m^{3}s) is the steady state nucleation rate obtained from Eqs. (26) or (30). Various types of precipitations can simultaneously occur in the system, i.e. n_{type} types of precipitation. Eq. (32) must be solved for each types of precipitation. The equivalent radius distribution of each precipitation type *j* is divided into n_{class} classes of size Δr having a density of precipitates N_{jk} (#/m^3) and a mean equivalent radius r_{jk}. These size classes are treated as control volumes to which the continuity equation is applied. An initial size distribution needs to be defined. The precipitates volume fraction f^j_v of each type of precipitation is calculated by

$$f^j_v = \sum_{k=1}^{n_{class}} \frac{4}{3} \pi (r_{jk})^3 N_{jk} \Delta r, \tag{33}$$

and the total precipitate volume fraction f_v is given by

$$f_v = \sum_{j=1}^{n_{type}} f^j_v. \tag{34}$$

The mean precipitate radius *r* is calculated using the following expression

$$r = \frac{1}{f_v} \sum_{j=1}^{n_{type}} \left(f^j_v \frac{\sum_{k=1}^{n_{class}} r_{jk} N_{jk}}{\sum_{k=1}^{n_{class}} N_{jk}} \right). \tag{35}$$

Table 3
Parameters of the microstructure evolution model for the 6005A alloy.

Parameter	Symbol	Value [42]
Pre-exponential term to C_e	C_{e0}	290 wt.%
Activation energy for solvus boundary	Q_e	41,000 J/mol
Pre-exponential term to D of Mg	D_0	10^{-4} m^2/s
Activation energy for D of Mg	Q_d	130,000 J/mol
Interfacial energy	γ_{int}	0.26 J/m^2
Molar volume of precipitates	V_m	3.95×10^{-5} m^3/mol
Energy barrier for nucleation	A_0	18.6 kJ/mol
Pre-exponential term to J_{nucl}	J_0	3×10^{37} #/m^3 s

The mean solute concentration in the matrix of an element i is calculated using

$$C_{ss}^i = \frac{C_0^i - C_p^i\left(\sum_{j=1}^{n_{type}} f_v^j\right)}{1 - \left(\sum_{j=1}^{n_{type}} f_v^j\right)}, \tag{36}$$

where C_0^i is the solute content of element i in the alloy. When multicomponent systems and multiple precipitate types are addressed, the solid solution composition evolves, for each element, following the evolution of the precipitate state. As a consequence, the evolutions of all the precipitates are coupled via the solid solution.

3.2.3.4. Extension to elongated precipitates. The meta-stable precipitates found in the 6xxx series Al alloys generally involve rod or needle-like shape. The microstructure evolution model described above initially written for spherical precipitates can be generalized to the case of a constant elongation ratio of a precipitate [54,157]. The elongation ratio, α_e, is defined as the length of a cylinder divided by its radius. Eq. (23) writes

$$K = K_\infty exp\left(\frac{4}{3}\frac{1+\alpha_e}{\alpha_e}\frac{\gamma_{int}V_m}{r_j R_g T}\right), \tag{37}$$

while Eq. (28) becomes

$$\Delta G^* = \frac{224\pi\alpha_e}{81}\frac{\varphi_j\gamma_{int}^3 N_A}{\left(\Delta G_v + \Delta G_e\right)^2}, \tag{38}$$

hence Eq. (31) becomes

$$r_c = -\frac{4}{3}\frac{1+\alpha_e}{\alpha_e}\frac{2\gamma_{int}}{\Delta G_v + \Delta G_e}. \tag{39}$$

3.2.3.5. Application to 6xxx series Al alloys. The model has been adapted to the 6005A Al alloy [42] by assuming pseudo binary precipitation of the Mg_2Si phase[1] using the diffusion coefficient of Mg, and by applying Eq. (19) to describe the solute concentration at the precipitate/matrix interface and Eq. (30) for the nucleation rate. Even though the meta-stable precipitates are elongated, the present version of the model treats only the distribution of the equivalent radius r_{eq} based on a sphere having the same volume as the real precipitates. Table 3 presents all the parameters used for the 6005A model. Fig. 9a presents the precipitate size distribution used to model the 6005A-T6 base material. Contrarily to the 6005 alloy, the elongated shape of the precipitates is accounted for in the 6056 alloy [54]. The precipitation of the Q phase is explicitly modeled, and Eqs. (25) and (37) have been used for calculating the solute concentration at the precipitate/matrix interface. Heterogeneous precipitation on dislocations and dispersoïds are modeled in addition to the homogeneous precipitation. Table 4 gathers all the

[1] This choice is made despite the fact that the chemical composition of the β'' and β' precipitates is different than the composition of the stable β-Mg_2Si phase, see Section 3.2.1.

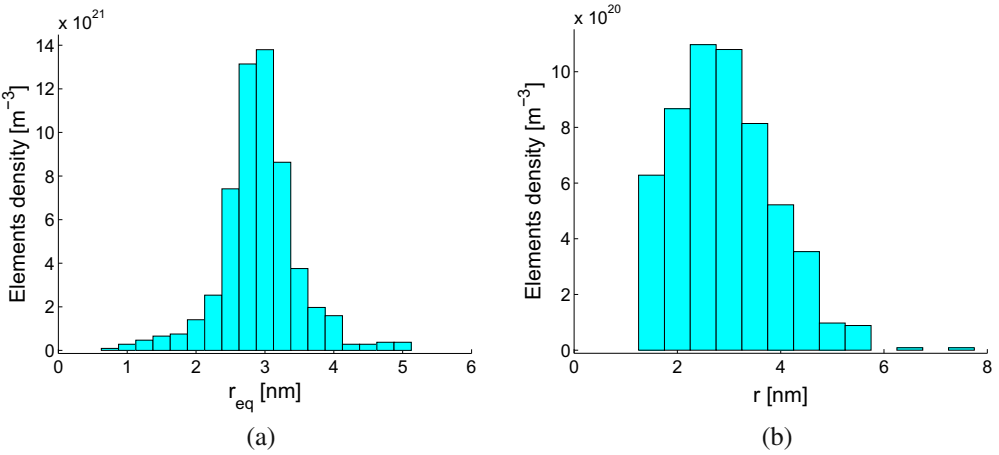

Fig. 9. Distribution of precipitates radius in the base materials for (a) the 6005A-T6 alloy (from Ref. [42]) and (b) the 6056-T78 alloy.

Table 4
Parameters of the microstructure evolution model for the 6056 alloy.

Parameter	Symbol	Value [54]
Pre-exponential term to K_∞	K_0	1458
Activation energy for solvus boundary	Q_e	71,645 J/mol
Pre-exponential term for diffusion of Mg	D_0^{Mg}	1.24×10^{-4} m^2/s
Activation energy for diffusion of Mg	Q_d^{Mg}	130,632 J/mol
Pre-exponential term for diffusion of Si	D_0^{Si}	2.08×10^{-4} m^2/s
Activation energy for diffusion of Si	Q_d^{Si}	136,228 J/mol
Pre-exponential term for diffusion of Cu	D_0^{Cu}	0.65×10^{-4} m^2/s
Activation energy for diffusion of Cu	Q_d^{Cu}	135,359 J/mol
Pre-exponential term for diffusion of Al	D_0^{Al}	0.13×10^{-4} m^2/s
Activation energy for diffusion of Al	Q_d^{Al}	129,300 J/mol
Interfacial energy	γ_{int}	0.6 J/m^2
Molar volume of precipitates	V_m	10^{-5} m^3/mol
Number of potential sites homogeneous precipitates	N_0^{homo}	$N_A/V_m = 6.10^{28}$ m^{-3}
Number of potential sites preci. on dislocations (welds)	N_0^{disloc}	$\rho/b = 3.52 \times 10^{23}$ m^{-3}
Number of potential sites preci. on dispersoïds	$N_0^{disperso}$	2×10^{19} m^{-3}
Zeldovitch factor	Z	0.05
Wetting function homogeneous precipitates	φ_{homo}	2.7×10^{-3}
Wetting function precipitates on dislocations	φ_{disloc}	2.2×10^{-3}
Wetting function precipitates on dispersoïds	$\varphi_{disperso}$	5×10^{-5}
Strain energy due to nucleation	ΔG_e	1.2×10^9 J/m^3
Precipitate elongation ratio	α_e	25

parameters of the model. Fig. 9b shows the precipitate size distribution used to model the 6056-T78 base material. These parameters have been calibrated on isothermal heat treatments as described in Simar et al. [42], for the 6005A alloy, and Gallais et al. [54], for the 6056 alloy, using hardness or tensile tests and the model described in the next section. For the 6056 alloy, an estimate is needed for the number of potential sites (i.e. N_0) and the wetting function (i.e. φ_j) corresponding to heterogeneous precipitation on dislocations or on dispersoïds. The dislocation density ρ has been estimated by Gallais et al. [54] as equal to 10^{14} m^{-2}, a high value resulting from the large deformation induced by the FSW process, particularly in the TMAZ. The number of potential sites for the heterogeneous precipitation on dislocations N_0^{disloc} is

Table 5
Parameters for the yield strength and strain hardening models (SS = solid solution, NA = natural aging), see Simar et al. [42] and Gallais et al. [54].

Parameter	Symbol	Value 6005A	Value 6056
Taylor factor	M	2	2
Shear modulus	G	2.7 GPa	2.7 GPa
Magnitude of Burger's vector	b	2.84×10^{-10} m	2.84×10^{-10} m
Yield strength of pure Al	σ_f	10 MPa	10 MPa
Constant for the effect of Mg in SS content on σ_{ss}	k_{Mg}	29 MPa wt.%$^{2/3}$	29 MPa wt.%$^{2/3}$
Constant for the effect of Si in SS content on σ_{ss}	k_{Si}	66.3 MPa wt.%$^{2/3}$	66.3 MPa wt.%$^{2/3}$
Constant for the effect of Cu in SS content on σ_{ss}	k_{Cu}	46.4 MPa wt.%$^{2/3}$	46.4 MPa wt.%$^{2/3}$
Transition radius	r_{trans}	3.04 nm	2.6 nm
Line tension constant	β_{Γ}	0.45	0.28
Limit C_{ss} for NA	C_{lim}	0.45 wt.%	0.2 wt.%
Constant for NA model	K_{NA}	58.1 MPa	168 MPa
Constant used to calculate *HV*	A_{HV}	0.26 HV MPa^{-1}	0.33 HV MPa^{-1}
Constant used to calculate *HV*	B_{HV}	35.6 HV	20 HV
Maximum yield strength (T6 material)	σ_0^{max}	260 MPa	338 MPa
Hardening rate θ with no dynamic preci pitation and no Orowan loops (θ of T6 material)	θ_0	600 MPa	600 MPa
Recovery term β when σ_0 is maximum (β of T6 material)	β_{min}	7.5	7.5
Constant linking σ_0 to β_0	k_{β}	9.3	6.2
Constant for the dynamic precipitation effect on θ	$k_{\theta dp}$	1270 MPa	1395 MPa
Radius of loss of coherency	r_{cl}	25 nm	25 nm
Mean distance between two moving dislocations of opposite sign	L_0	100 nm	100 nm
Constant linking the dislocation density to the shear stress	α	0.21	0.21
Annihilation distance when at least one precipitate lies between two dislocations of opposite sign	y_{preci}	22 nm	10 nm

the ratio between this dislocation density and the magnitude of the Burger's vector (see Tables 4 and 5). The number of potential sites for heterogeneous precipitation on dispersoïds $N_0^{disperso}$ is evaluated from microstructure observations but could have been extracted from upstream process models, see Dons [11] for a model predicting the dispersoïds density following the homogenization treatment. Finally, the wetting functions are calibrated on a wide variety of heat treatment conditions where the type of precipitation was systematically characterized (see Fig. 8 in Ref. [54]).

In Section 4.2.3, both microstructure evolution models, for the 6005A and the 6056 Al alloys, will be validated on friction stir welds made of the 6005A-T6 and 6056-T78 base materials. For the 6005A-T6 welds, the model validation will be based on TEM image analysis providing estimated mean radius at various distances away from the weldline. For the 6056-T78 welds, the model validation will be based on DSC measurements delivering estimates of the relative volume fraction of precipitates at various distances from the weldline.

3.3. Strength and strain hardening of precipitation hardened Al alloys

The precipitation models, described in Section 3.2.3, predict the solid solution concentration and the size distribution of every type of precipitates in the alloy under investigation for a given thermal history resulting from the welding or any pre or post welding heat treatment. This information is needed to quantify the strength of the material. The strength will be modeled both in terms of initial yield strength (see Section 3.3.1) and in terms of the strain hardening capacity (see Section 3.3.2). When one is concerned with predicting the overall mechanical properties of welds, a first step is to know how the mechanical properties are distributed throughout the different regions of the weld.

3.3.1. Yield strength model

In 6xxx series Al alloys, the yield strength and hardness evolutions due to an aging treatment starting from the T4 state has been widely studied, see e.g. [42,54,99,103,105,130,131,160–162]. The T4 material, hardened by solid solution and GP zones, becomes harder due to the formation of β''

precipitates, reaching the peak strength at the so-called T6 state. Subsequent over-aging will cause a drop of the yield strength due to the excessive growth of the precipitates and their transformation into β' and β precipitates.

3.3.1.1. Literature survey on yield strength models. The version of the model used in the present work is widely accepted in the literature [19,42,54,130,131,141,142,147,152,159,162]. The main contribution to the yield strength is the contribution of the precipitates. When the radius is lower than a critical value r_{trans}, the precipitates are sheared by the dislocations and the yield strength increases with the square root of the precipitates radius. When the radius is larger than r_{trans}, the precipitates are by-passed by the dislocations and the yield strength varies with the inverse of the precipitate radius, see Fig. 10 for a schematic of the yield strength evolution with precipitate radius.

Some variants of the model presented below can be found in the literature. Zhu and Starke [163] derived an extension of the Orowan expression for the strengthening coming from non-shearable precipitates. This expression is based on computer simulations of the equilibrium configurations of a dislocation interacting with randomly distributed non-shearable precipitates. Starink and Wang [132] and Khan et al. [150] used this expression to predict the yield strength of Al alloys. Wang et al. [164] used a slightly different expression to describe the strength in the presence of the S phase in a 2024 Al alloy. Esmaeili et al. [129,133] calculated the relative volume fraction of precipitates using an analytical precipitation model in order to evaluate the yield strength. For shearable precipitates, the yield strength is proportional to the square root of the radius multiplied by the relative volume fraction of precipitates. For non-shearable precipitates, the yield strength is proportional to the square root of the relative volume fraction of precipitates. Yazdanmehr et al. [135] used the same expressions to evaluate the yield strength evolution in over-aged AA6061.

3.3.1.2. Yield strength model. The main contributions to the strengthening mechanism of an age hardenable Al alloy are the following:

- σ_d (MPa) is the grain size contribution to the flow stress due to the Hall–Petch effect [165,166]. This contribution is generally negligible in age hardening Al alloys compared to the precipitation hardening. The contribution of the grain size to strengthening is considered by Starink et al. [167] to be, in most cases, less than 10 MPa in the weld nugget of FSW joints where dynamic recrystallization favors the formation of very fine grains compared to the base material, see for instance in Refs. [132,168] how to account for the grain size effect on the strength of friction stir welds.
- σ_{ss} (MPa) is the solid solution contribution to the flow stress, expressed as [169]

$$\sigma_{ss} = \sum_{i=1}^{n_{el}} k_i {C_{ss}^i}^{2/3}, \tag{40}$$

where k_i are constants associated to the strength increase resulting from the presence of element i with concentration C_{ss}^i (wt.%).[2] In the case of the 6056 alloy, all the constituents of the solid solution must be taken into account when calculating the contribution to the strength. In the case of the 6005A alloy, Cu will be assumed to remain in solid solution since the θ-Al_2Cu precipitates have very low dissolution temperatures. Furthermore, the Si solid solution concentration C_{ss}^{Si} is assumed to vary proportionally with the Mg solid solution concentration C_{ss}^{Mg} following the composition of the Mg_2Si precipitates. This is equivalent to assuming that the excess Si has precipitated in non-hardening coarse Si precipitates that do not dissolve during the process. Hence, for low Cu and excess Si aluminum alloys, e.g. the 6005A alloy, Eq. (40) can be simplified into [42,54]

$$\sigma_{ss} = k_{Mg_2Si}(C_{ss})^{2/3} + k_{Cu}(C_{Cu})^{2/3}, \tag{41}$$

where k_{Mg_2Si} is a constant equal to

[2] The units are expressed here in (wt.%) based on the units of k_i, but it is not mandatory. In the case of the microstructure evolution model, it is easier to express C_{ss}^i in at.%.

$$k_{Mg_2Si} = k_{Mg} + k_{Si}\ \left(\frac{100 - C_p^{Mg}}{C_p^{Mg}}\right). \tag{42}$$

- σ^j_{preci} (MPa) is the contribution to the flow stress due to the presence of precipitates of type j. Only the main equations will be recalled here. The reader is referred to Gerold [170], Ardell [171], Deschamps et al. [139] and Nembach [172] for a thorough description of the underlying assumptions. If we assume that the dislocation line has to overcome all the obstacles which are encountered when gliding in the slip plane to induce a macroscopic strain, σ^j_{preci} can be expressed as [139]

$$\sigma^j_{preci} = \frac{M\overline{F}_j}{bl_j}, \tag{43}$$

where M is the Taylor factor, $\overline{F}_j$ (N) is the mean obstacle strength, b (m) is the magnitude of the Burger vector and l_j (m) is the particle spacing in the glide plane of the dislocations for the type j precipitation. The spacing l_j can be expressed in terms of the mean precipitates radius r_j using Friedel's statistical model [170,171,173]:

$$l_j = \sqrt{\frac{2\pi}{3}}\frac{r_j}{\sqrt{f^j_v}}, \tag{44}$$

which gives

$$\sigma^j_{preci} = \frac{M}{b\sqrt{2\Gamma}}\sqrt{\frac{3f^j_v}{2\pi}}\frac{\overline{F}_j^{3/2}}{r_j}, \tag{45}$$

where $\Gamma = \beta_\Gamma G\, b^2$ (N) is the dislocation line tension with β_Γ considered as constant $\approx$0.5 [171] and G (Pa) is the shear modulus. In the case of a precipitation distribution, $\overline{F}_j$ can be calculated as

$$\overline{F}_j = \frac{\sum_k^{n_{class}} N_{jk}F_{jk}}{\sum_j^{n_{class}} N_{jk}}, \tag{46}$$

where F_{jk} is the obstacle strength for the size class k and type j precipitation. The obstacle strength F_{jk} depends on the mechanism of interaction between the dislocation and the precipitate.

  - If the precipitate radius r_{jk} is lower than an equivalent transition radius r_{trans}, the precipitates are sheared by the dislocations and $F_{jk} = 2\beta_\Gamma Gb^2\left(\frac{r_{jk}}{r_{trans}}\right)$ [139]. This expression, suggested by Gerold [170], does not take explicitly into account the details of the complex mechanisms involved in the dislocation/precipitate interaction (chemical, stacking-fault, modulus, coherency or order strengthening [171]).
  - If the precipitate radius r_{jk} is larger than an equivalent transition radius r_{trans}, the precipitates are by-passed by the dislocations following the Orowan mechanism and $F_{jk} = 2\beta_\Gamma Gb^2$ [139].

- $\sigma_{pl} = M\alpha Gb\sqrt{\rho}$ is the dislocation density contribution to the flow stress where ρ is the forest dislocation density and α is a constant ranging between 0.2 and 1.5. When evaluating the initial yield strength, this term can be considered as negligible which corresponds to assuming that $\sigma^j_{preci} \gg \sigma_{pl}(\rho = \rho_{init})$. Starink et al. [167] confirmed this assumption based on TEM image analysis. Gallais et al. [54] estimated the dislocation density in the 6056-T78 base material to be equal to 10^{13} m^{-2} and equal to 10^{14} m^{-2} in the thermomechanically affected zone of a weld. These estimates lead to σ_{pl} equal to respectively 1 MPa in the base material and 3 MPa in the thermomechanically affected zone (see Table 5 for the other parameters).

The important contributions to the yield strength are added up using [174,171]

$$\sigma_0 = \sigma_f + \sigma_{ss} + \sigma_{preci}, \tag{47}$$

where σ_f is the friction stress in pure Al (about 10 MPa). The choice of a linear additivity rule is based on the comparison with numerical simulations of obstacle strength performed by Brown and Ham

[174]. These authors concluded that when a small number of strong obstacles (i.e. precipitates) are mixed with many weak obstacles (i.e. the solute atoms), the linear superposition gives correct predictions of the total strength. Now, in all other instances, the pythagorean additivity rule gives more accurate predictions. Hence, the total contribution to hardening of the precipitates of the n_{type} distributions (i.e. for the 6056 alloy: homogeneous precipitation and heterogeneous precipitation on dislocations and dispersoïds) will be estimated as

$$\sigma_{preci} = \sqrt{\sum_{j}^{n_{type}} \left(\sigma_{preci}^{j}\right)^2}. \tag{48}$$

Myhr et al. [142] also combined Eqs. (47) and (48) to describe the strengthening of two types of precipitates (i.e. β'' and β') inside a solid solution.

The hardness HV can be inferred simply from the yield strength σ_0 by using a linear regression [13,19,42,54,141]

$$HV = A_{HV}\sigma_0 + B_{HV}, \tag{49}$$

where A_{HV} and B_{HV} are the parameters of the linear regression. A_{HV} is generally close to 1/3.

3.3.1.3. Natural aging model. In addition to the hardening due to the precipitation resulting from the thermal history, post-welding natural aging can induce an increase of the yield strength due to the local precipitation of GP zones. Only the final state where GP zones formation is completed is considered here since this usually occurs within a couple of days or weeks after welding. The formalism by Esmaeili et al. [129] states that the radius of the GP zones is independent of the initial solid solution content and is thus constant. Moreover, the final volume fraction of the GP zones is considered to be proportional to the solid solution concentration minus a constant accounting for a miscibility gap, C_{lim} (wt.%). The contribution of the GP zones to the yield strength is based on the classical contribution of shearable precipitates and can be expressed as[3]

$$\sigma_{0/NA} = \sigma_0 + K_{NA}\sqrt{\frac{C_{ss}^{Mg} - C_{lim}}{C_0^{Mg} - C_{lim}}}, \tag{50}$$

where K_{NA} (MPa) is given by

$$K_{NA} = \sigma_{SHT}^{init} - \sigma_{SHT}^{NA} \tag{51}$$

where σ_{SHT}^{init} is the yield strength just after a solution heat treatment and σ_{SHT}^{NA} is the yield strength after the saturation of the natural aging strengthening.

3.3.1.4. Model parameters. Table 5 summarizes the parameters of the yield strength model as applied to the 6005A [42] and to the 6056 Al alloys [54]. In Section 4.2.4, this yield strength model will be validated towards micro-tensile tests, performed on specimens extracted from the various zones of the weld and towards hardness measurements performed across 6005A-T6 and 6056-T78 welds.

3.3.2. Strain hardening model

Proper modeling of the strain hardening capacity is essential in order to address the resistance of the weld (i.e. in uniaxial tensile, the pseudo ultimate tensile strength and the pseudo uniform elongation).

3.3.2.1. Strain hardening behavior of Al alloys. For pure metals, the Kocks–Mecking–Estrin (KME) model [175–177] links the variation of the dislocation density ρ to the local plastic shear strain γ_p

$$\frac{d\rho}{d\gamma_p} = k_1\sqrt{\rho} - k_2\rho, \tag{52}$$

[3] The contribution to strengthening of the solid solution giving rise to the precipitation of GP zones must be subtracted from the initial yield strength as expressed by Eq. (47) (see e.g. Ref. [42] for the 6005A alloy).

where k_1 and k_2 are proportionality constants. Since $\sigma_{pl} = M\alpha Gb\sqrt{\rho}$ (Taylor relation) and using the definition of the Taylor factor $M = \sigma_y/\tau_y = \gamma_p/\varepsilon_p$, the evolution of the flow stress σ_y with the plastic strain can be expressed as

$$\frac{d\sigma_y}{d\varepsilon_p} = \theta_0 - \beta_0(\sigma_y - \sigma_0), \tag{53}$$

where $\theta_0 = \alpha GbM^2k_1/2$ and $\beta_0 = k_2M/2$ are related to the dislocation storage and dynamic recovery rates for pure materials. The term θ_0 is typically equal to $G/20$. Eq. (53) had been initially identified empirically by Voce [178].

Even if Eq. (53) is theoretically only valid for pure materials, it is classical in the literature related to strain hardening of Al alloys [179–183] to assume that the plastic slope varies linearly with the flow stress in more general situations such as the presence of precipitates. In that case, Eq. (53) is generalized as

$$\frac{d\sigma_y}{d\varepsilon_p} = \theta - \beta(\sigma_y - \sigma_0), \tag{54}$$

where θ and β are also assumed to be related to the dislocation storage and the dynamic recovery rate.

Deschamps et al. [179] performed channel-die compression of Al alloys containing up to 0.4 wt.% Cu and concluded that the increasing solute content increases the work hardening capacity. Later, Deschamps et al. [180] and Esmaeili et al. [181] determined, using tensile tests on a Al–Mg–Si–Cu alloy, that the initial work hardening rate (i.e. the parameter θ) increases significantly when the material naturally ages from the as-quenched solution heat treated condition. Oppositely, β is relatively unaffected by natural aging. When aging up to the peak strength, θ decreases. A slight decrease of β is only observed for the Al–Mg–Si–Cu alloy at the peak strength. In a Al–Zn–Mg alloy, a slight over-aging causes a drastic increase of both θ and β. Massively over-aged conditions (e.g. 6 months at 180 °C) lead to θ values similar to the peak aged condition in the Al–Mg–Si–Cu alloys. Cheng et al. [182] have fitted Eq. (53) to stress–strain curves obtained on Al alloys 6111 and 7030. For the 6111 alloy, θ decreases significantly from the under-aged to the peak aged condition while β only slightly drops. Both θ and β increase from the peak-aged to the over-aged condition. After a long aging time, β reaches a maximum plateau value. Similar trends have been observed for the evolution of θ with heat treatment time for the 7030 alloy, but β was slightly increasing from the under-aged to the peak-aged condition and no maximum of β was reached for the over-aged condition. Simar et al. [42] have observed for a 6005A Al alloy an evolution of the work hardening capacity similar to the 6111 alloy studied by Cheng et al. [182]. In addition, Simar et al. [42] have shown that both θ and β drop after a very long over-aging at relatively high temperatures (300 °C and 350 °C). Dumont et al. [184], Fribourg et al. [183] and Westermann et al. [185] analyzed the work hardening capacity on Al–Mg–Zn alloys and have also confirmed the trends described in the 7xxx series Al alloys.

To summarize, the presence of precipitates affect the strain hardening parameters θ and β in the following way (see schematics in Fig. 10):

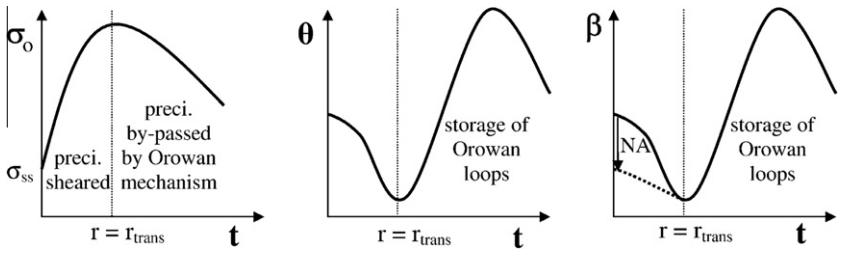

Fig. 10. Schematic of the evolution of the yield strength σ_0 and strain hardening parameters θ and β with heat treatment duration t starting from a supersaturated solid solution (NA = natural aging).

- The supersaturated solid solution samples have a high value of θ while β is only slightly larger than in a peak aged condition. Note that in the 7xxx series alloys, the drop of β from under-aged conditions to peak aged conditions is not observed. Deschamps et al. [186] attributed the large value of the parameter θ of a supersaturated solid solution to the dynamic precipitation in an Al–Zn–Mg alloy.
- The parameters θ and β reach a minimum when the material is close to its maximum yield strength state.
- When aging proceeds (over-aging), precipitates are by-passed, leaving Orowan loops around the precipitate. The parameters θ and β significantly increase up to reaching a maximum.
- When the samples are massively over-aged, the parameters θ and β drop in the 6xxx series alloys. This has however not been evidenced in the 7xxx series alloys.

3.3.2.2. Modeling strain hardening in age-hardenable Al alloys. Very few models have been proposed to predict the strain hardening behavior of solute/precipitation hardened materials as a function of the microstructure even though this is essential regarding the strength/ductility of the base alloys and of the welded joints (see later). The main contributions in the last 10 years to modeling the effect of solute and precipitation on strain hardening in Al alloys will be summarized hereafter; readers are referred to Kocks and Mecking [177] regarding physics based modeling of strain hardening in general.

Marthinsen, Nes and co-workers [187–192] developed a two state variable model for the strain hardening of metals. This model relies on the description of the evolution of the dislocation density inside the cell structure and a description of the cell size. This model has also been used to describe the effect of the grain size on the strain hardening capacity of Al alloys containing solute atoms and non-deformable precipitates [190–192]. The effect of precipitation on dislocation storage is accounted for by changing the effective slip length based on the precipitate radius and volume fraction (with $l = r/2f_v$, where l is the mean distance between obstacles in the glide plane of the dislocation), the grain size, and the mean distance between dislocations (proportional to $\rho^{-1/2}$). The dynamic recovery is only affected by the solute content, through an effect on the dislocation velocity, and not by the presence of precipitates.

Roters et al. [193] and Goerdeler et al. [194,195] described the evolution of three state variables, i.e. the mobile dislocation density, cell interior and cell wall dislocation density, as a function of the plastic strain, strain rate and temperature in an application to Al alloys. The model accounts for the storage of mobile dislocations into the cell walls, to dislocation locks or dipoles. The effect of precipitation on strain hardening is accounted for by changing the effective slip length similarly to Marthinsen and Nes [190] (except for the use of $l = r/\sqrt{f_v}$). Goerdeler et al. [195] accounted for the solute atoms through a modified effective activation energy.

Estrin [196] reviewed the theory needed for developing constitutive laws for precipitation and solute hardened alloys in order to generalize the KME model. Estrin [196] took the storage of Orowan loops into account by introducing a new term in the evolution of the dislocation density with deformation, given by Eq. (52). This term is inversely proportional to the obstacle spacing in the glide plane of the dislocations l (m):

$$\frac{d\rho}{d\gamma_p} = k_1\sqrt{\rho} + \frac{1}{bl} - k_2\rho. \tag{55}$$

Barlat et al. [197] introduced also the term $1/bl$ to model strain hardening in Al alloys and accounted for the dislocation cell structure and the microstructure associated to a mean free path for dislocation glide. Simar et al. [42] used this model with l as given by Eq. (44) and extended it, as explained later, to describe the strain hardening behavior of a 6005A Al alloy. Fazeli et al. [159] made use of Eq. (55) to capture the strain hardening of Al–Mg–Sc alloys. Poole, Lloyd and co-workers [182,198] suggested to tune the exponent of the additivity law associated to the strength of the dislocations density (i.e. σ_{pl}) and the precipitates (i.e. σ_{preci}) to the type of precipitate/dislocation interaction (shearable vs non-shearable).

Some authors have incorporated kinematic hardening contributions (internal stress) affecting the mechanical response of Al alloys [199,200]. Reynolds and Baxter [199] relied on composite theory to

describe the kinematic hardening of the 8009 dispersion strengthened alloy. Proudhon et al. [200] extended the model of Brown and Stobbs [174] to predict the internal stresses in a 6111 Al alloy. Fribourg et al. [183] suggested a way of linking the isotropic strain hardening model described later in the present paper and the kinematic hardening model by Proudhon et al. [200]. Teixeira et al. [201] combined the model by Poole, Lloyd and co-workers [182,198], Simar et al. [42] and Proudhon et al. [200] to represent the strain hardening behavior of Al–Cu–Sn alloys. Kinematic hardening will be neglected hereafter in order to limit the number of model parameters.

3.3.2.3. Strain hardening model - Dislocation storage term θ. The shear flow stress τ_y (Pa) is related to the forest dislocation density ρ (#/m^2) by

$$\tau_y = \tau_0 + \alpha G b \sqrt{\rho}, \tag{56}$$

where τ_0 (Pa) is the shear flow stress at the beginning of yielding. The evolution of the dislocation density with the local plastic shear strain γ_p is given by Eq. (52) if no Orowan loop is stored around precipitates (i.e. $r \leqslant r_{trans}$) and by Eq. (55) if Orowan loops are stored around precipitates (i.e. $r > r_{trans}$). The expression of the work hardening rate is given by

$$\frac{d\tau_y}{d\gamma_p} = \frac{d\tau_y}{d\rho}\frac{d\rho}{d\gamma_p} \tag{57}$$

$$= \frac{\alpha G b}{2\sqrt{\rho}}\left(k_1\sqrt{\rho} + \frac{k^*}{bl} - k_2\rho\right) \tag{58}$$

$$= \frac{\alpha G b k_1}{2} + \frac{\alpha^2 G^2 b}{2l(\tau_y - \tau_0)} - \frac{k_2}{2}(\tau_y - \tau_0), \tag{59}$$

with $k^* = 1$ if $r > r_{trans}$ and $k^* = 0$ if $r < r_{trans}$. By introducing the Taylor factor M and the expressions for θ_0 and β_0, one gets

$$\frac{d\sigma_y}{d\gamma_p} = \theta_0 + \frac{k^*\alpha^2 G^2 b M^3}{2l(\sigma_y - \sigma_0)} - \beta_0(\sigma_y - \sigma_0). \tag{60}$$

Hence, the dislocation storage parameter θ expresses as

$$\theta = \theta_0 + \frac{k^*\alpha^2 G^2 b M^3}{2l(\sigma_y - \sigma_0)}. \tag{61}$$

For the sake of simplicity, one can assume that the variation of $(\sigma_y - \sigma_0)$ between *0* and $(\sigma_{sat} - \sigma_0)$ [4] is small. A mean value of $(\sigma_y - \sigma_0)$ can be introduced in the second term of Eq. (61) as given by $(\sigma_{sat} - \sigma_0)/2 = \theta/(2\beta)$. Using this formalism, the assumption that the dislocation storage parameter θ is independent of the flow stress is an approximation which is well validated by experimental tensile tests results on Al alloys, as described in the literature survey. Using the expression of l, see Eq. (44), an implicit expression for the dislocation storage parameter θ is obtained

$$\frac{\theta}{G} = \frac{\theta_0}{G} + \alpha^2 G M^3 \frac{\beta}{\theta}\sqrt{\frac{3f_v}{2\pi}}\left(\frac{b}{r}\right) \tag{62}$$

which can also be written as

$$\frac{\theta}{G} = \frac{\theta_0}{2G} + \sqrt{\left(\frac{\theta_0}{2G}\right)^2 + \alpha^2 M^3 \beta\left(\frac{b}{r}\right)\sqrt{\frac{3f_v}{2\pi}}}. \tag{63}$$

A sharp transition between precipitates shearing and precipitates bypassing is an idealization when the material deforms plastically beyond the yield point. The flow stress increases due to work

[4] The saturation stress σ_{sat} is the stress at which $d\sigma/d\varepsilon_p = 0$.

hardening. In practice, the precipitates with a radius slightly larger than r_{trans} will first be bypassed by dislocations. When plastic straining proceeds, the Orowan loop undergoing an increasing stress due to the increasing pile up intensity as other dislocation loops accumulate and the increasing overall stress will end-up shearing the precipitate if it is coherent with the matrix [202]. Finally, the loop annihilates itself. An efficiency factor φ for the storage of Orowan loops is introduced in order to take into account the stability of the Orowan loops [42]. The factor φ is defined as the proportion of the Orowan loops that could potentially be formed and will not finish annihilating themselves when the flow stress increases. These are the efficiently stored loops. Two extreme cases must be distinguished.

- When $r = r_{trans}$, no Orowan loops will be stored since the Orowan loops created will directly auto-annihilate after precipitate shearing, with no excess plastic deformation needed. Hence, the condition $r \leqslant r_{trans}$ imposes $\varphi = 0$.
- When $r = r_{cl}$, where r_{cl} is the radius corresponding to the loss of coherency, all the Orowan loops will be stored. Hence, $r \geqslant r_{cl}$ leads to $\varphi = 1$.

Moreover, the efficiency of dislocation storage φ certainly increases with increasing radius. For a larger radius, a higher stress level must be attained owing to strain hardening before the Orowan loops can auto-annihilate through precipitate shearing [202]. Hence, the storage of Orowan loops becomes more efficient. For the sake of simplicity, a linear variation is assumed for φ as a function of r [42]. In between the two extreme cases, i.e. when $r_{trans} < r < r_{cl}$, the efficiency factor writes

$$\varphi = \frac{r - r_{trans}}{r_{cl} - r_{trans}}. \tag{64}$$

Precipitation from a supersaturated solid solution (i.e. $C_{ss} > C_e$) requires atomic transport. Usually this transport occurs by diffusion of chemical species. But, plastic deformation induces also atomic transport, and creates point defects enhancing the transport phenomena. This suggests that deforming a supersaturated solid solution can sometimes trigger precipitation, and that the relevant parameter driving the precipitation kinetics becomes the strain accumulation rather than time. The so called dynamic precipitation induces an increase of the flow stress while deforming the material since σ_{preci} increases with increasing the radius and the volume fraction of precipitates. These precipitates are small enough to be sheared by dislocations. Dynamic precipitation is expected to increase as the strain increases. The apparent effect of dynamic precipitation on strain hardening will therefore be an increase of the dislocation storage parameter θ by a quantity called θ_{dp}. After Deschamps et al. [186], the contributions of dislocation storage and of dynamic precipitation can be added linearly. A linear relationship between the excess solute and θ_{dp} is proposed [42], i.e.

$$\theta = \theta_0 + \theta_{dp} \quad \text{where} \quad \theta_{dp} = k_{\theta dp}\left(\frac{C_{ss} - C_e}{C_0 - C_e}\right), \tag{65}$$

where $(C_{ss} - C_e)/(C_0 - C_e)$ is therefore the relative remaining excess solute. The value of $k_{\theta dp}$ is calculated from the difference between the dislocation storage parameter θ after a solution heat treatment and the minimum value $\theta = \theta_0$.

3.3.2.4. Strain hardening model – dynamic recovery term β. As extensively discussed in the presentation of the precipitates and yield strength evolution models, the yield strength and the solid solution concentration are affected by the presence of precipitates. The dynamic recovery rate β is proportional to the annihilation distance between two dislocations of opposite sign y_a. When the interaction stress between two dislocations (Gb/y_a) exceeds the yield strength, the dislocations annihilate one another. Hence, if the yield strength increases, the dynamic recovery rate β should decrease. Furthermore, if dynamic precipitation occurs, an additional increase of the yield strength takes place leading to a larger decrease of the dynamic recovery rate β. Furthermore, precipitation and dynamic precipitation cause a depletion of solid solution, increasing the intrinsic mobility of dislocations out of their plane

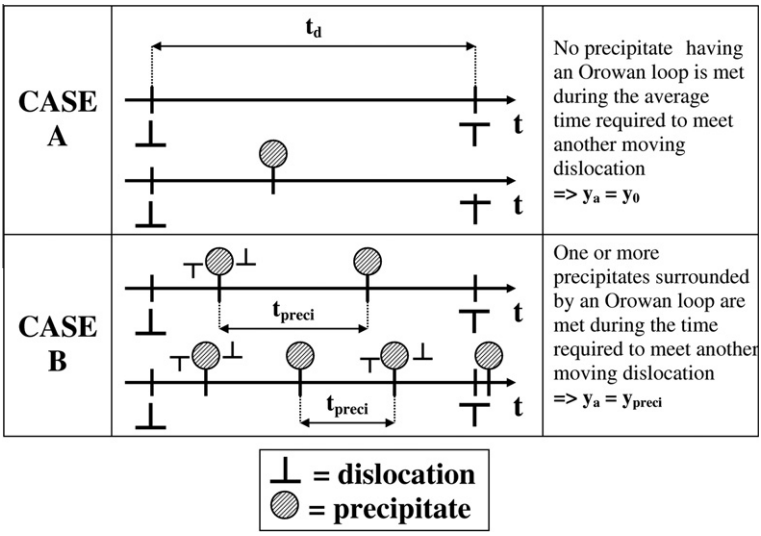

Fig. 11. Effect of the presence of a precipitate surrounded by an Orowan dislocation loop on the annihilation distance between two moving dislocations (y_a); traveling time associated to the mean spacing between two opposite dislocations t_d (s); $1/t_{preci}$ (s^{-1}) is the frequency of precipitates distribution.

by modifying the core properties of the dislocation, e.g. by increasing the stacking fault energy, which favors cross slip. The solid solution effect which is connected to the possibility of dynamic precipitation and the modification of the core properties of the dislocation is difficult to quantify due to its coupling with the yield strength evolution. Indeed, when the solid solution concentration decreases, the yield strength increases, as an indirect effect related to the precipitation, leading to a potential decrease of the dynamic recovery rate β. But, the decrease in solid solution concentration reduces the dynamic precipitation with a potential increase of the dynamic recovery rate β. For the sake of simplicity, the dynamic recovery rate β is assumed to be inversely proportional to the yield strength σ_0. The reference is the minimum value β_{min} for which the maximum yield strength σ_0^{max} is attained. The expression of the dynamic recovery rate β writes

$$\frac{1}{\beta_{min}} - \frac{1}{\beta} = k_\beta \left(\frac{\sigma_0^{max} - \sigma_0}{G} \right), \tag{66}$$

where k_β is an adimensional constant which can be evaluated by knowing the value of the dynamic recovery rate β and initial yield stress for a solution heat treated sample.

Fig. 11 explains the physics of the model proposed for the influence of the Orowan loop formation on the dynamic recovery mechanism. Two cases are possible [42]:

- *Case A.* The mean spacing between two opposite dislocations and associated traveling time t_d (s) is such that the dislocations annihilate before encountering a precipitate involving an Orowan loop. In this case, the annihilation distance with another mobile dislocation y_a[5] is equal to y_0 which is the annihilation distance when no dislocation is stored around precipitates. In that case, the dynamic recovery rate β is equal to β_0, which is the value of the dynamic recovery rate β when no Orowan loop is stored.
- *Case B – "The dislocation lift effect".* At least one precipitate is met during the interval time t_d and this precipitate is surrounded by an Orowan loop. In that case, the dislocation will partially and locally annihilate with the Orowan loop favoring a change of glide plane. Consequently, the dislocation

[5] Distance under which two dislocations undergo a force field large enough to allow cross slip resulting in annihilation.

glide is"de-localized" and the effective annihilation distance with another mobile dislocation y_a will be larger. The apparent recovery rate β will increase up to β_{preci}. If the dynamic recovery rate β can be interpreted via the critical annihilation distance y_{preci} at the precipitate/matrix interface, $\beta_{preci} \approx 2y_{preci}/b$, independent of the precipitate radius.

Case A and B can take place simultaneously when deforming an alloy containing precipitates around which Orowan loops are stored. Let $p(0)$ be the probability to have no precipitate between two dislocations that would potentially annihilate one another (case A). The value of y_a then writes

$$y_a = y_0 p(0) + y_{preci}(1 - p(0)), \tag{67}$$

or equivalently, if β_{preci} can be interpreted via the critical annihilation distance y_{preci},

$$\beta = \beta_0 p(0) + \beta_{preci}(1 - p(0)). \tag{68}$$

An estimate for $p(0)$ is required. By definition, the traveling time writes $t_d = L_0/v_r$, where L_0 (m) is the mean distance between two mobile dislocations of opposite sign and v_r (m/s) is the relative velocity of two moving dislocations. Another traveling time interval t_{preci} is defined as $t_{preci} = l/v_r$, where l (m) is the precipitates spacing in the glide plane of the dislocations given by Eq. (44). The mean number v of precipitates encountered before two moving dislocations meet is $v = t_d/t_{preci}$. Hence, the mean number v_φ of precipitates having an Orowan loop efficiently stored around it encountered before two moving dislocations meet is $v_\varphi = v\,\varphi$, where φ is the efficiency of dislocation storage, i.e. the probability of an Orowan loop to survive the deformation process. Consequently, the following expression for v_φ is proposed

$$v_\varphi = \varphi \frac{t_d}{t_{preci}} = \varphi \frac{L_0}{l} = \sqrt{\frac{3}{2\pi}} \frac{\sqrt{f_v} L_0 \varphi}{r}. \tag{69}$$

Using a Poisson probability distribution, the mean probability to meet m precipitates with an Orowan loop during the time t_d can be estimated, which requires knowing the mean number v_φ of precipitates having an Orowan loop efficiently stored and encountered before two moving dislocations meet. This mean probability $p(m)$ writes

$$p(m) = \frac{v_\varphi^m}{m!} exp(-v_\varphi). \tag{70}$$

Hence, the probability $p(0)$ that a dislocation meets no precipitate involving an Orowan loop during the time t_d is given by (using expression (44) to calculate l)

$$p(0) = exp(-v_\varphi) = exp\left(-\sqrt{\frac{3}{2\pi}} \frac{\sqrt{f_v} L_0 \varphi}{r}\right). \tag{71}$$

3.3.2.5. Final expressions for θ and β. Accounting for Orowan loop formation and dynamic precipitation leads to

$$\frac{\theta}{G} = \frac{\theta_0 + \theta_{dp}}{2G} + \sqrt{\left(\frac{\theta_0}{2G}\right)^2 + \alpha^2 M^3 \beta \varphi \left(\frac{b}{r}\right) \sqrt{\frac{3 f_v}{2\pi}}}. \tag{72}$$

Accounting for Orowan loop formation and for the effect of the yield strength on dynamic recovery leads to

$$\beta = \beta_0 exp\left(-\sqrt{\frac{3}{2\pi}} \frac{\sqrt{f_v} L_0 \varphi}{r}\right) + \frac{2y_{preci}}{b}\left(1 - exp\left(-\sqrt{\frac{3}{2\pi}} \frac{\sqrt{f_v} L_0 \varphi}{r}\right)\right). \tag{73}$$

In Eqs. (72) and (73), the evolution of φ with the precipitate radius is given by Eq. (64). The evolution of θ_{dp} with the solid solution concentration is provided by Eq. (65). The evolution of β_0 with the initial yield strength is given by Eq. (66). The precipitate radius used in the strain hardening model is the mean radius, i.e. the contributions of the radius of each type of precipitate multiplied by its volume fraction are added and the total is divided by f_v. Table 5 summarizes the parameters used for modeling the strain hardening behavior of 6005A [42] and 6056 Al alloys. In Section 4.2.4, this strain hardening model will be validated on micro-tensile tests performed across 6005A-T6 and 6056-T78 welds, probing the various zones of the weld.

3.3.2.6. Stage IV hardening. As discussed by Nes [188], Kocks and Mecking [177], and Argon and Haasen [203], large strain experiments, performed under torsion or shear, demonstrate that the decrease of the hardening rate is interrupted by a constant hardening stage, referred to as stage IV. Stage IV hardening corresponds to the increasing misorientation among dislocation cells built during stage III [177,188]. Simar et al. [5] have estimated this constant stage IV hardening rate θ_{IV} on heat treated samples of 6005A Al alloy. They concluded that stage IV hardening must be accounted for when modeling damage, which often develops at large local strains. Simar et al. [5] found a simple correlation between the true strain at necking ϵ_u and θ_{IV} which will be used in the following: θ_{IV}/ϵ_u = 650 MPa. In absence of any other information, the same correlation will be assumed to hold true for the 6056 alloy. Eq. (54) is modified as suggested by Liu [204] to account for a smooth transition to stage IV hardening, see also Fig. 2 of Simar et al. [5]:

$$\frac{d\sigma_y}{d\varepsilon_p} = \theta - \beta(\sigma_y - \sigma_0 - \theta_{IV}\varepsilon_p) + \theta_{IV}. \tag{74}$$

3.4. Damage model for Al alloys

Ductile materials always involve damage accumulation when deformed to large plastic strains. In Al alloys, damage is caused by the nucleation of voids on intermetallic particles that are about three orders of magnitude larger than the strengthening precipitates described in Section 3.2.1. The growth and coalescence of these voids will eventually lead to the final fracture of the material due to the propagation of a crack resulting from the coalescence of several voids. Micro-mechanics type damage models can be used to estimate the fracture strain based on the predicted tensile properties from Section 3.3 and distribution parameters associated to the intermetallic phase. This section first provides a description of the non-hardening precipitates in Al alloys (i.e. the intermetallic phases). The damage mechanisms in Al alloys will be described in Section 3.4.2. In Section 3.4.3, the micro-mechanics based damage model relying on Gurson's formalism [205] will be presented. Finally, Section 3.4.4 will show how the damage model can be applied to 6xxx series Al with an emphasis on the 6005A and 6056 alloys. Later, in Section 4.2.6, the damage model will be validated towards experimental measurements of the broken section area of tensile specimens of friction stir welds in both Al alloys.

3.4.1. Non-hardening precipitates in Al alloys

During the casting of industrial Al alloys of the series 6xxx, the presence of Fe, Mn and Cr leads to the formation of incoherent coarse phases. These phases can be classified into two separate categories: the intermetallics which are iron rich precipitates, and the dispersoïds which are Mn and/or Cr rich precipitates. The intermetallic particles and dispersoïds are the particles on which damage nucleates in Al alloys [3,5,34,206–210].

Intermetallics are Al–Fe, Al–Fe–Si and Al–Fe–Mn–Si type particles formed between the Al dendrites during the cooling of the cast [211]. These phases have a typical size of around 1–10 μm. The homogenization treatment that follows casting aims, among others, at transforming interconnected plate-like β-Al_5FeSi into more rounded and discrete α-$Al_{12}(FeMn)_3$ and at dissolving coarse Mg_2Si precipitates [3,212].

Dispersoïds are α-Al (FeMn) phases formed on purpose during the homogenization of the alloy to control the recrystallisation. The typical size of these phases is about 100 nm. They heterogeneously

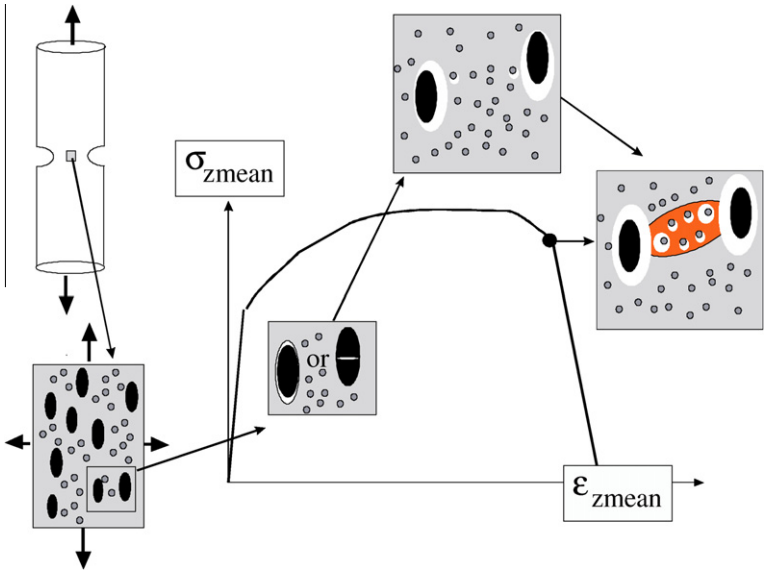

Fig. 12. Schematic description of the sequence of damage mechanisms occurring in metallic alloys and leading to ductile failure.

precipitate on β' phases during the homogenization treatment and are incoherent with the Al matrix. The β' phases segregate towards the dendrite boundaries during casting [213] and later dissolve during a homogenization treatment. This explains the inhomogeneous distribution of dispersoïds within the Al matrix [214].

3.4.2. Damage mechanisms in Al alloys

Fig. 12 schematically presents the phenomenology of ductile failure. The reader is referred also to the comprehensive reviews by Pineau [215], Tvergaard [216], Lassance et al. [3], Pineau and Pardoen [4], Pardoen et al. [10] and Benzerga and Leblond [8]. A macroscopic specimen, here containing a notch, is deformed in tension. Damage accumulates faster in the center of the minimum section of the bar where the highest stress triaxiality as well as large plastic strains, the two main parameters in ductile fracture [217]. Damage in a ductile material is characterized by the nucleation, growth and coalescence of small internal voids. These voids generally nucleate by the fracture or decohesion of second phase particles [218] such as the intermetallics found in Al alloys [3,5,32,207,208,210,219]. The voids then grow by plastic deformation [8]. Void coalescence consists in the localization of plastic deformation at the micro-scale inside the intervoid ligament between neighboring voids [220]. Earlier void coalescence can be favored by the presence of secondary voids nucleated on a second population of smaller particles such as on the dispersoïds in Al alloys [209,221–224].

In the model presented in the next section, the detrimental effect of precipitate free zones (PFZ) on ductility is not considered, see Pardoen et al. [10,225] for an example of application of the Gurson formalism to PFZ or Steglich et al. [226] for precipitate free bands. Indeed, the presence of precipitate free zones does not particularly affect 6xxx series aluminum alloys but is a major concern when treating the ductility of high strength aluminum alloys, in particular in the 7xxx series aluminum alloys.

3.4.3. Model description

Comprehensive literature survey on the micro-mechanics based damage models are available in review papers [3,4,8,8,10]. Only the main ingredients and equations of a generic damage model used in the model chain will be presented. The model is based on the work by Pardoen and Hutchinson [227,228] which relies on the Gurson formalism [205] as enhanced by Tvergaard et al. [229],

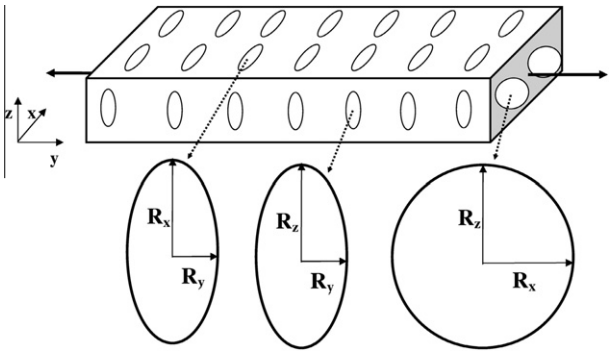

Fig. 13. Definition of the void radius assuming a spheroidal shape ($R_z = R_x$) with respect to the main loading axis.

Needleman et al. [230], Gologanu et al. [231] (void morphology), Benzerga et al. [2], Thomason [220] for the void coalescence condition.

3.4.3.1. Main geometrical void parameters. The voids are described by the following parameters:

- f is the porosity, i.e.the volume fraction of voids, with f_0 the initial value.
- W is the mean aspect ratio of the voids. The voids are assumed spheroidal, which signifies a circular section in a plane transverse to the main void axis y (i.e. $R_x = R_z$, where R_x or R_z is the radius of the circular section). The logarithmic aspect ratio of the voids is defined as $S_v = ln(W) = ln(R_y/R_x)$. The initial values are designated S_{v0} and W_0. Fig. 13 clarifies the definition of W.
- λ_d is the particle distribution factor. Here, we will assume that the voids are uniformly distributed leading to $\lambda_d = 1$.
- χ is the relative void spacing and is defined as

$$\chi = \left(\frac{f}{\gamma_d}\frac{\lambda_d}{W}\right)^{\frac{1}{3}}, \tag{75}$$

where γ_d is a geometric factor which depends on the arrangement of voids. Here, we will assume that the voids are distributed in a simple periodic cubic array (i.e. $\gamma_d = 0.605$), see Fig. 13.

3.4.3.2. Void nucleation. The decohesion or fracture of a particle is assumed to occur when the maximum principal stress in the particle or at the interface with the matrix $(\sigma^{particle}_{princ})^{max}$ reaches a critical value σ_c. The maximum principal stress in the particle can be related to the overall stress state by using [232–234]:

$$\left(\sigma^{particle}_{princ}\right)^{max} = \sigma^{max}_{princ} + k_s(\sigma_{eq} - \sigma_0), \tag{76}$$

where σ^{max}_{princ} is the maximum overall principal stress, σ_{eq} is the von Mises equivalent stress, and k_s is a parameter of the order of unity which is a function of the inclusion shape and of the loading direction [235], see also Tekoğlu and Pardoen [236] for a more advanced formulation. The rate of increase of the void volume fraction associated to the nucleation of new voids $\dot{f}_{nucl}$ is taken as a function of the plastic strain

$$\dot{f}_{nucl} = g(\varepsilon_p)\dot{\varepsilon}_p, \tag{77}$$

where ε_p is the equivalent plastic strain of the matrix material, $g(\varepsilon_p)$ takes a polynomial form described in Lassance et al. [3] and nucleation is assumed to occur over a strain range equal to $\Delta\varepsilon_{nucl}$. The fact that void nucleation occurs over a strain interval implies that voids will be nucleated with an already

evolving void aspect ratio ($W > W_0$). As discussed in Lassance et al. [3], this can be approximately accounted for by correcting the porosity to be nucleated as a function of the current void aspect ratio as $f_0^{(eff)} = f_0 W/W_0 = f_p W/W_p$ (f_p is the particle volume fraction and W_p is the particle aspect ratio).

3.4.3.3. Void growth. Based on volume conservation during plastic deformation, the increase of the void volume fraction writes

$$\dot{f} = (1-f)\dot{\varepsilon}^p_{ii} + \dot{f}_{nucl}, \tag{78}$$

where $\dot{\varepsilon}^p_{ij}$ are the ij components of the overall plastic strain tensor. The evolution law for S_v has been derived by Gologanu et al. [231] from the micro-mechanical analysis of the growth of spheroidal voids in a J2 perfectly plastic material as

$$\dot{S}_v = \frac{3}{2}(1+h_1)\left(\dot{\varepsilon}^p - \frac{\dot{\varepsilon}^p_{ii}}{3}\delta_K\right) : P_d + h_2\dot{\varepsilon}^p_{ii}, \tag{79}$$

with analytical expressions for h_1, h_2 as a function of S_v and f; P_d is a projector tensor, defined by $e_y \otimes e_y$ (e_y is a unit vector parallel to the main cavity axis[6]); δ_K is the Kronecker tensor. The hardening behavior of the matrix material is related to the overall stress and plastic strain rate through the energy balance initially proposed by Gurson [205]:

$$\sigma_y \dot{\varepsilon}^p_y (1-f) = \sigma \dot{\epsilon}^p, \tag{80}$$

where the mean flow strength of the matrix σ_y is a function of the mean plastic strain ε^p_y. In order to calculate the evolution of the variables f and S_v as well as the stress state σ_{ij}, use is made of the associated flow rule

$$\dot{\varepsilon}^p_{ij} = \dot{\gamma}\frac{\partial \Phi}{\partial \sigma_{ij}}, \tag{81}$$

where Φ is the flow potential proposed by Gologanu et al. [231] for a porous material involving spheroidal voids:

$$\Phi = \frac{C}{\sigma_0^2}\left\|\sigma' + \eta_d \sigma^g_h X\right\|^2 + 2q(g+1)(g+f)\cosh\left(\kappa\frac{\sigma^g_h}{\sigma_0}\right) - (g+1)^2 - q^2(g+f)^2 = 0, \tag{82}$$

where (see Gologanu et al. [231], Pardoen and Hutchinson [227], Benzerga et al. [2], Pardoen [237] for more details)

- σ' is the deviatoric tensor part of the Cauchy stress tensor;
- σ^g_h is a generalized hydrostatic stress defined by $\sigma^g_h = \sigma : J$; J is a tensor associated to the void axis and defined by

$$J = (1-2\alpha_2)e_y \otimes e_y + \alpha_2 e_x \otimes e_x + \alpha_2 e_z \otimes e_z; \tag{83}$$

- X is a tensor associated to the void axis and defined by

$$X = \frac{2}{3}e_y \otimes e_y - \frac{1}{3}e_x \otimes e_x - \frac{1}{3}e_z \otimes e_z; \tag{84}$$

- $\| \ \|$ is the von Mises norm;
- C, η_d, g, κ and α_2 are analytical functions of the state variables S_v and f;
- q is a parameter that has been calibrated as a function of f_0, W_0 and the strain hardening exponent n.

The stresses are calculated from

[6] For the sake of simplicity, we will assume here that the main void axis e_y does not rotate and that it remains parallel to the loading direction, i.e. the y direction.

$$\dot{\sigma}_{ij} = L_{ijkl}\left(\dot{\varepsilon}_{kl} - \dot{\varepsilon}^{p}_{kl}\right), \tag{85}$$

where L_{ijkl} are the elastic moduli.

3.4.3.4. Void coalescence. The first stage of void growth by relatively homogeneous plastic deformation of the matrix surrounding the voids is interrupted by the localization of the plastic flow in the ligament between the voids. This localization corresponds to the onset of coalescence. From that point on, void coalescence starts, driven by plasticity localized between the primary voids. The problem is similar to an internal necking process at a micro-scale. Thomason [220] proposed the following condition for the onset of coalescence by internal necking:

$$\frac{\sigma_{yy}}{\sigma_0(1 - r_g\chi^2)} = \alpha_d\left(\frac{1-\chi}{\chi W}\right)^2 + 1.24\sqrt{\frac{1}{\chi}}, \tag{86}$$

where r_g is a geometric factor which depends on the void arrangement (in a cubic cell, $r_g = \pi/4$) and parameter α_d has been fitted as a function of the average value of the strain hardening exponent n by Pardoen et al. [227] for $0 \leqslant n \leqslant 0.3$

$$\alpha_d(n) = 0.1 + 0.22n + 4.8n^2. \tag{87}$$

In the case of the hardening law used in this work, see Eq. (74), the corresponding strain hardening exponent is not constant. The Considère criterion, stating the true strain at necking ε_u is equal to the strain hardening exponent, is used to provide an estimate of an average n noted $\langle n\rangle$, i.e. $\langle n\rangle \approx \varepsilon_u$, to be used in Eq. (87), see Lecarme et al. [238] for a more elegant approach. Criterion (86) states that coalescence occurs when the stress normal to the localization plane reaches a critical value. This critical value decreases as the voids open (i.e. W increases) and get closer to each other (i.e. χ increases). Hence, the dominant parameter controlling the transition to the coalescence mode is the relative void spacing χ. The porosity affects the coalescence indirectly through the link with the void spacing χ and through its softening effect on the applied stress σ_{yy}. In the present study, coalescence by internal necking is assumed to occur in a band normal to the main void axis which is certainly an approximate in the case of shear-driven void sheet coalescence mechanism, see Scheyvaerts et al. [239,240] for a more advanced formulation.

3.4.3.5. Influence of a second population of voids on coalescence. As discussed in Section 3.4.1, industrial Al alloys generally contain dispersoïds in addition to the larger intermetallics. The dispersoïds can intervene in the damage process as second population of cavities [34,208–210,223,224,241,242]. The schematic of Fig. 12 shows how these secondary voids, represented by dark gray small circles, intervene in the damage process. A second population of cavities generally nucleate after the primary voids, especially within the ligament between these primary voids in which the deformation is the largest. Fabrègue et al. [223,224] have shown that the secondary voids do not affect the primary void growth. Fabrègue et al. [223,224] also suggested a phenomenological correction to the Thomason [220] criterion

$$\frac{\sigma_{yy}}{(1-f_2)\sigma_0(1 - r_g\chi^2)} = \alpha_d\left(\frac{1-\chi}{\chi W}\right)^2 + 1.24\sqrt{\frac{1}{\chi}}, \tag{88}$$

where f_2 is the volume fraction of secondary voids growing in the ligament between the primary voids. The evolution of f_2 with strain is also calculated by Fabrègue et al. [223,224] using a closed form model but, for simplicity and reducing the calculation time, we will assume that the secondary voids grow at a rate K_2 proportional to the equivalent plastic strain (see [6])

$$f_2 = K_2(\epsilon_p - \epsilon_{p,nucl2}), \tag{89}$$

where $\epsilon_{p,nucl2}$ is the equivalent plastic strain at the nucleation of the secondary voids. The secondary voids are assumed to nucleate when the maximum principal stress in the particle or at the interface with the matrix $(\sigma^{particle}_{princ})^{max}$ reaches a critical value σ_{c2} following Eq. (76).

Table 6
Parameters of the micro-mechanics based damage model, see Simar et al. [5].

Parameter	Symbol	Value 6005A	Value 6056
Volume fraction of intermetallic particles	f_p	1.2%	0.93%
Aspect ratio of intermetallic particles	W_p	0.59	0.85
Initial aspect ratio of nucleated voids	W_0	0.01	0.01
Nucleation stress	σ_c	400 MPa	400 MPa
Extend of nucleation	$\Delta\sigma_{nucl}$	200 MPa	200 MPa
Nucleation condition parameter	k_s	1.0	1.0
Nucleation stress for secondary voids	σ_{c2}	600 MPa	600 MPa
Rate of growth of a second pop. of voids	K_2	1.2	1.2

3.4.4. Application to 6xxx series Al alloys

In this section, the identification of the different parameters entering the damage model are described. The objective is to rely as much as possible on microstructural data obtained experimentally with a minimum number of adjusting parameters.

Simar et al. [5] have shown that in the 6005A Al alloy the intermetallic particles break during deformation at room temperature. When void nucleation results from the fracture of brittle (elastic) particles, a stress controlled criterion can be justified by a fracture mechanics argument: the particles contain internal defects which lead to cracking when the particle fracture toughness is reached, the stress intensity factor being proportional to the applied stress, see Shabrov et al. [243], Lassance et al. [244] and Tekoğlu and Pardoen [236] for a more complete description concerning the use of a stress controlled nucleation law in the case of particle fracture. In the present model chain, it is chosen to iteratively introduce a stress controlled nucleation distribution law even though the numerical code is written with a strain controlled nucleation distribution law. The term $\Delta\,\sigma_{nucl}$ is defined as the distribution of void nucleation stress that should correspond to the $\Delta\varepsilon_{nucl}$ in the nucleation law, Eq. (77). The code works by iterations. An initial $\Delta\varepsilon_{nucl}$ is imposed. The stress in the particle is calculated by Eq. (76). Then, the calculation is restarted with an increased or decreased $\Delta\varepsilon_{nucl}$ with the aim to reach a stress in the particle after complete nucleation equal to $\sigma_{nucl} + \Delta\sigma_{nucl}$. Since nucleation occurs by particle fracture, the initial void aspect ratio is very low. Hence, a small value of the initial void aspect ratio is selected, $W_0 = 0.01$, see Huber et al. [207]. As a result, the initial volume fraction of voids is given by $f_0 = W_0 f_p / W_p$. Table 6 summarizes the parameters used for the damage model for the 6005A and 6056 Al alloys. Note that only the microstructure parameters (i.e. f_p and W_p) are alloy dependent. These parameters, related to the intermetallic particles, have been obtained by image analysis performed on SEM micrographs in both alloys [5,34].

Simar et al. [5] have shown that heat treated 6005A tensile specimens involve two populations of cavities on their fracture surface if the material is in a hard state (typically in the T6 state). Gallais et al. [34] have shown that friction stir welds made of AA6056-T78 present a second population of cavities on their fracture surface. The presence of a second population of cavities plays a more significant role at high stresses, hence one can expect this phenomenon to have a larger impact on the fracture strain of 6056-T78 welds than on the fracture strain of 6005A welds as verified experimentally [6,34]. Furthermore, Al–Mg–Si–Cu heterogeneous precipitation on the dispersoïds as observed in the thermomechanically affected zone of 6056-T78 friction stir welds [34,54] tends to increase the apparent size of the dispersoïds. Fig. 14 compares the fracture surfaces of a 6005A-T6 weld and of a 6056-T78 weld. In the low strength material, i.e. the 6005A alloy show no evidence of a second population of cavities while, in the high strength alloy, i.e. the 6056 alloy, secondary voids are clearly observed. The stress required to nucleate voids on dispersoïds is much higher than the one for the iron rich intermetallics because of the smaller size and associated lower size of interface or internal defects. This high nucleation stress is apparently not reached in this 6005A weld while it is attained in the 6056 welds.

The parameter K_2, controlling the rate of growth of the secondary voids, is identified from the response of the base material 6056-T78 in the following way. The yield strength and strain hardening parameters of the base material have been used in a J_2 finite element simulation of a tensile test, i.e. no damage is involved in the simulation. By extracting the evolution of the stress triaxiality with

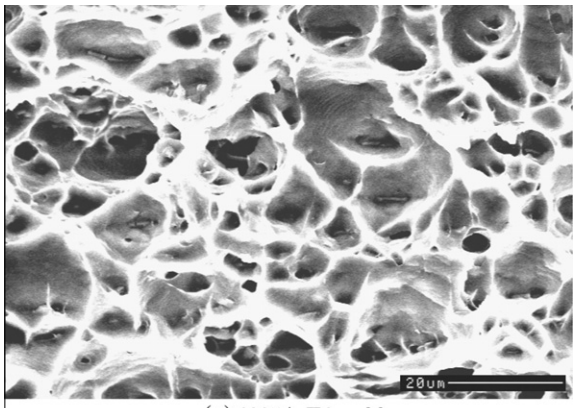

(a) 6005A-T6 weld

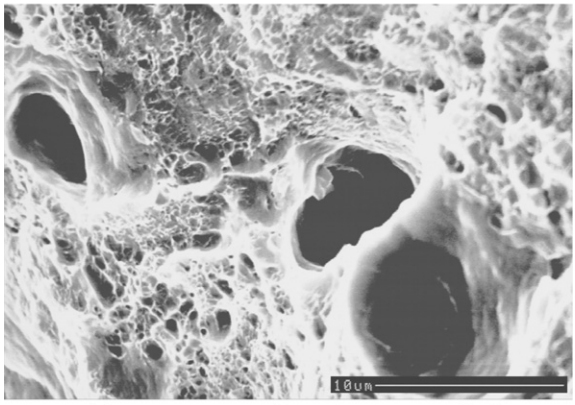

(b) 6056-T78 weld (from Gallais *et al.* [34])

Fig. 14. Fracture surface of a 6005A-T6 and 6056-T78 welds deformed in tension perpendicular to the weld line. Both samples have fractured in the weakest heat affected zone. The 6056 weld (b) presents a second population of cavities contrarily to the 6005A weld (a).

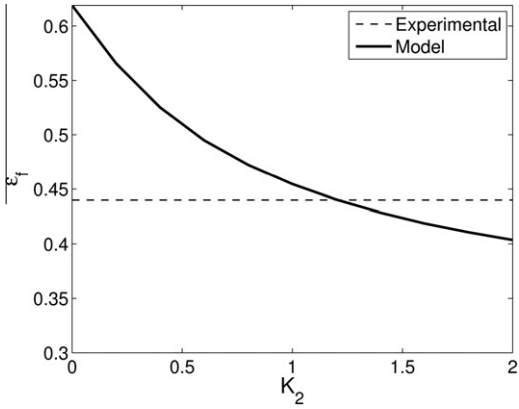

Fig. 15. Evolution of the fracture strain predicted by the damage model for the 6056-T78 base material with a nucleation stress for secondary voids $\sigma_{c,nucl2}$ equal to 600 MPa.

Table 7
Summary of the models described in Section 3. FE = finite element and KME = Kocks–Mecking–Estrin.

Model type	Selected model	Inputs	Outputs	References with validation
Thermal	FE model with heat transfer involving an estimated velocity field	Power input (torque) contact conditions (tool workpiece and workpiece/backing plate interfaces) thermal properties of the material	Thermal cycles during the FSW process	[49,42] Section 4.2.2
Microstructure evolution	Size class model with possible heterogeneous precipitation of quaternary phases (e.g. Q phase)	Thermal cycle precipitation sequence thermodynamic and kinetic data	Radius size distribution ss concentration	[42,54] Section 4.2.3
Yield strength and strain hardening	Adding contributions to σ_0 of solid solution and precipitates + KME strain hardening model accounting for precipitation	Precipitate radius and volume fraction ss concentration mechanical material parameters	Tensile properties (σ_0, θ, β and θ_{IV})	[42] Section 4.2.4
Damage	Void nucleation + extended Gurson model for void growth and shape evolution + Thomason coalescence criterion with secondary voids	Tensile properties intermetallic phase volume fraction and shape	Volume fraction of voids and shape at fracture fracture strain	[34,5,6] Section 4.2.6

plastic deformation in the most deformed element, the damage model is run in "post-processing" with and without a second population of cavities (this is thus a so-called "non-coupled damage modeling"). Without a second population of cavities, the predicted fracture strain ε_f is equal to 0.62 while it is equal to 0.44 experimentally (see Table 9 and Gallais et al. [34]). The true fracture strain is defined as $\varepsilon_f = ln(A_i/A_f)$ where A_i and A_f are respectively the initial and deformed area of the cross-section containing the critical element. Fig. 15 presents the evolution of the fracture strain with a second population of cavities as a function of K_2. The nucleation stress of the second population of cavities $\sigma_{c,nucl2}$ is selected to be 600 MPa, as suggested by Gallais et al. [34]. It will be shown in Section 4.2.6 that, with this choice of $\sigma_{c,nucl2}$, no secondary voids nucleation is predicted in the 6005A-T6 welds as verified experimentally, see Fig. 14. The experimental fracture strain of the base material 6056-T78 tensile test specimens (i.e. $\varepsilon_f = 0.44$) is correctly predicted with $K_2 = 1.2$ (see Table 6). Micro-tensile specimens extracted from the weak heat affected zone of a 6056-T78 weld, with an initial yield strength equal to 165 MPa, present an experimental fracture strain equal to 0.67 and a predicted fracture strain without secondary voids equal to 0.63. Using $\sigma_{c,nucl2} = 600$ MPa, no secondary damage is predicted. Now, it will be shown in Section 4.2.6, that in the transverse tensile test on welded specimens, secondary voids play a significant role in reducing the fracture strain due to a higher level of stress triaxiality in the weakest zone of the welds (elevating thus the magnitude of the maximum principal stress) compared to homogeneous micro-tensile specimens.

3.5. Conclusions

This section described the models that will be used in the integrated modeling discussed in the next section. Table 7 summaries all these models and provides a summary of the required input data and the output data as well as the references where more details on model validation can be found.

4. Integrated modeling applied to friction stir welding

4.1. Principles of the integrated chain modeling

Fig. 1 describes the chaining of models used to link the process parameters and material properties to the end-use properties of the welds. It involves a thermal model, a microstructure evolution model,

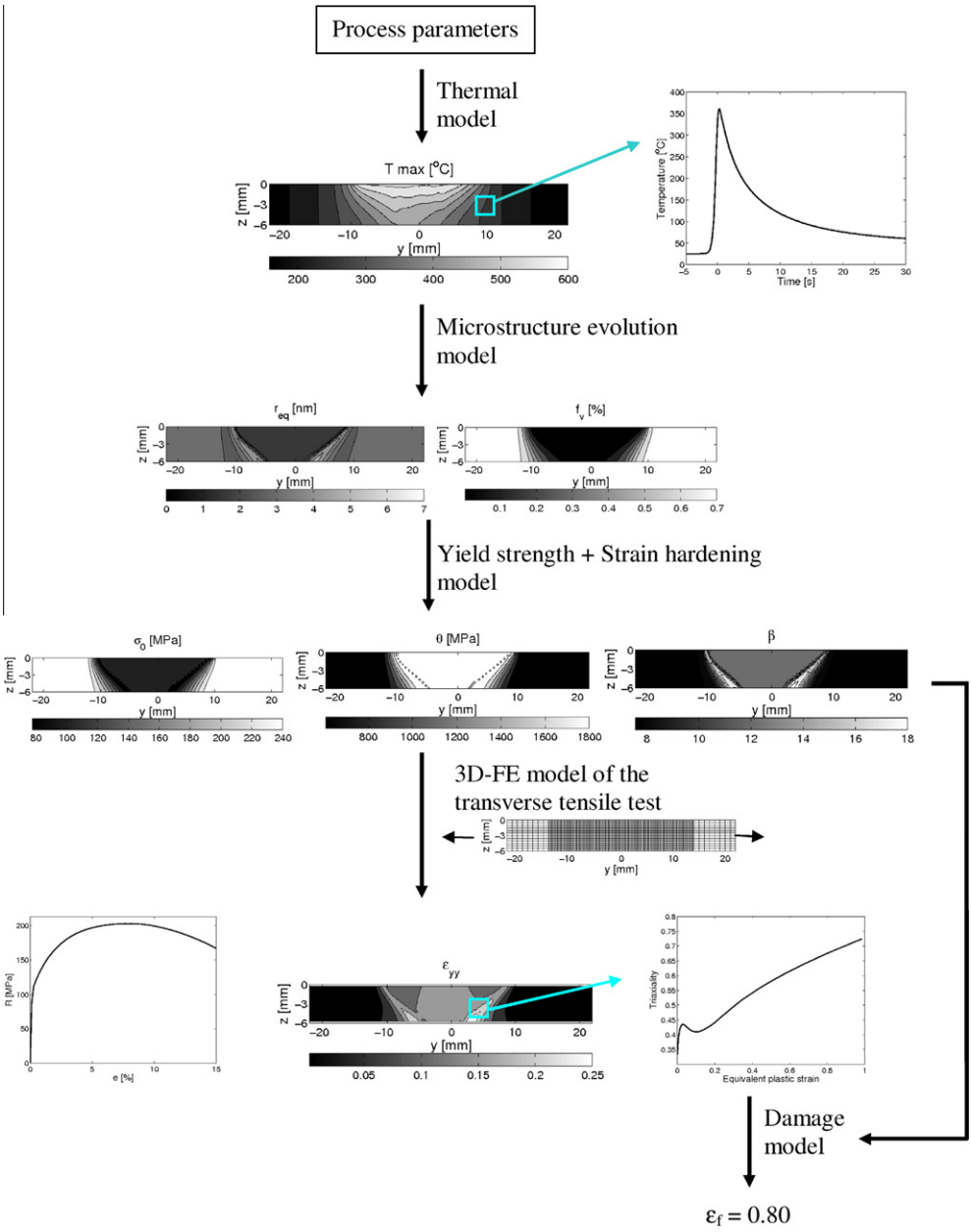

Fig. 16. Principle of the integrated chain modeling applied to a friction stir weld made of a 6005A Al alloy with an advancing speed of 1000 mm/min and a rotational speed of 1000 rpm. The following parameters and their distribution on a transverse section (z is the thickness and y is perpendicular to the welding direction) are calculated by the model: T_{max} is the maximum temperature, r_{eq} is the equivalent radius, f_v is the volume fraction of precipitates, σ_0 is the initial yield strength, θ and β are the strain hardening parameters, ϵ_{yy} is the local strain in the loading direction, e is the engineering strain, R is the engineering stress and ε_f is the true strain at fracture.

a dislocation based model for hardening and strain hardening, a macro-mechanics model of a welded component and a micro-mechanics based damage model. The primary goal of this model chain is the

prediction of the effect of a variety of processing parameters, often difficult to systematically test experimentally, with the final objective to optimize the process.

Fig. 16 describes the integrated modeling procedure in the case of the friction stir welds made of 6005A Al alloy. The thermal model described in Section 3.1.2 provides the temperature cycles across the weld. The thermal cycles are transfered to the microstructure evolution model described in Section 3.2.3, particularized to the 6005A alloy, to predict the equivalent radius and volume fraction of Mg_2Si precipitates. Based on this last information, the yield strength and strain hardening models described in Section 3.3 provide the local distribution of tensile properties. The local distributions of tensile properties are then introduced in a 3D finite element model of a transverse tensile specimen involving all the zones of the weld. This model relies on J_2 elastoplasticity to predict the pseudo engineering stress–strain curve, from which the pseudo yield strength, pseudo ultimate tensile strength and pseudo engineering strain at maximum load (or pseudo uniform elongation) can be inferred. The FE simulation also provides the local stresses and strains in the weld. The stress triaxiality and plastic strain as well as the local tensile properties are transfered to the damage model described in Section 3.4.3. The element that presents the earliest coalescence will be considered to initiate fracture of the entire specimen, providing a lower bound estimate of the true fracture strain. This uncoupled approach was shown by Pardoen et al. [10] to give the same prediction of the fracture strain of a weld as the coupled simulation by Nielsen et al. [6] which is much more computationally intensive. Now, the present approach does not permit simulations of the full crack growth process.

This modeling procedure is applied also to the 6056-T78 welds, with the appropriate microstructure evolution model including heterogeneous precipitation and the formation of the quaternary phase Q. Furthermore, the damage model for the 6056-T78 welds involves the effect of the growth of a second population of cavities on void coalescence.

4.2. Validation on friction stir welds in 6xxx series Al alloys

The aim of this section is to validate the model chain by comparing the predictions to a variety of experimental data available for the 6005A and 6056 welds. Note that the microstructure evolution model, the yield strength and strain hardening models, as well as the damage model described in Section 3 have also been validated individually on isothermal heat treatments (see Refs. [5,42,54]).

4.2.1. Base materials

The composition of the 6005A and 6056 alloys have been determined by chemical analysis, see Table 8. Both materials contain Mg and Si as main alloying elements. The 6005A alloy has been extruded while the 6056 alloy has been rolled, both with a 6 mm thick plate geometry. Several important differences between the two alloys must be mentioned:

- According to the different amount of alloying elements, the nature of the strengthening precipitates is different for each alloy: previous work on the 6056 alloy [54] indicates that the major hardening phase in over aged condition, such as the T78 state, is the quaternary Q phase whereas the β-Mg_2Si precipitates constitute the stable phase for the 6005A composition [245]. The excess of Si is not sufficient in the 6005A alloy to favor metastable precipitation of a Q-like phase.
- Less alloying elements are available in the 6005A alloy to form strengthening precipitates.
- As a counterpart, the 6056 will be more sensitive to heterogeneous precipitation during welding [54,118].

Table 8
Composition of the 6005A and 6056 Al alloys (wt.%).

Alloy	Al	Si	Mg	Cu	Fe	Mn	Zn
6005A	98.21	0.81	0.48	0.09	0.24	0.11	0.07
6056	96.99	0.87	0.73	0.67	0.12	0.62	–

- The 6056 alloy has half the iron content of the 6005A alloy. The 6056 alloy will thus present a lower volume fraction of iron-rich intermetallics, responsible for damage nucleation (see f_p in Table 6).
- The 6056 alloy has about 6 times more Mn compared to the 6005A alloy. Consequently, the 6056 alloy will present a higher volume fraction of Mn rich dispersoïds, acting as second population of cavities, known to favor early void coalescence, hence lower the ductility.

Table 9
Tensile properties of the 6005A and the 6056 alloys in various states.

Alloy and state	6005A		6056		
	T4	T6	T4	T6	T78
Yield stress at 0.2%, σ_0 (MPa)	99	256	226	338	287
True tensile stress, σ_u (MPa)	260	299	407	372	324
True strain at onset of necking, ε_u	0.22	0.08	0.20	0.031	0.056
True fracture strain, ε_f	0.80	0.18	0.32	–	0.44
Dislocation storage rate, θ (MPa)	1872	806	1995	600	1141
Recovery rate, β	10.4	10.1	9.3	7.5	15.0

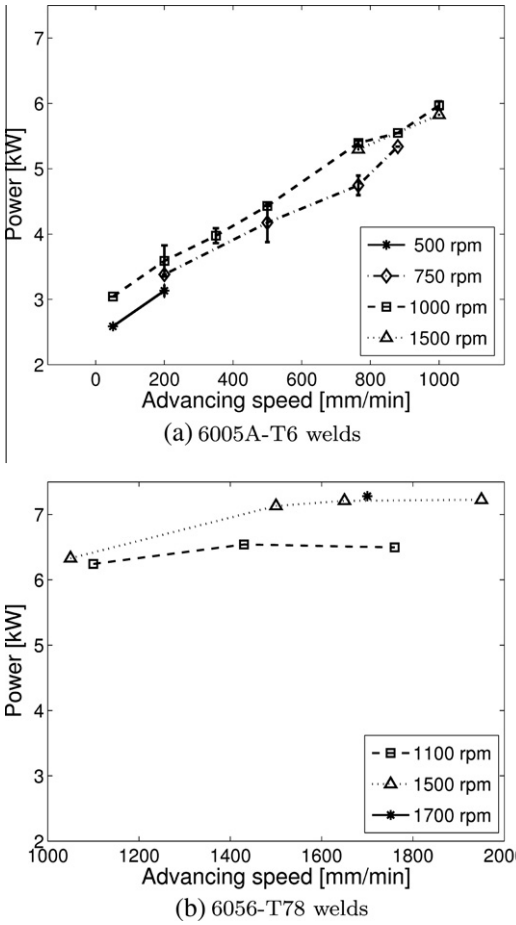

Fig. 17. Variation of the total power P estimated from the torque measurement as a function of the welding parameters.

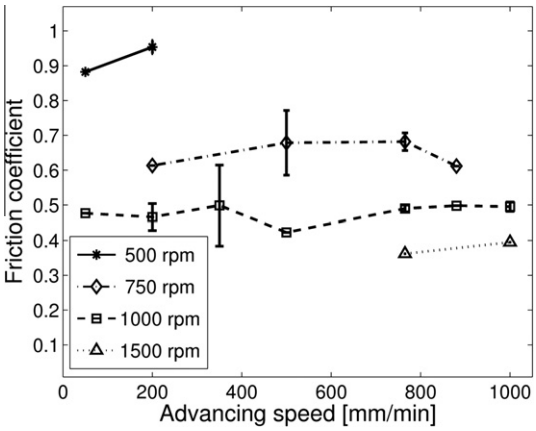

Fig. 18. Evolution of the friction coefficient with the welding parameters for the 6005A-T6 welds.

Table 9 presents the uniaxial tensile properties of the 6005A and the 6056 Al alloys for various heat treatments states. The T78 treatment is an overaged condition consisting of two successive isothermal holdings of 6 h at 175 °C and 5 h at 210 °C. The 6005A-T6 base material used in the welds is 10% weaker than the 6056-T78.

4.2.2. Validation of the thermal model

4.2.2.1. Measurement of the mechanical power. The thermal model presented in Section 3.1.2 has been applied to welds produced for a variety of conditions both for the alloy 6005A in the T6 temper and for the alloy 6056 in the T78 temper. The input of the thermal model are the total power P_{in} (W) for each welding condition which is calculated based on the rotational speed ω (rad/s), the torque M_z (Nm) and the efficiency η, as $P = \eta P_{in} = M_z\omega$ [49]. The torque has been measured during welding [49,63] (most dedicated FSW machines include a torque measurement). For the 6005A-T6 welds, the efficiency is estimated by measuring the temperature during welding at two locations on the tool away from the shoulder surface. The efficiency does almost not vary with the welding parameters and is close to $\eta \approx 0.95$ [49].

Fig. 17 shows the variation of the torque, represented in terms of the variation of the corresponding total mechanical power P as a function of the advancing speed for various rotational speeds and for both alloys. Note that the welding parameters are different in the two alloys.[7] A higher rotational speed induces only a slightly larger power. The effect of the rotational speed on the total power is more marked in the 6056 welds which could be explained by the more complex geometry of the tool (i.e. a triflute tool) compared to the 6005A welds which were performed using a simply threaded pin. The total power increases with increasing advancing speed in the 6005A-T6 welds while no pronounced effect of the advancing speed can be observed in Fig. 17b for the 6056-T78 welds. Note however that for an advancing speed equal to 1000 mm/min the power of the 6005A-T6 welds and the 6056-T78 welds is similar, probably due to a minor difference in the room temperature yield strength between the 6005A-T6 and 6056-T78 base materials, see Table 9. The variation of P with respect to the advancing speed is almost linear $P\,(\text{kW}) = 2.66 + 0.00322 \times v\,(\text{mm/min})$ [49] for low advancing speeds and tends to saturate for high advancing speeds.

4.2.2.2. Use of the vertical force to infer the mechanical power. When the measurement of the torque is not available, the measurement of the vertical force (F_z) could be used to infer the total power

[7] The welds made of the 6005A alloy were performed with a very large span of welding parameters in order to test the extreme welding parameters still giving sound welds. The welds made of the 6056-T78 alloy were performed in order to reach the best tensile performances and hence the lower advancing speeds were not tested.

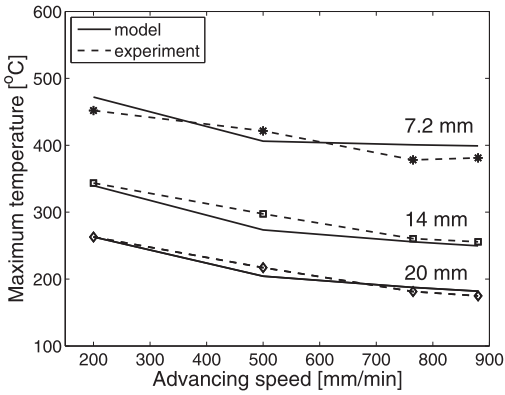

(a) 6005A-T6 welds with a rotational speed equal to 750 rpm

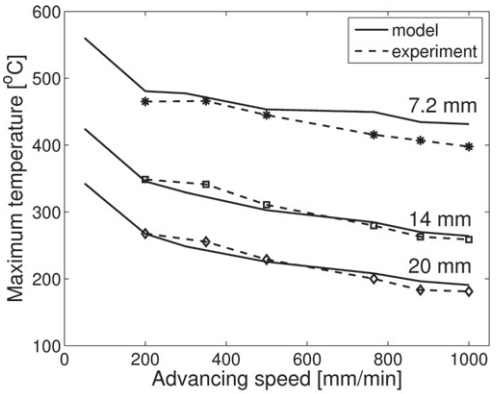

(b) 6005A-T6 welds with a rotational speed equal to 1000 rpm

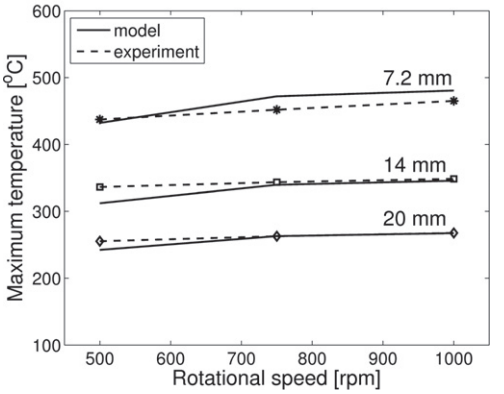

(c) 6005A-T6 welds with an advancing speed equal to 200 mm/min

Fig. 19. Assessment of the thermal model for various welding parameters applied to the 6005A alloy welds, see also Ref. [63]. Maximum temperatures at 7.2, 14 and 20 mm from the weldline on the advancing side of the weld.

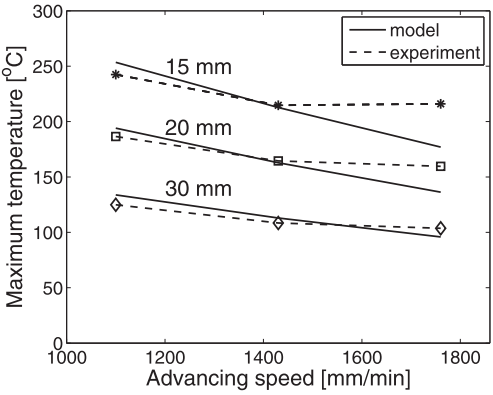

(a) Rotational speed equal to 1100 rpm

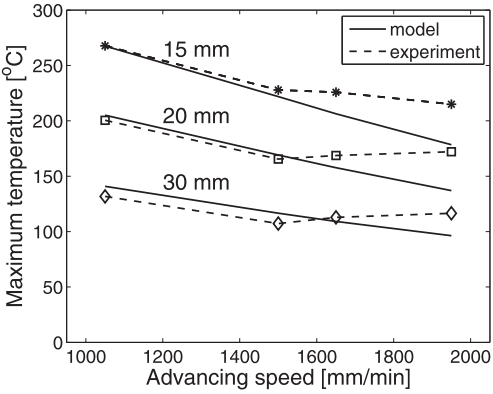

(b) Rotational speed equal to 1500 rpm

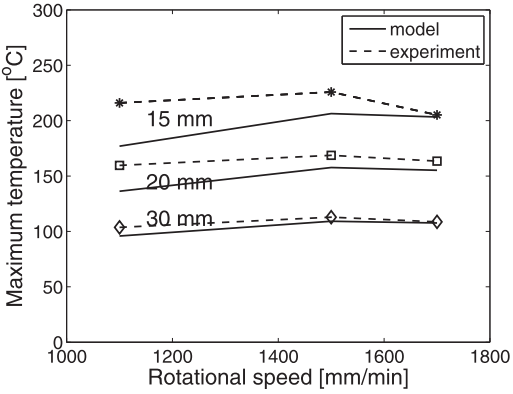

(c) Advancing speed equal to 1700 mm/min

Fig. 20. Assessment of the thermal model for various welding parameters applied to the 6056-T78 alloy welds. Maximum temperatures at 15, 20 and 30 mm from the weldline on the retreating side of the weld.

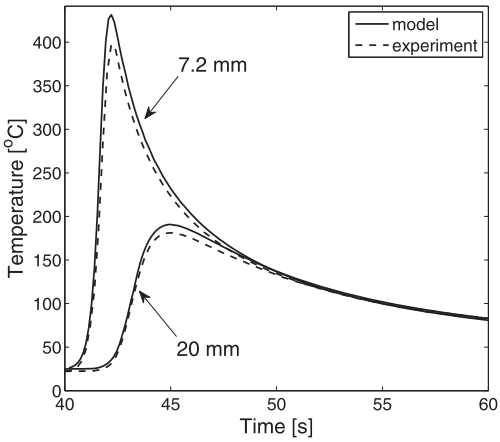

(a) Advancing speed equal to 1000 mm/min and a rotational speed equal to 1000 rpm - 6005A-T6 Al alloy.

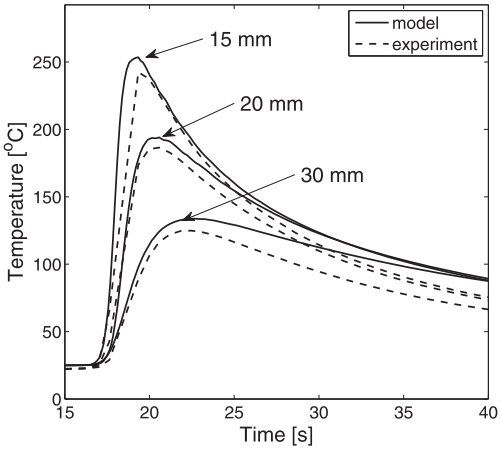

(b) Advancing speed equal to 1100 mm/min and a rotational speed equal to 1100 rpm - 6056-T78 Al alloy.

Fig. 21. Comparison of the predicted and measured thermal cycles. The arrows indicate the distance of the thermocouple from the weldline respectively (a) on the advancing side of the welds for the 6005A welds and (b) on the retreating side of the weld for the 6056 welds.

(P). Nevertheless, this is similar to assuming that the heat is entirely generated by friction. An estimate of the friction coefficient μ is thus needed. The heat generated on the surface by the friction of the tool on the material can be estimated by Eq. (90) assuming a constant pressure equal to $p_{shoulder}$ (Pa) [246] as

$$Q_S = \frac{2}{3}\pi\mu p_{shoulder}\omega r_o^3 = \frac{2}{3}\mu F_z \omega r_o. \tag{90}$$

Note that this expression neglects the pin lateral surface contribution. Another interest of this simple model is that, based on the experimental measurements of the vertical force in Ref. [119], the friction coefficient can be estimated as

$$\mu = \frac{P}{\frac{2}{3}F_z\omega r_o}. \tag{91}$$

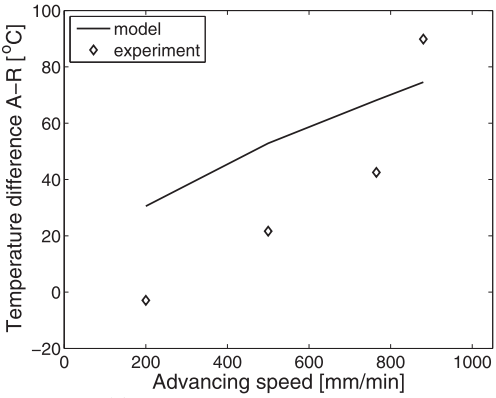

(a) Rotational speed equal to 750 rpm

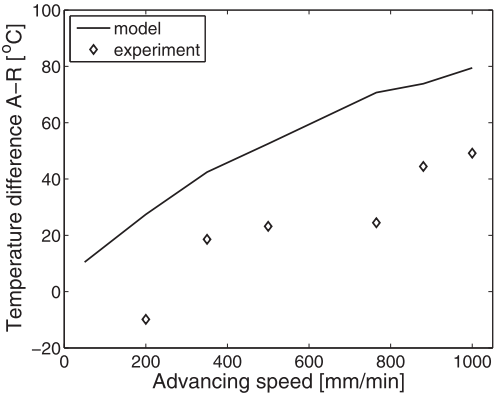

(b) Rotational speed equal to 1000 rpm

Fig. 22. Comparison of the predicted and the measured temperature difference between the advancing (A) and the retreating (R) side of the welds at 7.2 mm from the weldline for the 6005A-T6 welds as a function of the advancing speed (based on Ref. [63]).

Fig. 18 shows the evolution of the friction coefficient as estimated with Eq. (91) for different welding parameters, in the case of the 6005A-T6 welds. The friction coefficient is clearly more influenced by the rotational speed than by the advancing speed since the vertical force F_z and the power P depend more on the advancing speed than on the rotational speed and that both increase with the advancing speed. This observation indicates that the assumption of a friction coefficient independent of the rotational speed is not correct. A large variety of friction coefficient can be found in the thermal models presented in the literature. Some values are realistic like the one proposed by Frigaard [50] ($\mu = 0.4$ for an advancing speed equal to 300 mm/min, a rotational speed equal to 1500 rpm, and a shoulder diameter of 20 mm) or the one proposed by Soundararajan et al. [47] and Hamilton et al. [48] (μ varying between 0.4 and 0.5 depending on the welding parameters). Oppositely, the value proposed by Zahedul et al. [44] is quite low ($\mu = 0.15$ for an advancing speed equal to 139.7 mm/min, a rotational speed equal to 500 rpm, and a shoulder diameter of 25.4 mm).

4.2.2.3. Assessment of the thermal model. Temperature histories during welding were measured in most of the welds already addressed in Fig. 17 using thermocouples located at various positions from the weldline. The model predictions are compared to the maximum temperatures in Figs. 19 and 20. Even though the thermal model is relatively simple, it successfully captures the temperature field changes

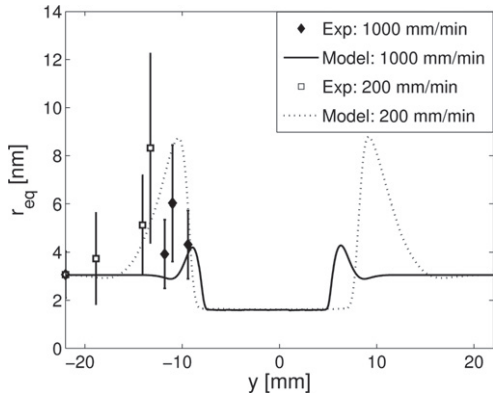

(a) 6005A-T6 welds

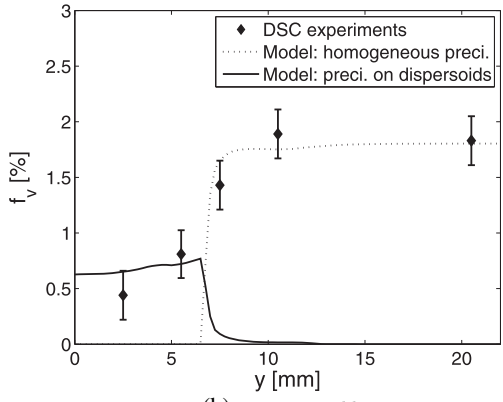

(b) 6056-T78 weld

Fig. 23. (a) Comparison for the 6005A welds of the predicted evolution of the mean equivalent precipitate radius as a function of the position in the weld to the values measured by TEM image analysis [245], value at mid-thickness. The rotational speed is equal to 1000 rpm; two advancing speeds are compared (200 mm/min and 1000 mm/min). (b) Comparison for the 6056 welds of the predicted evolution of the precipitate volume fraction and its experimental estimation by DSC measurements [54] as a function of the position in the weld, value at mid-thickness. The rotational speed is equal to 1100 rpm and the advancing speed is equal to 1100 mm/min.

with varying welding parameters. Nevertheless, the temperatures at large welding speeds are underestimated for the 6056-T78 welds. The maximum temperature away from the weldline increases as the advancing speed decreases and as the rotational speed increases. The main limit of the model is that the parameters γ and δ, governing, respectively, the proportion of heat generated as a volume heat source and the sliding ratio, should depend on the advancing and rotational speeds which is neglected here.

Fig. 21 compares the thermal history predictions at various locations with respect to the weldline for different welding parameters. The model slightly underestimates the cooling rate for the 6056-T78 welds with a possible impact on the estimates of the microstructure evolution in the next stages of the model chain.

Fig. 22 presents the temperature difference between the advancing and retreating side of the weld taken under the tool shoulder at 7.2 mm on both sides of the weldline. The predicted difference is due to the material flow around the tool which pushes hot material towards the advancing side. Colegrove et al. [247] and Schmidt and Hattel [61] concluded that the introduction of a convective heat flow

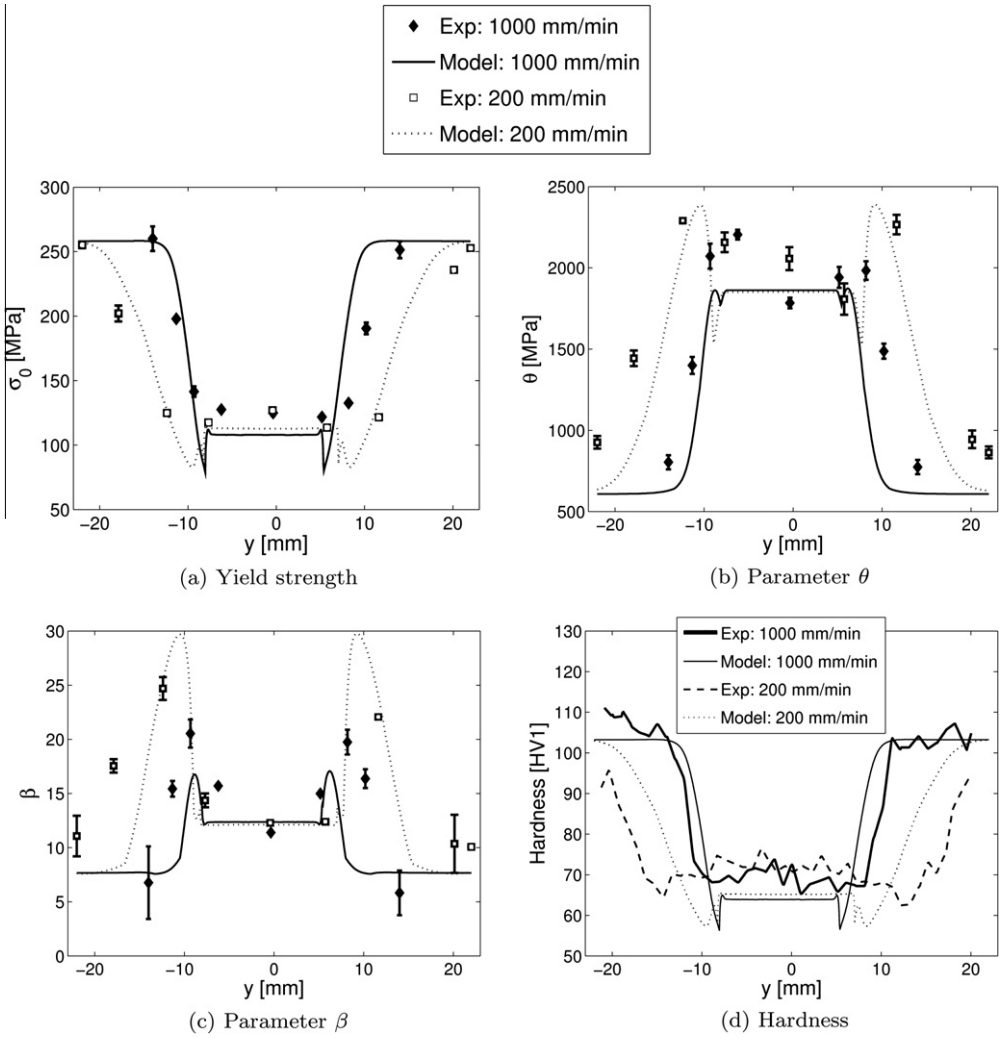

Fig. 24. Comparison for the 6005A-T6 welds of the predicted hardness and tensile properties with the hardness measured by a Vickers micro-hardness indenter with a 1 kg load as well as the measured tensile properties obtained by extracting micro-tensile specimens as a function of the position in the weld [245]; the rotational speed is equal to 1000 rpm and two advancing speeds are compared (200 mm/min and 1000 mm/min); σ_0 is the initial yield strength, θ and β are the strain hardening parameters.

induces an asymmetry in the temperature distribution making the advancing side hotter. In the present model, the material flow was estimated with the velocity field presented in Fig. 7. The model captures the trends but overestimates the temperature difference. This result confirms also that the simple description of the velocity field in Fig. 7 is sufficient for the purpose of the present study. Not accounting for this simple description of the velocity field would lead to symetric welds and prevent the prediction for instance of the side of the weld where fracture takes place (see Section 4.2.5). Furthermore, if no velocity field is introduced in the thermal model, the predicted maximum temperature at the hottest point can be, for some welding parameters, larger than the fusion temperature [63], even though the FSW process is a solid state process.

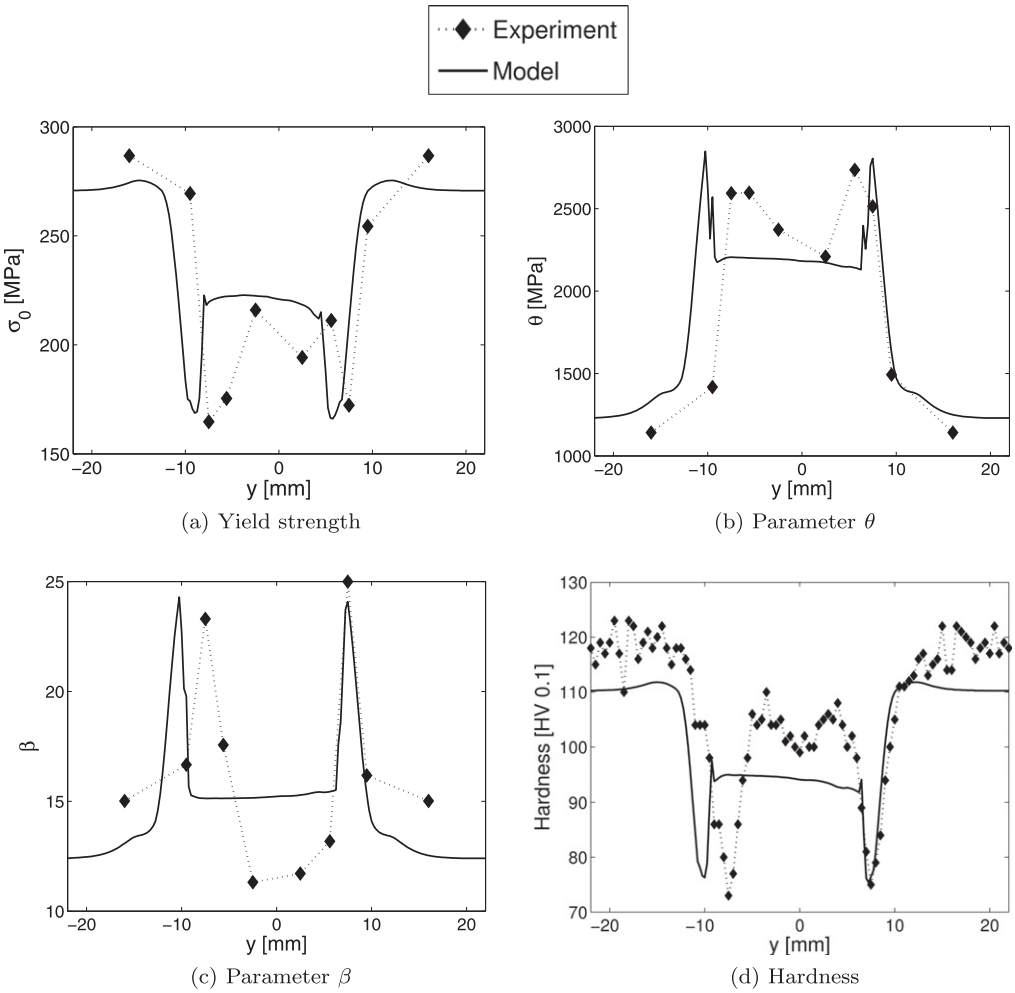

(a) Yield strength (b) Parameter θ

(c) Parameter β (d) Hardness

Fig. 25. Comparison for the 6056-T78 welds of the predicted hardness and tensile properties with the hardness measured by a Vickers micro-hardness indenter using a 0.1 kg load [54] and the measured tensile properties obtained by extracting micro-tensile specimens as a function of the position in the weld [34]; the rotational speed is equal to 1100 rpm and the advancing speed is equal to 1100 mm/min; σ_0 is the initial yield strength, θ and β are the strain hardening parameters.

4.2.3. Validation of the microstructure evolution model

Fig. 23a compares the equivalent precipitate radius predicted by the microstructure evolution model to TEM image analysis for the 6005A weld from Simar et al. [245] along the mid-thickness section transverse to the weldline. The model captures the increase of the equivalent radius in the heat affected zone when the welding speed increases. Fig. 23b compares the predictions of the microstructure evolution model extended to heterogeneous precipitation with the estimated volume fraction of precipitates obtained from differential scanning calorimetry (DSC) measurements for a 6056-T78 weld by Gallais et al. [54]. The model correctly describes the homogeneous or heterogeneous (on dispersoïds) nature of the precipitation and the related evolution of volume fraction of precipitates.

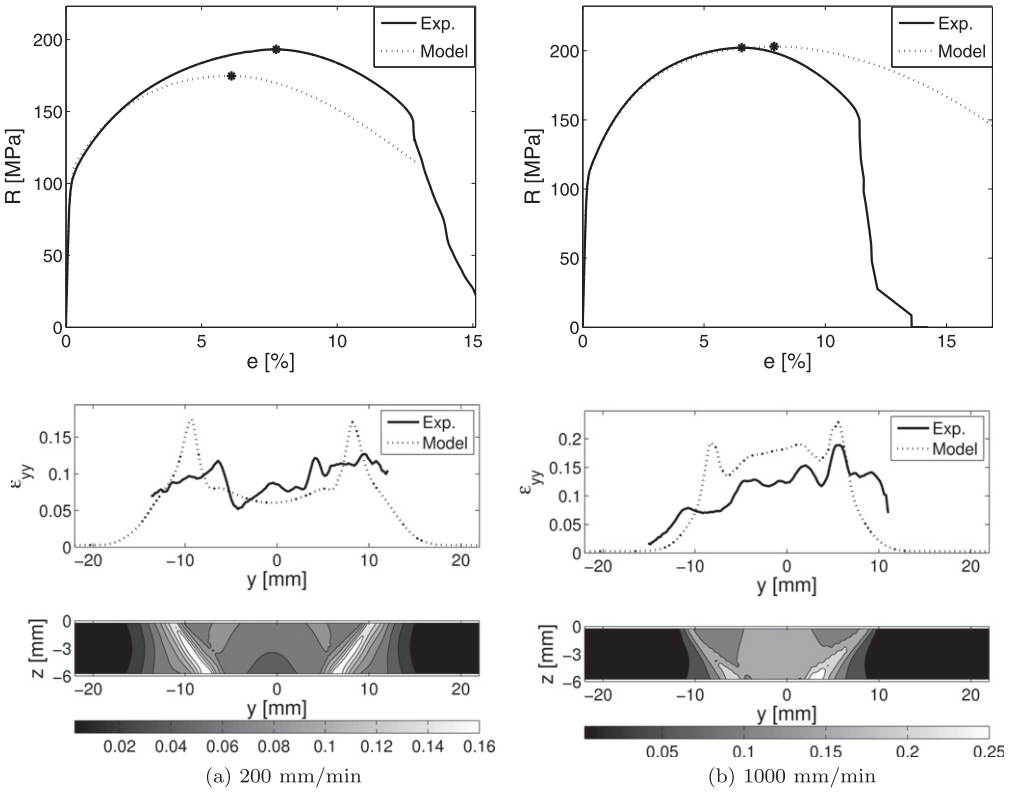

Fig. 26. Comparison of the predicted and measured transverse tensile curve (top) and local strains ϵ_{yy} in the loading direction at necking as a function of the position in a y–z plan for two 6005A-T6 welds (the two figures at bottom are the model predictions). The measurements of the local strains ϵ_{yy} are based on a digital image correlation [6,245]. The rotational speed is equal to 1000 rpm and the advancing speed is mentioned under the figures.

4.2.4. Validation of the strength and strain hardening model

Figs. 24 and 25 present the variation of the initial yield strength, hardness and strain hardening parameters as a function of the position transverse to the weldline for, respectively, two 6005A-T6 welds and one 6056-T78 weld. All the trends of the experimental results are properly captured. In the 6005A-T6 welds, a larger strain hardening capacity is observed in the weld nugget compared to the HAZ while the initial yield strength of these two zones is similar. Conversely, the initial yield strength of the HAZ in the 6056-T78, see Fig. 25, is much lower than the yield strength of the weld nugget. This is due to the heterogeneous precipitation on dispersoïds in this zone in the 6056 welds compared to a solid solution hardened by GP zones in the 6005A welds. The distribution of the strain hardening parameters in the 6056-T78 welds is similar to the distribution in the 6005A-T6 welds.

Fig. 24 shows that the increasing width of the HAZ in terms of hardness variation with decreasing advancing speed is well reproduced by the model. The cold 6005A-T6 weld (1000 mm/min) presents lower values of the parameters θ and β in the HAZ compared to the hot weld (200 mm/min). At the opposite, the yield strength of the HAZ is not much affected by the advancing speed.

4.2.5. Validation of the finite element modeling of the tensile test on welded samples

Different parameters can be extracted from an uniaxial tensile test performed on a welded sample with the loading direction perpendicular to the welding direction in order to assess its quality: a pseudo yield strength (calculated conventionally with a 0.2% offset to the linear response), a pseudo

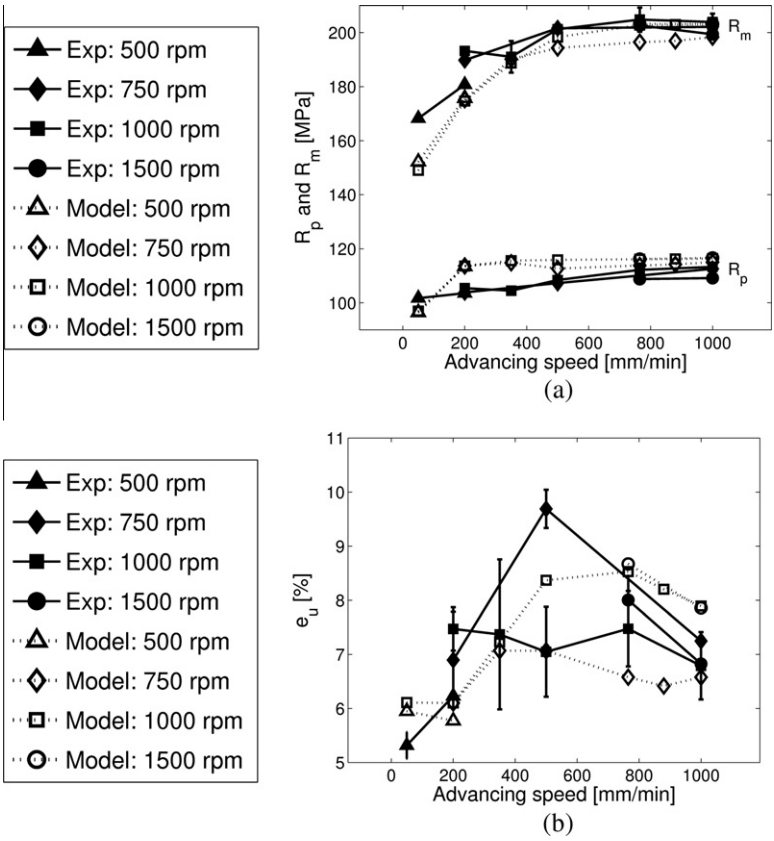

Fig. 27. Comparison of the predicted and measured transverse tensile properties for the 6005A-T6 welds as a function of the advancing speed and the rotational speed of the welds. (a) Pseudo yield strength R_p and ultimate tensile strength R_m and (b) pseudo uniform elongation e_u.

ultimate tensile strength (maximum load divided by initial specimen cross-section area) and a pseudo uniform elongation (elongation at maximum load). These quantities are "pseudo engineering" properties since the material tested is not homogeneous. The weakest zone of the weld starts yielding plastically first. When further deforming the specimen, most of the zones affected by welding also deform. The pseudo uniform elongation is highly dependent on the size of the deforming zones and on the strain hardening capacity. It is inversely proportional to the selected gage length. In our case, the gage length will be kept unchanged for all welds and equal to 50 mm.

Fig. 26 presents the predictions of the finite element simulations of the transverse uniaxial tensile test on welded 6005A-T6 samples. The pseudo yield strength and pseudo ultimate tensile strength are generally accurately predicted. The pseudo uniform elongation is more difficult to capture because it is very sensitive to the size of the weak zone and to the existence of imperfections (material and geometry). Nevertheless, the results are satisfactory to within 20–25% of error. Fig. 26 also presents the local strain field component ϵ_{yy}, compared to the predictions with digital image correlation results. The quality of the predictions confirm the ability of the model to reproduce the complex strain distribution typical of tensile tests transverse to the welds. The localization of deformation in the weak heat affected zone shows up very clearly in Fig. 26.

Fig. 27 compares the measured and predicted mechanical pseudo properties as a function of the advancing speed for various rotational speeds in 6005A-T6 welds. The predictions of the pseudo yield

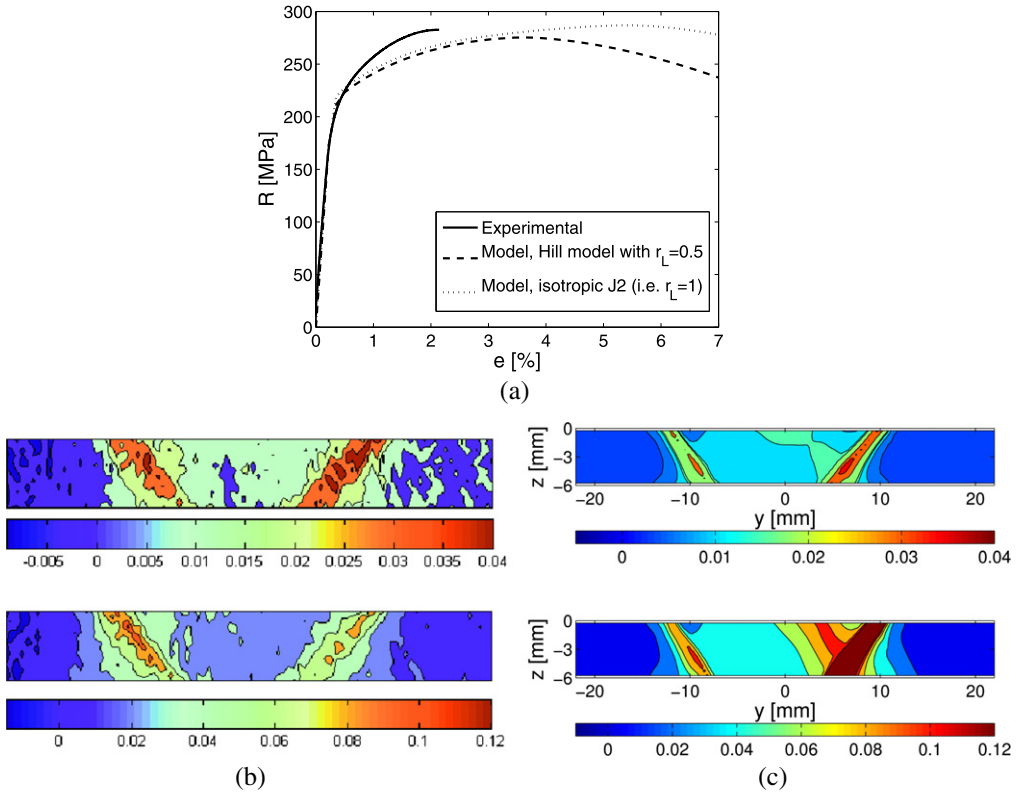

Fig. 28. (a) Comparison of the predicted and measured transverse tensile curve for a 6056-T78 weld with a rotational speed equal to 1100 rpm and an advancing speed equal to 1100 mm/min; r_L is the Lankford coefficient, $r_L = 1$ corresponds to an isotropic case. (b and c) Comparison of the predicted (with $r_L = 0.5$), on the right, and measured (DIC results), on the left, local strain in the loading direction ϵ_{yy}. On top, the map for $e/e_u = 0.2$ and, on the bottom, the map for $e/e_u = 1$; where e is the current engineering strain and e_u is the pseudo uniform elongation.

strength, ultimate tensile strength and uniform elongation are in good agreement with the experiments, validating the model chain for a wide variety of conditions. The effect of the welding parameters towards process optimization will be further discussed in Section 5.1.1.

Fig. 28a compares the predicted and experimental transverse tensile curves for a weld made of the 6056-T78 Al alloy. The predicted response significantly overestimates the pseudo uniform elongation. One of the reasons for this overestimation is plastic anisotropy. Indeed the 6056-T78 base material has been rolled giving an estimated Lankford coefficient[8] r_L equal to 0.5. Note that the anisotropy of the 6005A-T6 extruded base material is negligible. This estimate of the Lankford coefficient is based on the reduction of section in the thickness and width of base material tensile specimens. Another simulation, see Fig. 28a, was run with the anisotropic Hill model [248] for transverse isotropy and for $r_L = 0.5$. Fig. 28a shows that anisotropy affects the pseudo uniform elongation by reducing it. But, even if anisotropy is accounted for, the pseudo uniform elongation is still overestimated. This conclusion is systematic for all welds for which experiments were available (see Fig. 29b). The reason for this discrepancy is difficult to determine but could result either from a poor estimation of the strain hardening ability at high

[8] The Lankford coefficient is the ratio of the plastic strain in the rolling plan divided by the plastic strain in the thickness direction.

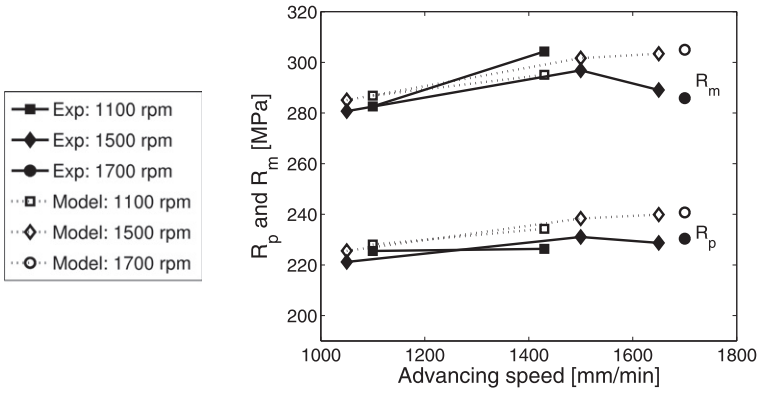

(a) Pseudo yield strength R_p and ultimate tensile strength R_m.

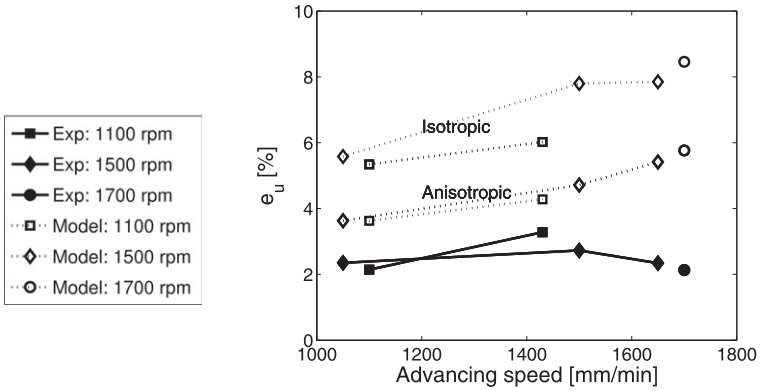

(b) Pseudo uniform elongation e_u, isotropic or anisotropic case ($r_L = 0.5$).

Fig. 29. Comparison of the predicted and measured transverse tensile properties for the 6056-T78 welds as a function of the advancing speed and the rotational speed of the welds.

strains (e.g. stage IV hardening), from the presence of imperfections in the tensile samples or from an inaccurate prediction of the geometry of the weak zone. Cracking in the 6056-T78 welds produced with welding parameters equal to 1700 mm/min and 1700 rpm takes place inside the weld nugget. This might be explained by the presence of a small root defect which is also the cause for the lower strength and ductility measured for that weld compared to the model. The apparent strain hardening capacity of the weld is underestimated but this may have the same origin as the overestimation of the pseudo uniform elongation. Note that, in the results presented next in this study, anisotropy will not be accounted for except if explicitly mentioned. Indeed, the damage model is only developed and validated for plastic isotropy.

Fig. 25a shows that the yield strength of the weakest zone of the 6056 weld is about 170 MPa while the plasticity spreads throughout the weld at about 215 MPa, see Fig. 28a. This is due to the narrow band of weak material that has already reached yielding with an applied stress between 170 and 215 MPa. This is not observed in a 6005A weld where the weld nugget has a yield strength similar to the weak heat affected zone (see Fig. 24a) and macroscopic evidence of plastic deformation in the weld appears at a level only slightly larger compared to the weakest zone of the weld (see Fig. 26). The precipitation of the Q phase on dispersoïds in the 6056-T78 weld nugget decreases the difference in pseudo yield strength of a weld compared to the yield strength of the base material in 6056-T78 welds. Indeed, the pseudo yield strength of the 6005A-T6 weld of Fig. 26b is about 40% of

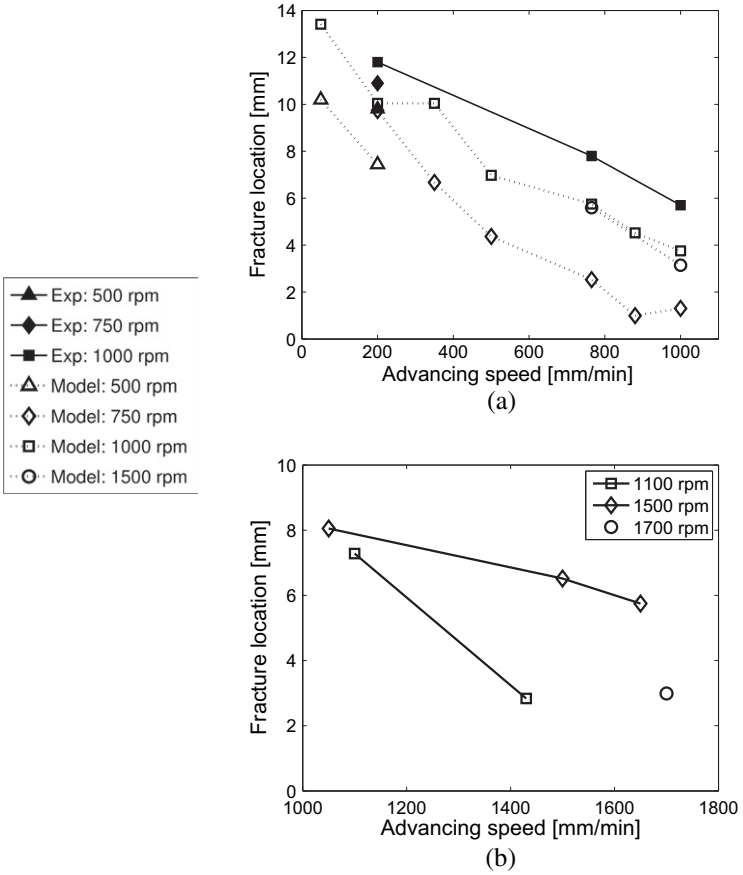

Fig. 30. Location of fracture at mid-thickness (distance from the weld centerline) for (a) 6005A-T6 welds (absolute value) and (b) 6056-T78 welds. (a) Comparison with experimental locations of fracture obtained by marking the samples before tensile testing.

the yield strength of the base material while for the 6056-T78 weld of Fig. 28a, this ratio goes up to 80%.

Fig. 28b and c present respectively the measured (by digital image correlation) and predicted local strain component in the loading direction ϵ_{yy} for the 6056-T78 weld with an advancing speed equal to 1100 mm/min and a rotational speed equal to 1100 rpm. The model captures the localization of deformation in an inclined band very early in the tensile test, i.e. already when $e/e_u = 0.2$, well before reaching the maximum load.

Fig. 29 presents the measured and predicted results of the transverse uniaxial tensile tests as a function of the advancing speed for various rotational speeds in the 6056-T78 welds. The model correctly predicts the pseudo yield strength and the pseudo ultimate tensile strength. The model systematically overestimates the pseudo uniform elongation as shown in Fig. 28a but all trends are properly captured.

Fig. 30 compares the fracture location predicted by the finite element model. Note that Fig. 30 only gives the distance to the weld center because fracture can sometimes occur either on the advancing side of the weld or on the retreating side.

The location of fracture was determined by drawing vertical marker lines equally spaced before tensile testing on a few 6005A-T6 weld samples. The model slightly overestimates the fracture

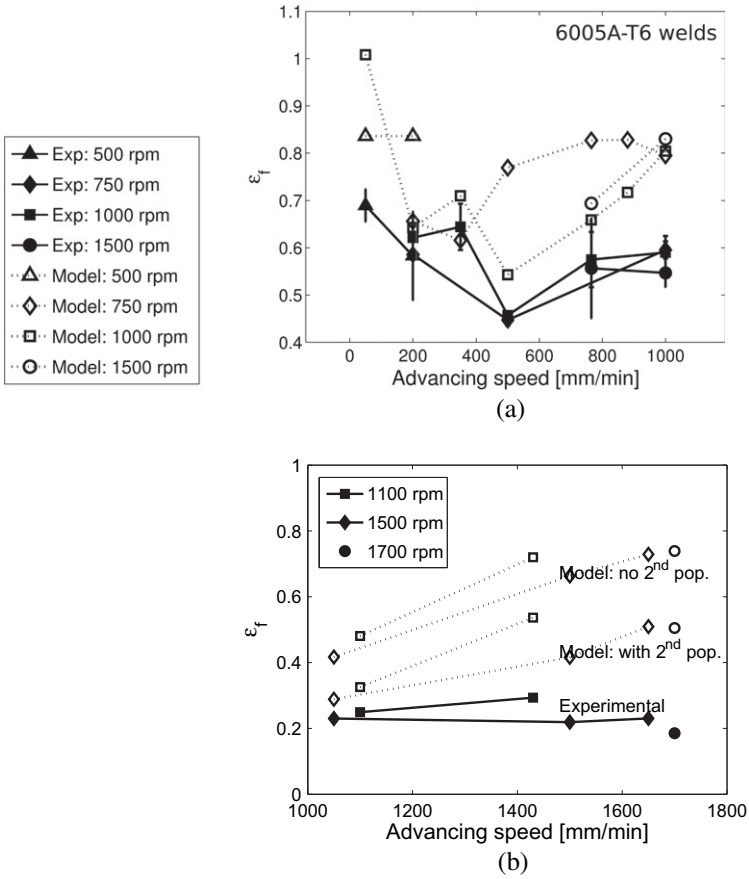

Fig. 31. Comparison of the predicted and measured fracture strain for various welding parameters for (a) the 6005A-T6 and (b) 6056-T78 welds. The predictions of the model are given with and without accounting for a second population of cavities for the 6056-T78 welds (no second population is observed in the 6005A-T6 welds).

position but captures the observed fracture closer to the weldline if the advancing speed increases and if the rotational speed decreases. The fracture position corresponds to the weak heat affected zone slightly towards the base material except for the very cold welds where fracture occurs closer to the weld center as can be observed on Fig. 30a. This is due to the limited difference in yield strength between the heat affected zone and the weld nugget. The 6005A welds experimentally tend to fracture on the retreating side except for some moderately hot welds (with advancing speed lower than 350 mm/min but larger than about 200 mm/min) where fracture occurs on either side of the welds. The model predicts fracture on the retreating side for cold welds and usually predicts fracture on the advancing side of the weld for moderately hot welds. Nevertheless, the welding condition at which the transition of fracture side occurs experimentally is not systematically well predicted. Welds tend to be more symmetric in terms of mechanical properties as the advancing speed decreases due to the lower difference in temperature between the advancing and retreating side as shown in Fig. 22. This justifies the tendency for plastic localization and finally cracking to occur on the advancing side when the advancing speed decreases. The model overestimates the asymmetry in the temperature evolution. This inaccuracy at that early stage of the model chain has an impact at the end of the model chain when looking at the location of fracture.

The 6056-T78 welds with a rotational speed equal to 1100 rpm experimentally fracture on the advancing side of the weld while the 6056-T78 welds with a rotational speed equal to 1500 rpm break

on the retreating side of the weld. The model systematically predicts that fracture occurs on the retreating side of the weld. The model predicts the same trend as for the 6005A welds, i.e. fracture occurring closer to the weldline if the advancing speed increases and the rotational speed decreases. The fracture location corresponds to the limit between the thermo-mechanically affected zone and the heat affected zone in agreement with the experimental observations [34].

4.2.6. Validation of the damage model

The predictions of the damage model have been assessed only in terms of the experimental fracture strain ε_f. Fig. 31 compares the predicted and the measured fracture strains for various welding parameters for the 6005A-T6 and 6056-T78 welds (note that plastic anisotropy is not accounted for). The predicted fracture strain agrees with the experimental values with a systematic but moderate overestimation. The experimental observation that the fracture strain goes through a minimum for an intermediate advancing speed (around 500 mm/min) in the 6005A welds (see Fig. 31a) is properly captured. The tendency for an increase of the fracture strain in the 6056-T78 welds when increasing the advancing speed is correctly reproduced, though slightly overestimated (see Fig. 31b). The fracture strain increases when the rotational speed decreases. As also mentioned in Section 3.4.4 and shown on the fracture surfaces of the two alloys in Fig. 14, no second population of cavities nucleate in the 6005A welds while they significantly reduce the fracture strain of 6056-T78 welds (see Fig. 31b). The introduction of a second population of cavities in the model significantly improves the fracture strain predictions in the 6056-T78 welds.

It is interesting to compare the local strains at void nucleation for the two alloys. For the 6056-T78 welds void nucleation occurs almost at the onset of plasticity while, in the 6005A weld, void nucleation occurs when the equivalent local plastic strain is becoming at least larger than 0.2 with a value depending on the welding parameters. This significant difference in the local strain at void nucleation is due to the lower stress level reached in the 6005A weld. This, in addition to the effect of the second population of cavities, explains the much lower fracture strain of the 6056-T78 welds compared to the 6005A-T6 welds.

5. Process optimization

This section aims at discussing the effect of the welding parameters and base material parameters on the end use properties of the joints with the intent to optimize the process. The focus will be on the strength and ductility optimization though the approach could be extended to other properties (e.g. the fracture toughness). Since it has been shown in Section 4.2 that the ''chain model'' based on physical laws reproduces with reasonable accuracy the experimentally measured joint properties, it can thus be used to predict trends for other compositions and process parameters, some of them being outside the experimental window investigated up to now, but within the range of validity of the underlying physical parameters. Nevertheless, one must recognize cumulative uncertainties associated to the chaining of several models having each their adjustable parameters. Further work should involve the estimation of this error by varying the adjustable parameters, testing the sensitivity on the predictions of the ''chain model'' and compare with the effects predicted in the present section.

Two main reference welds in the 6005A-T6 alloy are selected as a basis for comparison of various optimization routes. Both welds have been obtained with a rotational speed equal to 1000 rpm. The ''hot'' weld (referred to as ''weld A'') has been obtained with an advancing speed equal to 50 mm/min and the ''cold'' weld (referred to as ''weld B'') has an advancing speed equal to 1000 mm/min. One reference weld in the 6056-T78 alloy is also selected for comparison with various optimization routes. This weld, referred to as ''weld C'', was produced using an advancing speed equal to 1100 mm/min and a rotational speed equal to 1100 rpm. The dimensions of the simulated joints are identical to the experimental dimensions (see end of Section 3.1.2.6).

Firstly, the effects of the welding parameters on the weld performances will be assessed by studying the effects of the advancing speed, the rotational speed, the initial temperature of the workpiece, the cooling conditions after the tool has left and the material of the backing plate. Secondly, the effect of the alloy composition, both in terms of strengthening constituents and in terms of iron content

Table 10
Predicted precipitate mean radius at mid-thickness (r), predicted volume fraction of precipitates at mid-thickness (f_v), predicted width of the joint (W defined from the region where the yield strength drops down at 3/4 of the yield strength HAZ) and predicted local tensile properties in the weakest zone at mid-thickness (σ_0, θ and β) used for the optimization analysis. Weld **A**: 50 mm/min and 1000 rpm, weld **B**: 1000 mm/min and 1000 rpm and weld **C**: 1100 mm/min and 1100 rpm. SS = strainless steel, CS = carbon steel and PWHT = post-welding heat treatment. Note that, for the 6005A welds, r is the maximum in the HAZ and, for the 6056 welds, two radii are given: first the maximum homogeneous precipitate radius (except for the T4 weld where it is the mean radius of precipitates that nucleate on dislocations in the HAZ) and second the mean radius of precipitates that nucleate on dispersoïds at the joint line. Regarding f_v, for the 6005A welds, it is the value at the yield strength minimum and, for the 6056 welds, two values for f_v are given: first the value at the minimum of yield strength and second the volume fraction of precipitates that nucleate on dispersoïds at the joint line. Regarding σ_0, two values are given for the 6056-T78 welds: first the minimum yield strength in the weakest zone of the weld and second the yield strength at the joint line. The strain hardening parameters θ max and β max belong to the weakest zone of the weld.

Location	r (nm) HAZ	f_v (%) min σ_0	W (mm)	σ_0 (MPa) min – WN	θ max (MPa) HAZ	β max HAZ
Model conditions for 6005A-T6 welds						
50 mm/min and 1000 rpm (**A**)	14.0	0.46	40.8	70 – 93	2744	37
1000 mm/min and 1000 rpm (**B**)	4.3	0.05	19.3	79 – 108	1873	17
weld B, T_{in} = 150 °C	4.3	0.05	28.3	84 – 113	1843	18
weld A, CC_B = 0 kW/m^2 K	14.7	0.49	41.1	68 – 106	2779	38
weld A, CC_B = 30 kW/m^2 K	13.5	0.46	40.5	71 – 96	2718	36
weld B, CC_B = 0 kW/m^2 K	4.2	0.05	19.5	80 – 110	1860	17
weld B, CC_B = 30 kW/m^2 K	4.3	0.05	19.1	79 – 107	1887	17
weld B, Cu backing plate	3.9	0.15	12.7	130 – 158	1773	15
weld B, SS backing plate	4.4	0.06	21.2	81 – 109	1876	18
weld B, 0.58 wt.% Mg	7.5	0.21	19.1	94 – 108	2427	25
weld B, state T4	2.4	0.04	30	98 – 108	1863	13
weld B, state T4 + 2 h at 180 °C	2.9	0.05	20.8	98 – 109	1863	13
weld A, T6 PWHT	7.9	0.65	44.0	118 – 244	2355	33
weld B, T6 PWHT	3.9	0.70	19.6	213 – 246	1235	16
weld B, state T4 + T6 PWHT	3.0	0.69	30	244 – 246	714	8
Location	HAZ – WN	min σ_0 – WN				
Model conditions for 6056-T78 welds						
1100 mm/min and 1100 rpm (**C**)	16.9 – 15.7	1.70 – 0.63	20.8	166 – 222	2848	24
1430 mm/min and 1100 rpm	13.1 – 15.3	1.62 – 0.59	17.5	180 – 224	2812	24
weld C, T_{in} = 150 °C	21.8 – 19.1	1.77 – 1.12	25.2	131 – 192	2914	25
weld C, CC_B = 0 kW/m^2 K	18.3 – 18.0	1.77 – 0.95	20.8	147 – 204	2887	25
weld C, CC_B = 50 kW/m^2 K	15.2 – 13.9	1.65 – 0.44	20.8	180 – 231	2860	24
weld C, Cu backing plate	8.5 – 6.9	1.66 – 1.73	16.2	188 – 203	2784	24
weld C, CS backing plate	16.5 – 15.2	1.65 – 0.57	19.8	171 – 225	2853	24
weld C, 20% more alloying element	55.0 – 18.3	2.09 – 1.08	20.5	161 – 220	3063	26
weld C, state T4	13.5 – 15.7	1.77 – 0.63	21.5	160 – 222	2876	25

(responsible for the brittle intermetallic phase), as well as the effect of the alloy initial precipitation state will be investigated. Finally, the effect of a T6 type post-welding heat treatment on the microstructure and tensile properties of the weld will be tested. Note that some results already presented earlier in the paper will be used again in this section.

Table 10 summarizes the results discussed in this section in terms of the most relevant resulting characteristics, at the "local" level, i.e. the width of the joint, the precipitate radius and the tensile properties of the weakest zone and weld nugget, while Table 11 summarizes the results at the "macroscopic" level, in terms of transverse tensile properties of the welds. The results in Tables 10 and 11 are analyzed in details in the next sub-sections.

5.1. Optimization of the welding parameters

5.1.1. Effects of the advancing and rotational speeds

Fig. 27 compares the measured and predicted transverse tensile properties of the 6005A-T6 welds as a function of the advancing velocity for various rotational speeds. When the advancing velocity

Table 11
Predicted transverse tensile properties from the optimization analysis: R_p is the pseudo yield strength of the weld, R_m is the pseudo ultimate tensile strength of the weld, e_u is the pseudo uniform elongation and ε_f is the fracture strain. The fracture strain ε_f is predicted without (ε_{f1}) or with (ε_{f2}) accounting for the nucleation of a second population of cavities. Transverse tensile property improvements by more than 5% compared to the reference welds A, B or C are underlined. The 6056-T78 weld simulation were performed without including the effect of anisotropy. Weld **A**: 50 mm/min and 1000 rpm, weld **B**: 1000 mm/min and 1000 rpm and weld **C**: 1100 mm/min and 1100 rpm. SS = strainless steel, CS = carbon steel, ua = unaffected, BM = base material and PWHT = post-welding heat treatment.

	R_p (MPa)	R_m (MPa)	e_u (%)	ε_{f1}	ε_{f2}
Model conditions for 6005A-T6 welds					
50 mm/min and 1000 rpm (**A**)	97	149	6.1	1.01	ua
1000 mm/min and 1000 rpm (**B**)	116	203	7.9	0.80	ua
weld B, T_{in} = 150 °C	119	204	9.6	0.71	ua
weld A, CC_B = 0 kW/m^2 K	101	147	5.3	1.06	ua
weld A, CC_B = 30 kW/m^2 K	96	151	6.4	0.98	ua
weld B, CC_B = 0 kW/m^2 K	117	204	8.0	0.77	0.76
weld B, CC_B = 30 kW/m^2 K	116	202	7.9	0.79	ua
weld B, Cu backing plate	172	226	5.1	0.73	ua
weld B, SS backing plate	117	205	8.5	0.63	ua
weld B, 0.58 wt.% Mg	120	197	6.1	0.67	0.66
weld A, 20% reduction of f_p (wt.%Fe)	ua	ua	ua	1.02	ua
weld B, 20% reduction of f_p (wt.%Fe)	ua	ua	ua	0.87	0.83
weld A, 20% increase of f_p (wt.%Fe)	ua	ua	ua	1.00	ua
weld B, 20% increase of f_p (wt.%Fe)	ua	ua	ua	0.74	ua
weld B, state T4	105	192	Fracture in BM	Fracture in BM	
weld B, state T4 + 2 h at 180 °C	119	208	8.7	0.89	0.86
weld A, T6 PWHT	154	192	3.2	0.73	ua
weld B, T6 PWHT	242	264	8.4	0.57	0.55
weld B, state T4 + T6 PWHT	246	266	Fracture in BM	Fracture in BM	
Model conditions for 6056-T78 welds					
1100 mm/min and 1100 rpm (**C**)	226	287	5.8	0.48	0.33
1430 mm/min and 1100 rpm	232	295	6.5	0.72	0.54
weld C, T_{in} = 150 °C	192	251	5.4	0.43	0.38
weld C, CC_B = 0 kW/m^2 K	209	274	5.9	0.77	0.53
weld C, CC_B = 50 kW/m^2 K	236	302	8.0	0.56	0.46
weld C, Cu backing plate	236	296	7.0	0.76	0.63
weld C, CS backing plate	226	294	7.1	0.68	0.46
weld C, 20% more alloying element	215	282	5.4	0.76	0.57
weld C, 20% reduction of f_p (wt.%Fe)	ua	ua	ua	0.51	0.34
weld C, 20% increase of f_p (wt.%Fe)	ua	ua	ua	0.46	0.31
weld C, state T4	221	285	6.5	0.45	0.38

increases, the strength of the weld increases, reaching a plateau when the advancing speed becomes larger than 500 mm/min. The model predicts this change with a slight overestimation. The pseudo uniform elongation is generally higher at moderate to high advancing speeds. The two extreme advancing speeds give lower pseudo uniform elongation compared to intermediate advancing speeds around 500 mm/min. Those predicted trends are confirmed experimentally. There is no significant effect of the rotational speed.

Fig. 29 presents the measured and predicted transverse tensile properties of the 6056-T78 welds as a function of the advancing velocity for various rotational speeds. Again, there is no significant effect of the rotational speed. The dependence of the strength on the advancing speed is much weaker than for the 6005A-T6 welds, with a tendency for an increase with increasing advancing speed. The pseudo uniform elongation slightly increases with increasing advancing speed, especially for low rotational speed welds. At the highest rotational speed (1700 mm/min), the experimental pseudo uniform elongation is particularly small but this is due to the opening of a root defect (which cannot be predicted by the model) causing fracture in the weld nugget while the model predicts fracture in the thermomechanically affected zone.

Fig. 31 presents the measured and predicted fracture strains as a function of the advancing speed under various rotational speeds for (a) the 6005A-T6 and (b) the 6056-T78 welds. At very high advancing speeds (larger than 600 mm/min) the fracture strain increases with increasing advancing speed while the level of strength saturates at intermediate advancing speeds. At advancing speeds lower than 400 mm/min, the fracture strain decreases with increasing advancing speed. The model correctly predicts this interesting trend which deserves more attention.

Fig. 19b shows that for the 6005A-T6 welds with an advancing speed of 50 mm/min, the predicted maximum temperature close to the weld center is 130 °C larger than for the 1000 mm/min weld. Consequently, Table 10 shows that the precipitate radius in the heat affected zone increases by a factor of 3 (see also Fig. 23a). Furthermore, the volume fraction of precipitates is almost equal to the maximum Mg concentration, thereby limiting the possibility for post-welding natural aging. The larger precipitate radius and the lower natural aging capacity explains the drop in strength when reducing the advancing speed (see Table 11). Looking at the strain hardening evolution, the high apparent strain hardening rate θ is compensated by a very high effective recovery rate β in the HAZ of the welds. The width of the heat affected zone is significantly increased when lowering the advancing speed. Hence, deformation localizes in a larger zone, and the local stress triaxiality gets smaller (see Fig. 31a). This explains the large fracture strains predicted for welds obtained under very low advancing speeds. The larger fracture strain of welds generated with a high advancing speed is explained by the lower strength mismatch between the weak zone and the weld nugget which reduces also the stress triaxiality level. For the 6056-T78 welds, the increase in advancing speed from 1100 mm/min to 1430 mm/min (see Table 10) is probably too small to significantly enhance the strength as confirmed by the small measured temperature difference (see Fig. 20a). Although overestimated by the model (see Fig. 31b), the larger fracture strain when increasing the advancing speed is also due to the lower strength mismatch between the weak zone and the weld nugget, as for the 6005A welds.

As a conclusion, the strength of a weld is improved by using the fastest advancing speed and, the lowest possible rotational speed though the last effect is of second order. Ductility is another important property regarding possible post welding forming operation. If the aim is to improve the ductility of a weld (measured by the pseudo uniform elongation), an intermediate welding speed (500 mm/min) gives the best results for the 6005A welds while no clear improvement associated to the welding parameters are found for the 6056-T78 welds. If the aim is to improve the resistance to damage of a weld, as quantified here by the fracture strain, intermediate advancing speeds must be avoided. The key for understanding this last conclusion is very much related to the size of the weak zone. If the weak zone is narrow, stress triaxiality becomes high because of intense plastic localization. This is exactly the issue encountered in many other applications involving soft bands squeezed between hard layers, e.g. in precipitate free zones [10]. Hence, the largest advancing speeds, as long as the weld is sound, are the welding conditions giving the best compromise between strength, ductility and damage resistance. This conclusion, going in line with an increasing productivity, is well known by the practitioners.

5.1.2. Effects of the preheating

Figs. 32 and 33 present the predicted temperature cycles and the resulting local yield strength distributions when preheating the workpiece at a temperature equal to 150 °C for the 6005A and 6056 welds. Fig. 33 also provides the mean precipitate radius and volume fraction distribution at mid-thickness. The corresponding microstructural, local tensile properties and transverse tensile properties are given in Tables 10 and 11. In these simulations, the torque has been adjusted such as to keep the overall maximum temperature unchanged, since it is close to the melting temperature of the alloys. In the absence of any other experimental data, it was considered as the best assumption to be made. The torque depends on the rheology of the material which is in turn affected by the temperature. More sophisticated thermal models and/or experiments are thus required to validate the conclusions of this section. Nevertheless, the hypothesis of a constant maximum temperature is reasonable, avoiding too large maximum temperature incompatible with a solid state process.

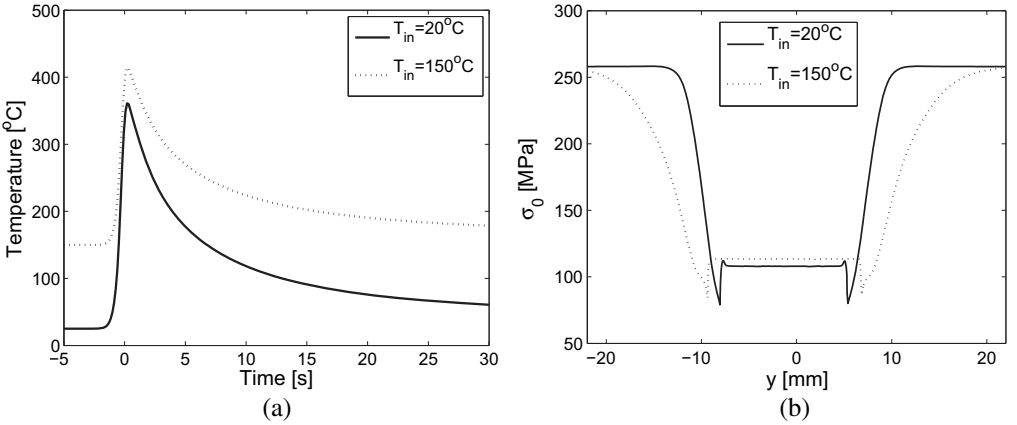

Fig. 32. Effect of an initial preheating temperature equal to 150 °C on the predictions of the model chain for the 6005A alloy. The rotational speed is equal to 1000 rpm and the advancing speed is equal to 1000 mm/min (weld B). (a) Temperature cycles at 10 mm from the weld center on the advancing side and at mid-thickness of the weld and (b) local yield strength profile.

Regarding the 6005A welds, the heat affected zone becomes wider with increasing initial temperature (see Fig. 32b and Table 10) while the precipitate radius and volume fraction are not modified. Hence, the strength of the weakest zone is almost unaffected by the initial temperature (see Table 10). The transverse tensile strength does not change either (see Table 11). However, due to a 50% increase in the width of the heat affected zone, the pseudo uniform elongation increases by 20% (see Table 11). Regarding fracture, Fig. 32b shows that the weak zone contains an even weaker very narrow band where deformation localizes at large strains. This causes a high level of stress triaxiality in the element reaching void coalescence first, and a decrease of the fracture strain ε_f by 10% to 0.71 instead of 0.80.

Concerning the 6056 welds, Fig. 33a shows that, on the one hand, the maximum temperature 10 mm away from the weldline increases only slightly by setting the initial workpiece temperature

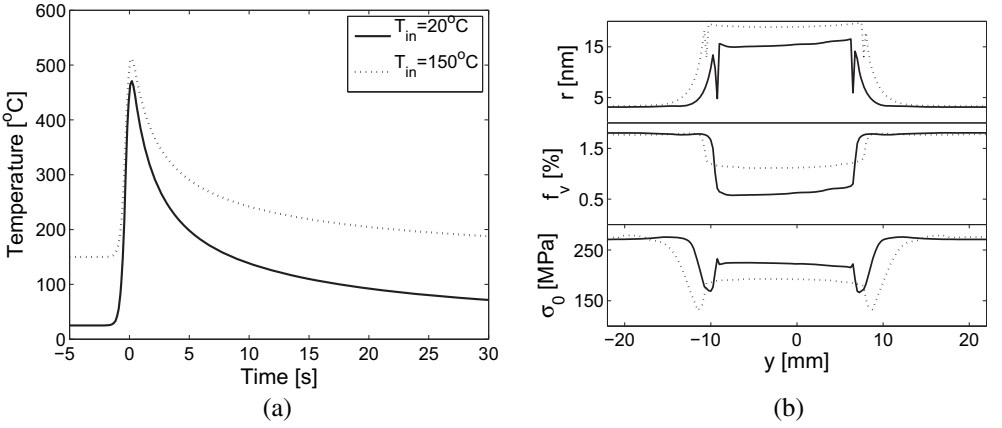

Fig. 33. Effect of an initial preheating temperature equal to 150 °C on the predictions of the model chain for the 6056 alloy. The rotational speed is equal to 1100 rpm and the advancing speed is equal to 1100 mm/min (weld C). (a) Temperature cycles 10 mm away from the weld centerline on the advancing side and at mid-thickness of the weld; (b) the mean precipitate radius r (i.e. the contribution of the radius of each type of precipitate multiplied by its volume fraction are added and the total is divided by f_v), the total precipitate volume fraction f_v and the local yield strength σ_0.

equal to 150 °C, and, on the other hand, the cooling rate is much slower. Hence, the precipitate radius in the weak zone and in the weld nugget increases by more than 20% to 19.1 nm instead of 15.7 nm (see Fig. 33b and Table 10) compared to the reference condition. The volume fraction of precipitates nucleated on dispersoïds increases by 80% in the weld nugget to 1.12% instead of 0.63% (see Fig. 33b and Table 10). The consequence is a 20% decrease of the initial yield strength in the weak zone and a 13% decrease in the weld nugget (see Fig. 33b and Table 10). Indeed, a larger precipitate radius leads to lower strength while a larger precipitate volume fraction causes a lower solid solution concentration and hence a lower contribution of the strength associated to the precipitation of GP zones by natural aging. The lower strength of the various regions of the weld causes a decrease of the transverse tensile strength of the weld, R_p and R_m, by respectively 15% and 13% compared to the reference weld C. The pseudo uniform elongation is only slightly improved. Contrarily to the 6005A-T6 welds, the predicted fracture strain increases by 15% due to the lower strength level, favoring a later nucleation of the second population of voids.

The results presented in this section show that the effect of the initial temperature depends on the alloy composition. In low alloyed Al, like the 6005A alloy, changing the initial temperature causes only a minor improvement of the pseudo uniform elongation while being detrimental to the fracture strain. Hence, increasing the initial temperature might be recommended for alloys of that family only in applications for which a large resistance to plastic localization is required such as in the case of a post welding forming operation. In highly charged alloys, like the 6056 alloy, the increase of the initial temperature causes an increase of the precipitate radius and volume fraction. Consequently, the strength decreases with no marked improvement of the pseudo uniform elongation but an increase of the fracture strain. Hence, increasing the initial temperature is not to be recommended for such alloys except for improving the damage tolerance.

5.1.3. Effects of the cooling rate

Figs. 34 and 35a present the predicted temperature cycles during welding when adjusting the cooling rate either by increasing by a factor of 10 or by setting to zero the parameter CC_B describing the contact conductance between the workpiece and the backing plate behind the tool (see Fig. 8). The torque is assumed unchanged compared to the reference weld since the overall maximum temperatures is unaffected by the variation of the parameter CC_B contrarily to the effect of preheating the plates (Section 5.1.2). For the 6005A-T6 welds, the two extreme advancing speeds, i.e. 50 mm/min and 1000 mm/min, are studied with the rotational speed kept constant at 1000 mm/min. For the 6056-T78 welds, only weld C, with an advancing speed equal to 1100 mm/min and a rotational speed

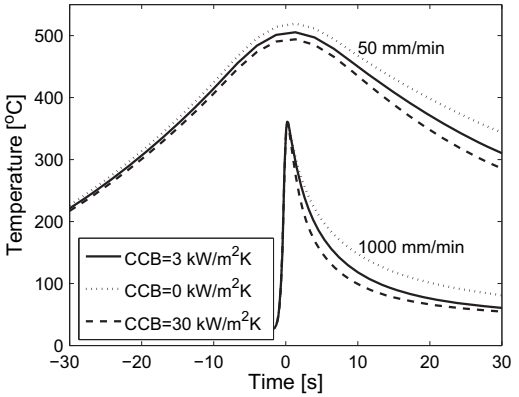

Fig. 34. Effect of the cooling rate parameter CC_B on the predicted thermal cycle at mid-thickness, 10 mm away from the weldline on the advancing side, for two 6005A welds with a rotational speed equal to 1000 mm/min and two advancing speeds equal to 50 mm/min (weld A) and 1000 mm/min (weld B).

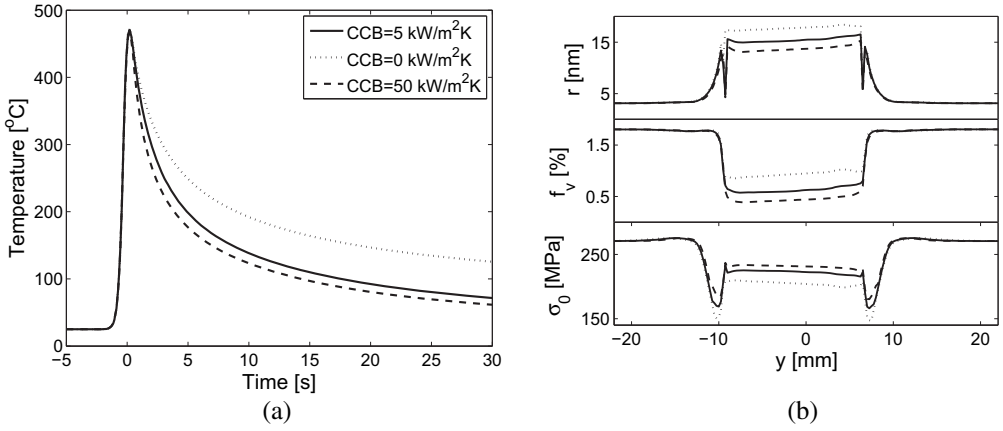

(a) (b)

Fig. 35. Effect of the cooling rate parameter CC_B on the predictions of the model chain for the 6056 alloy. The rotational speed is equal to 1100 rpm and the advancing speed is equal to 1100 mm/min (weld C). (a) Temperature cycles at 10 mm away from the weld centerline on the advancing side and at mid-thickness of the weld, (b) the mean precipitate radius r (i.e. the contribution of the radius of each type of precipitate multiplied by its volume fraction are added and the total is divided by f_v), the total precipitate volume fraction f_v and the local yield strength σ_0.

equal to 1100 rpm is considered. The results of the model chain are presented in Tables 10 and 11 and in Fig. 35.

Regarding the 6005A-T6 welds, for a "cold" weld with advancing speed equal to 1000 mm/min, no significant effect on the minimum tensile properties in the heat affected zone is predicted. The ultimate tensile strength of the weakest point was found to change by about 2 MPa for the three considered CC_B values (see Tables 10 and 11). For the "hot" weld with an advancing speed equal to 50 mm/min, the value CC_B slightly affects the maximum temperature contrarily to the "cold" weld. As a result, the pseudo uniform elongation increases by about 5% when setting CC_B equal to 30 kW/m^2 K but the pseudo ultimate tensile strength remains almost constant (see Table 11). The fracture strain is almost not affected by the initial temperature with a slight tendency to decrease, except for the slow cooling rate (i.e. CC_B = 30 kW/m^2 K) and the slowest advancing speed (i.e. 50 mm/min), see Table 11.

Regarding the 6056-T78 weld, Table 11 shows that the effect of CC_B on the properties of the welds is more significant than for the 6005A-T6 welds: both the strength and the pseudo uniform elongation are modified. The 6056 alloy is more quench sensitive than the 6005A alloy due to the heterogeneous precipitation that occurs at high temperature in the former alloy [54,118]. When decreasing the cooling rate CC_B from 5 to 0 kW/m^2K, the precipitate radius increases by 8% to 18.3 nm instead of 16.9 nm in the weak zone and by 15% to 18 nm instead of 15.7 nm in the nugget (see Fig. 35b). This causes a decrease of the initial yield strength by 11% in the weak zone and by 8% in the nugget without significantly affecting the strain hardening capacity (see Fig. 35b and Table 10). Hence, the pseudo yield strength decreases by 8% to 209 MPa instead of 226 MPa while the pseudo uniform elongation remains unchanged (see Table 11). When increasing the cooling rate CC_B from 5 to 50 kW/m^2K, the precipitate radius decreases by 10% to 15.2 nm instead of 16.9 nm in the weak zone and by 11% to 13.9 nm instead of 15.7 nm in the weld nugget with a significant decrease (by 30%) of the precipitate volume fraction in the weld nugget (see Fig. 35b). This results in an increase of the initial yield strength in both zones and, finally, in an improvement of the weld transverse tensile properties (4% increase of the pseudo yield strength, 5% increase of the pseudo ultimate tensile strength, 38% increase of the pseudo uniform elongation and 40% increase of the fracture strain, see Table 11).

As a conclusion, the transverse tensile properties can be optimized for quench sensitive alloys like the 6056, where heterogeneous precipitation at high temperature occurs, by increasing the cooling rate. Significant improvements of the strength as well as of the ductility can be reached. A faster

cooling rate behind the tool can be obtained for instance by an external cooling operation, right after welding. In addition, Staron et al. [249] and Luan et al. [250] have shown that cooling after welding by, respectively, liquid CO_2 and water spray significantly reduces residual stresses in the weld center. Recently, Richards et al. [251] have simulated this effect of residual stress reduction due to cooling after welding.

5.1.4. Effects of the material of the backing plate

In this section, the modeling chain is applied to test the impact of the backing plate material under constant contact conditions. For the 6005A welds, the backing plate used in the experiments was made of high carbon steel; the effect of replacing this backing plate by copper or by stainless steel is simulated. For the 6056 welds, the backing plate used in the experiments was made of stainless steel; the effect of replacing this backing plate by copper or by high carbon steel is simulated. Table 12 presents the thermal properties of these various backing plate materials. The torque has been assumed unchanged for the different backing plate materials. This is indeed probably a rough assumption since a more efficient heat transfer will lead to a lower peak temperature and therefore to a higher torque which, in turn, would increase heat generation, counterbalancing the better heat extraction effect. The calculation performed here neglects this point and probably overestimates the lowering of temperatures. For instance, the overall maximum temperature in weld B is predicted equal to 619 °C with a high carbon steel backing plate while the overall maximum temperature is predicted equal to 502 °C with a copper backing plate.

Fig. 36 presents the predicted temperature cycles when modifying the material of the backing plate. As expected, the temperature decreases with increasing thermal conductivity of the backing

Table 12
Thermal properties of the various backing plates used for the modeling [98].

Material of the backing plate	Density, ρ_a (kg/m^3)	Specific heat, cp (J/kg K)	Thermal conductivity, λ (W/mK)
Stainless steel	7700	460	21
High carbon steel	7700	460	47
Copper	8900	420	381

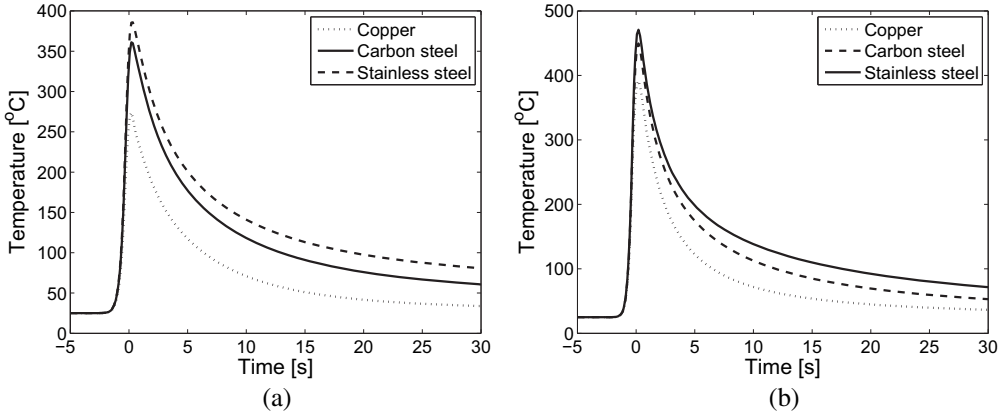

Fig. 36. Effect of the backing plate material on temperature cycles at 10 mm from the weld centerline on the advancing side of the weld and at mid-thickness for (a) a 6005A-T6 weld with an advancing speed of 1000 mm/min and a rotational speed of 1000 rpm (weld B) and (b) a 6056-T78 weld with and advancing speed of 1100 mm/min and a rotational speed of 1100 mm/min (weld C). The material of the backing plate in the experimental setup (i.e. carbon steel for the 6005A welds and stainless steel for the 6056 welds) is represented with a continuous line.

plate (see Table 12), i.e. the highest temperatures are found for the stainless steel backing plate and the lowest temperatures for the copper backing plate. Figs. 37 and 38 present the results of the microstructure evolution, yield strength and strain hardening models for, respectively, the 6005A-T6 weld B and the 6056-T78 weld C.

The use of stainless steel instead of a high carbon steel as backing plate for the 6005A-T6 weld B has for consequence an increase of the precipitate radius, of the volume fraction of precipitates, and of the width of the heat affected zone (see Table 10). This leads to a 8% increase of the pseudo uniform elongation (see Table 11). Oppositely, the fracture strain is reduced by 20%. The use of high carbon steel instead of stainless steel as backing plate for the 6056-T78 weld C leads to a decrease of the precipitate radius, of the precipitate volume fraction and of the width of the heat affected zone, but, still, the strength of the weld, the pseudo uniform elongation and the fracture strain (see Table 11) becomes larger. This apparent contradiction with the 6005A-T6 welds can be explained by a larger ability of

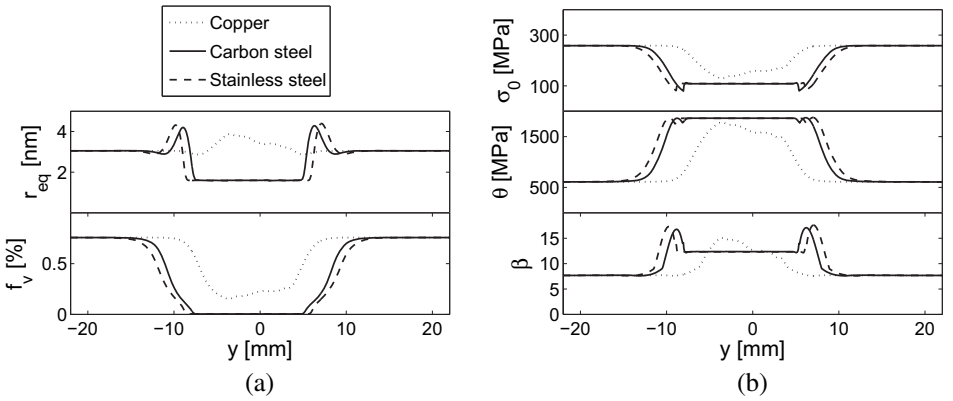

Fig. 37. Effect of the backing plate material on the predictions of (a) the microstructure evolution model (i.e. pondered by the volume fraction of each type of precipitate), (b) the initial yield strength σ_0 and the strain hardening (parameters θ and β) models for a 6005A-T6 weld performed with an advancing speed equal to 1000 mm/min and a rotational speed equal to 1000 rpm (weld B).

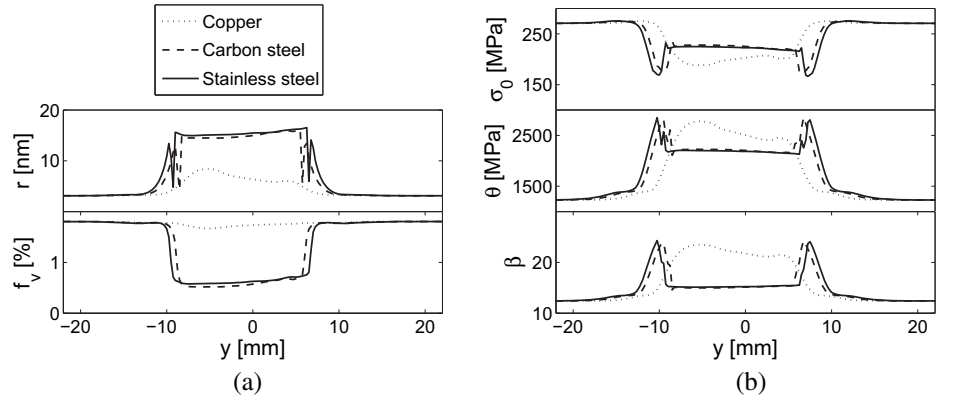

Fig. 38. Effect of backing plate material for a 6056-T78 weld on the predictions of (a) the mean precipitate radius r (i.e. the contribution of the radius of each type of precipitate multiplied by its volume fraction are added and the total is divided by f_v), the total precipitate volume fraction f_v, (b) the yield strength σ_0 and the strain hardening (parameters θ and β) models at mid-thickness. This weld was made with an advancing speed equal to 1100 mm/min and a rotational speed equal to 1100 rpm (weld C).

the 6056-T78 weld for natural aging after welding. Indeed, the parameter C_{lim}, i.e. the limit solid solution concentration for natural aging (see Section 3.2.3), is much lower in the 6056 alloy than in the 6005A alloy (see Table 4) due to the lower content of alloying elements in the 6005A alloy. Consequently, the lower volume fraction of precipitates in the 6056-T78 weld C with a high carbon steel backing plate favors the precipitation of GP zones after welding. The contribution to the strength of the GP zones compensates for the increase in size and decrease in volume fraction of the Q-type strengthening precipitates.

The use of copper instead of steel for the backing plate significantly changes the microstructure evolution and the tensile properties distribution for welds made of both alloys. Indeed, the maximum temperature is significantly reduced due to the heat sink resulting from the high thermal conductivity of the backing plate (see Table 12). Therefore, the heat affected zone is shifted towards the weld center (see Figs. 37 and 38). In the 6005A-T6 weld B with a copper backing plate, the precipitate radius and volume fraction are larger in the weld center due to an incomplete dissolution of the initial precipitates. Consequently, the yield strength and strain hardening parameter β are also larger in the weld center where fracture takes place. The yield strength and the pseudo ultimate tensile strength increase by 48% to 172 MPa instead of 116 MPa and 11% to 226 MPa instead of 203 MPa, respectively (see Table 11). The pseudo uniform elongation and the fracture strain decrease by 35% to 5.1% instead of 7.9% and 9% to 0.73 instead of 0.80, respectively (see Table 11). Fig. 39a presents the evolution of the temperature and precipitate volume fraction as a function of time at the weldline at mid-thickness for the 6056-T78 weld C. With a copper backing plate, the precipitate radius is the largest near the weld center towards the advancing side of the weld mainly featuring homogeneously distributed precipitates that have not dissolved at the peak temperature but have grown. In these welds, the nucleation of precipitates on dispersoïds is very limited due to the lower maximum temperature reached (about 450 °C). Fig. 38a shows that the volume fraction of precipitates is almost unchanged throughout the various weld regions preventing GP zones to form by natural aging after welding. Hence, the yield strength in the weld center is lower than after natural aging of the welds performed with a steel backing plate (see Fig. 38b). Nevertheless, as can be seen in Fig. 39b, the local yield strength is larger on the upper part of the weld than at mid-thickness. This is due to a higher temperature on the upper surface, favoring more dissolution than at mid-thickness and causing a larger solid solution concentration there. That enhances natural aging in that region of the weld. Consequently, the transverse tensile strength of the weld C with a copper backing plate is slightly larger than the weld C obtained with a steel backing plates. No improvement of the pseudo uniform elongation is found when compared to a high carbon steel backing plate. For the 6056-T78 welds, only the fracture strain presents a

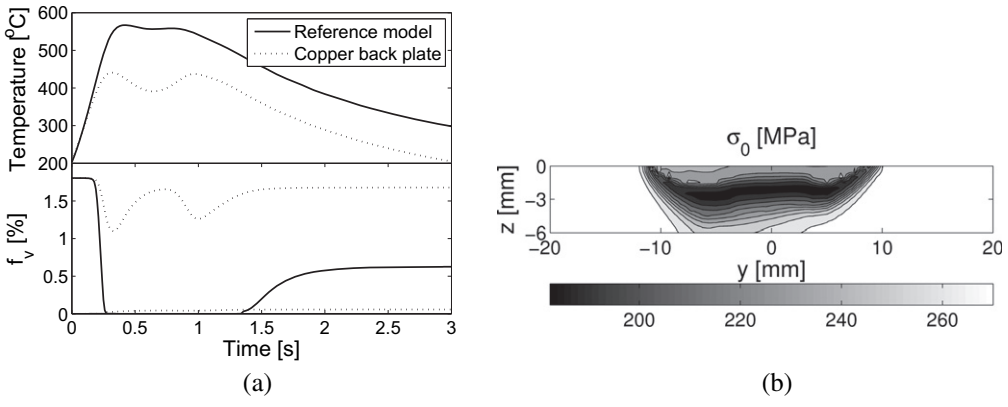

Fig. 39. (a) Effect of using a copper backing plate for a 6056-T78 weld on the predictions of the temperature and the precipitate volume fraction as a function of time in the weld center. (b) Map of the yield strength σ_0 for a 6056-T78 weld having a copper backing plate. This weld was made with an advancing speed equal to 1100 mm/min and a rotational speed equal to 1100 rpm (weld C).

significant improvement. This can be explained by a lower level of the stress triaxiality for low plastic strains due to the difference in tensile properties distribution shown in Fig. 38b.

As a conclusion, the use of a backing plate with a larger thermal conductivity is a potentially attractive route to improve the tensile properties of welds, depending on the alloy. Using a steel backing plate with a lower thermal conductivity (e.g. stainless steel) for a 6005A-T6 weld improves the pseudo uniform elongation but decreases its fracture strain. However, the effect is opposite for the 6056-T78 weld due to the larger ability of the 6056-T78 weld to naturally age. Using a copper backing plate is probably not the best choice due to the limited strength of copper alloys. A low strength of the backing plate leads to the sticking of the workpieces to the backing plate, requiring then to modify the welding conditions and avoid full penetration (in that case milling of the bottom side is needed). Bronze would be a better choice since the yield strength of bronze can reach up to 430 MPa. Furthermore, the low maximum temperature reached (i.e. 502 °C for the 6005A weld B) could lead to defected welds. Nevertheless, the simulation was attempted to reveal the potentialities of such welds. They show that using a copper backing plate leads to significant improvements of the 6005A-T6 weld strength. Due to the larger sensitivity of the 6056 alloy to heterogeneous precipitation compared to the 6005A alloy, the strength improvement of the 6056-T78 weld C with a copper backing plate remains small. The only significant improvement for the 6056-T78 weld with a copper backing plate compared to the same weld obtained with a steel backing plate is the doubling of the fracture strain.

5.2. Alloy design

In this section, the effect of the alloy composition on the tensile properties will be addressed and explained in relation to the microstructure evolutions and local tensile properties changes. It must be noted that the thermal cycles of the welds will be assumed unaffected by slight changes in the composition and state of the base material. The steady state torque is controlled by the plastic flow. Around the tool, the initial grain size, state of precipitation, and even the details of the composition and initial state of the base alloy rapidly become irrelevant since precipitates are dissolved, and dislocation accumulation is balanced by dislocation annihilation at the large strains occurring under the tool. This results in a torque which is the same, for a given advancing and rotational speed, for both 6005A and 6056 alloys, whatever their initial state, as shown in Fig. 40. The hypothesis of a constant torque seems therefore reasonable.

5.2.1. Effect of the proportion of alloying elements

This section aims at testing the effect of increasing the content of strengthening alloying elements. It is well known that increasing the alloying content increases the strength of the base material but the

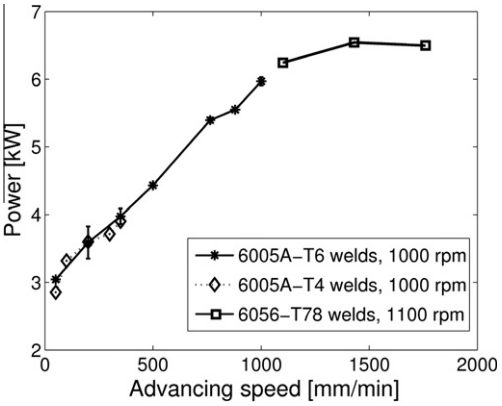

Fig. 40. Variation of the total power *P* estimated from the torque measurement as a function of the advancing speed for 6005A welds in T6 and T4 state (rotational speed equal to 1000 rpm) and for 6056-T78 welds (rotational speed equal to 1100 rpm).

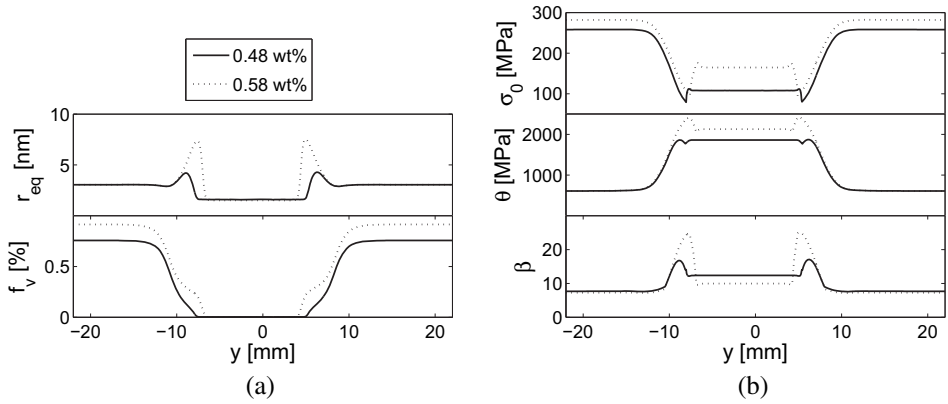

Fig. 41. Effect of the Mg content on the predictions of (a) the microstructure evolution (r_{eq} is the mean equivalent precipitate radius and f_v is the precipitate volume fraction), (b) the yield strength σ_0 and the strain hardening (parameters θ and β) models for a 6005A-T6 weld made with an advancing speed equal to 1000 mm/min and a rotational speed equal to 1000 rpm.

question remains whether it improves the overall tensile properties of a welded joint. In the simulations with the 6005A alloy reference, the Mg content has been increased from 0.48 wt.% to 0.58 wt.%. In the 6056 alloy, the Mg, Si and Cu alloying elements enter in the composition of the Q phase, and their contents have been increased by 20% each. In these calculations, the initial radius distribution was taken as the same as for the reference alloy but with a corrected density of precipitates within each size class.

Increasing the content in alloying elements could be responsible for the modification of the sequence and type of precipitation which are not accounted for in this simple analysis. For instance, in the 6005A alloy, heterogeneous precipitation often observed in 6xxx series aluminums containing a larger amount of alloying elements could require a change of the nucleation parameters (see Tables 3 and 4). Furthermore, some other phases might form in addition to the β' phase observed in the HAZ, as for instance the B' phase identified by Dumolt et al. [252] in the 6061 alloy containing more Mg/Si than the reference 6005A alloy.

Regarding the 6005A alloy, Fig. 41a presents the predicted equivalent precipitate radius and the precipitate volume fraction distribution at mid-thickness when increasing the Mg content. Fig. 41b presents the resulting yield strength and strain hardening parameters θ and β distributions at mid-thickness. The change of the yield strength in the HAZ remains limited (see Fig. 41b). The 0.58 wt.% Mg alloy is globally stronger due to its larger quantity of Mg in solid solution but this effect is compensated by the larger size of the precipitates in the HAZ (see Fig. 41a). Conversely, the pseudo uniform elongation and fracture strain of the initial 6005A-T6 alloy is higher than for the alloy with 0.58 wt.% Mg (see Table 11). This is due to the higher strength mismatch between the HAZ and the nugget favoring early localization in the HAZ of the alloy with a high Mg content.

Regarding the 6056 alloy, Fig. 42a presents the predicted precipitate radius and the precipitate volume fraction distribution at mid-thickness for the two compositions. Fig. 42b presents the yield strength and strain hardening parameters θ and β distributions at mid-thickness. The precipitate volume fraction in the weld center increases due to more intense heterogeneous precipitation on dispersoïds and a small volume fraction of very coarse homogeneous precipitation (r of 55 nm, see Table 10). The coarse homogeneous precipitation is not present in the original 6056 weld (see Fig. 42a). In the alloy with 20% more alloying element, this homogeneous precipitation tremendously coarsening is due to a very limited number of precipitates that are not dissolved during the welding process and hence grow during the cooling stage. The heterogeneous precipitation in the weld center involves also coarser precipitates than in the original 6056 weld (see Fig. 42a). The balance between a lower solid solution concentration, i.e. a lower capacity to naturally age and a higher precipitate volume fraction of slightly coarser precipitates in the weld center, induces no change of the yield strength in the weld

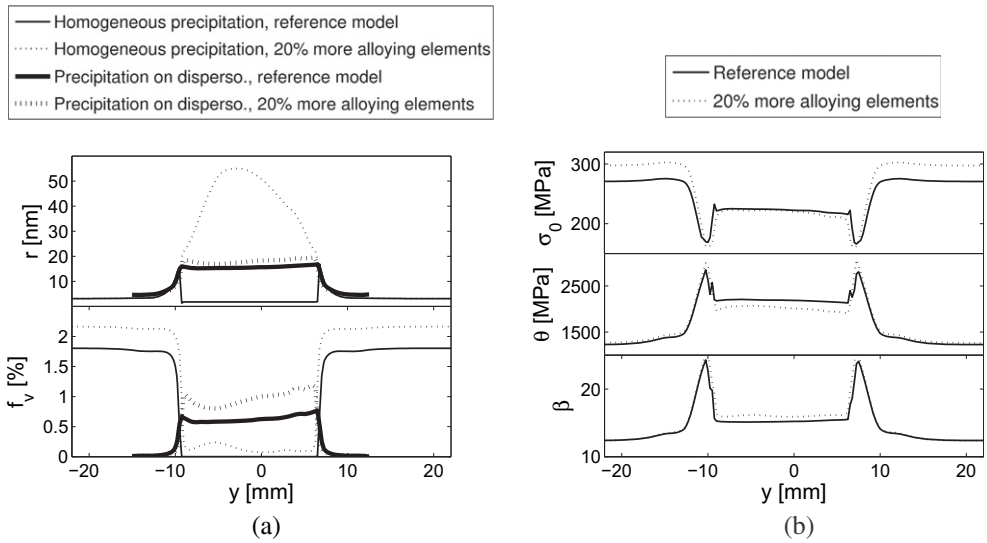

Fig. 42. Effect of the material of the backing plate on the predictions of (a) the mean precipitate radius r (i.e. pondered by the volume fraction of each type of precipitate), the total precipitate volume fraction f_v, (b) the yield strength σ_0 and the strain hardening (parameters θ and β) models at mid-thickness. This weld was performed with an advancing speed equal to 1100 mm/min and a rotational speed equal to 1100 rpm (weld C).

center. Furthermore, the yield strength remains also unchanged in the HAZ. The strain hardening parameter θ increases in the weak zone and decreases in the weld nugget (see Fig. 42a and Table 10). The strain hardening parameter β slightly increases in both zones of the weld. Consequently, the strength and ductility of the weld slightly decrease, see Table 11. The only significant improvement is the 80% increase of the fracture strain due, among others, to the lower strength of the weld delaying the void nucleation process. Since there are other ways to improve the fracture strain without affecting the strength of the weld (e.g. see Section 5.1.4), there is thus probably no real interest to increase the alloy content in the case of the 6056 welds.

As a conclusion, increasing the alloying element content in 6xxx series Al alloys is obviously a way to improve the strength of the base material, but it can be detrimental to the weld properties. Hence, it is recommended to limit the increase of alloy content in the limits required to obtain the desired base material strength to avoid a decrease of the weld efficiency (ratio of the weld to the base material ultimate tensile strength).

5.2.2. Effect of the intermetallics content

The intermetallic particles present in Al alloys result from the presence of Fe in the natural Al oxides. These intermetallic particles primarily intervene in the damage process since cavities are nucleated by the fracture of these phases (see Section 3.4.2). Purification of the alloy to remove the iron is a costly operation. Liu et al. [209] have shown that an enhanced solution treatment (with a slow increase of the temperature to reach dissolution) can also decrease the volume fraction of intermetallic particles and dispersoïds by respectively 30% and 20% and consequently improve the fracture strain by 20% in Al–Mg–Si alloys. Hence, other more simple routes than changing the Fe content can also lead to a reduction of the volume fraction of particles responsible for damage.

Tables 10 and 11 present the results of the damage model when reducing by 20% the volume fraction of intermetallic particles (i.e. parameter f_p) in welds A and B made of the 6005A-T6 alloy and in weld C made of the 6056-T78 alloy. In all these cases, the fracture strain is not significantly improved. Now, an improvement of the fracture strain could be expected for the "cold" 6005A-T6 weld if no second population of cavities had intervened in the damage process. Consequently, it is interesting

to ask the question: is it worth purifying the alloy? Tables 10 and 11 also present the effect of increasing by 20% the volume fraction of intermetallic particles for the same welds. In the 6005A-T6 welds, for the "hot weld" (weld A), the decrease in fracture strain is only of 1% but, for the "cold welds" (weld B), this decrease is more substantial and equal to 8%. In the 6056-T78 welds, the fracture strain is already low due to the contribution of a second population of cavities and is decreased by 6% when increasing f_p by 20%.

As a conclusion, decreasing the volume fraction of intermetallic particles in the alloy improves its fracture strain more significantly in "cold welds" if no second population of cavities are intervening in the damage process. Hence, only very low strength Al alloys may show significant improvement in fracture strain by reducing the amount of intermetallic particles when second population of cavities do not play any role. Now, substantially increasing the volume fraction of intermetallics may lead to decreases of the fracture strain.

5.2.3. Effect of the alloy state before welding

The initial state of the weld materials before welding was always T6 for the 6005A alloy and T78 for the 6056 alloy. The possibility of welding the same alloy starting from underaged conditions has also been investigated. For the 6005A alloy, two additional pre-welding conditions have been tested: welding in the T4 state and welding in an intermediate under-aged state (T4 + 2 h at 180 °C, see Simar et al. [42]). The predictions for the T4 base material weld are only valid if no precipitation on dislocations occurs in the HAZ which could happen in the 6005A alloy (see further for the 6056 alloy). The initial distribution of precipitates for the intermediate under-aged state is generated by the microstructure evolution model. For the 6056 alloy, only the effect of welding in a T4 state has been investigated. Since the microstructure evolution model for the 6056 alloy has only been validated for high temperature heat treatments [54], no intermediate under-aged state size class distribution has been simulated.

Regarding the 6005A alloy, Fig. 43a presents the predicted equivalent precipitate radius and the precipitate volume fraction distribution at mid-thickness when changing the base material state. Fig. 43a presents the resulting distributions of the yield strength and of the strain hardening parameters θ and β at mid-thickness. As expected for under-aged to peak aged conditions, the precipitate radius, the precipitate volume fraction, the initial yield stress, and the strain hardening parameter θ of the base material increase with increasing aging time. The strain hardening parameter β of the base material decreases with increasing aging time. The precipitate radius and volume fraction follow the same trend in the HAZ with only a limited increase of the precipitate volume fraction for the T4 base material state. As a consequence, the initial yield stress in the HAZ increases with aging time. The local

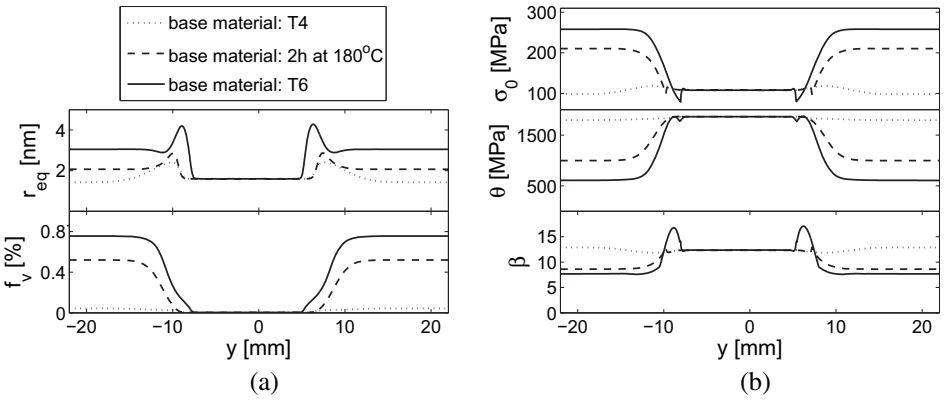

Fig. 43. Effect of the state of the base material on the predictions of (a) the microstructure evolution (r_{eq} is the mean equivalent precipitate radius and f_v is the precipitate volume fraction), (b) the yield strength σ_0 and the strain hardening (parameters θ and β) models for 6005A welds made with an advancing speed equal to 1000 mm/min and a rotational speed equal to 1000 rpm.

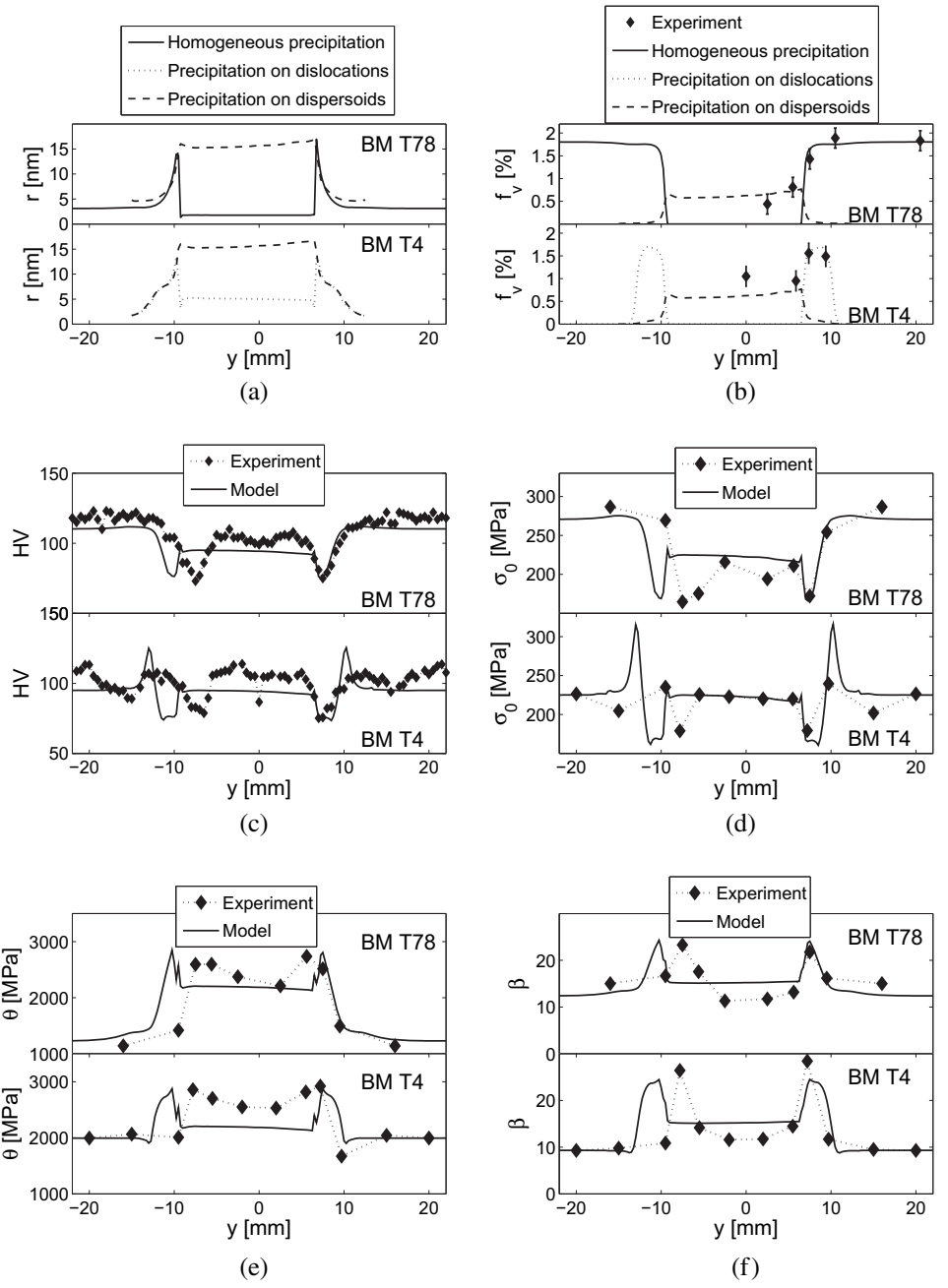

Fig. 44. Effect of the state of the base material on the predictions of (a) the mean precipitate radius r, (b) the precipitate volume fraction f_v, (c) the hardness, (d) the yield strength σ_0, (e) the strain hardening parameter θ and (f) the strain hardening parameter β for 6056 welds made with an advancing speed equal to 1100 mm/min and a rotational speed equal to 1100 rpm. Comparison with experiments: f_v (DSC measurements), hardness, σ_0, θ and β, are based on experimental results from Gallais et al. [34,54]. BM = base material.

yield strength remains unchanged in the weld nugget due to the dissolution at high temperature of the strengthening precipitates in all cases. Even after 2 h of artificial aging at 180 °C, the strain hardening parameters θ and β of the HAZ remain equal to the value corresponding to a T4 state and in the weld nugget. The consequence of these redistribution of the local tensile properties is a slightly smaller strength. The increase in pseudo uniform elongation of the welds is equal to 62% and 10% for, respectively, the T4 state and the intermediate under-aged state base materials. The fracture strain increases by 8% when welding in the under-aged condition and a second population of cavities should intervene in the damage process. In the case of the T4 base material, fracture occurs in the T4 base material.

Regarding the 6056 alloy, Fig. 44 presents the predicted precipitate radius and volume fraction distribution at mid-thickness when changing the state of the base material. The predicted volume fraction of precipitates is compared with DSC measurements. Fig. 44 also compares the measured and predicted hardness profiles, distributions of local yield strength and strain hardening parameters θ and β at mid-thickness. The model correctly reproduces the experiments except near the T4 base material where, associated to the precipitation in the HAZ, excessive strengthening is predicted. This is due to an over-estimation of the width of the HAZ where precipitation occurs. In the HAZ, precipitation occurs on dislocations in the HAZ for the T4 base material contrarily to the T78 welds [54,118]. Indeed, in the T78 welds, the homogeneously nucleated precipitates dissolve and growth in the various weld regions but no precipitation on dislocations is involved in any region of the weld (see Fig. 44b). The weld local properties show little difference when changing the state of the base material, i.e. only the level of the base material properties is affected. The only significant effect on the tensile properties is the increase by 12% of the pseudo uniform elongation.

As a conclusion, using under-aged base materials is only interesting if the aim is to improve the ductility of the weld without significantly affecting the strength. However, the strength of the base material is significantly reduced if the welding is performed with under-aged conditions.

5.3. Effects of a post-welding heat treatment

After welding, a large amount of alloying elements are dissolved in the Al matrix. Hence, it might be useful to re-precipitate these elements in order to strengthen the weld. This implies achieving a T6 type post-welding heat treatment, known to improve the weld strength [245,253,254].

Fig. 45 compares the predicted and measured hardness evolutions before and after a T6 post-welding heat treatment (PWHT), i.e. 6 h at 185 °C, applied to two 6005A welds. The predictions of the model, in particular, the level of the minimum hardness after PWHT as well as their location, are very well captured for both welding conditions, and this without any parameter tuning.

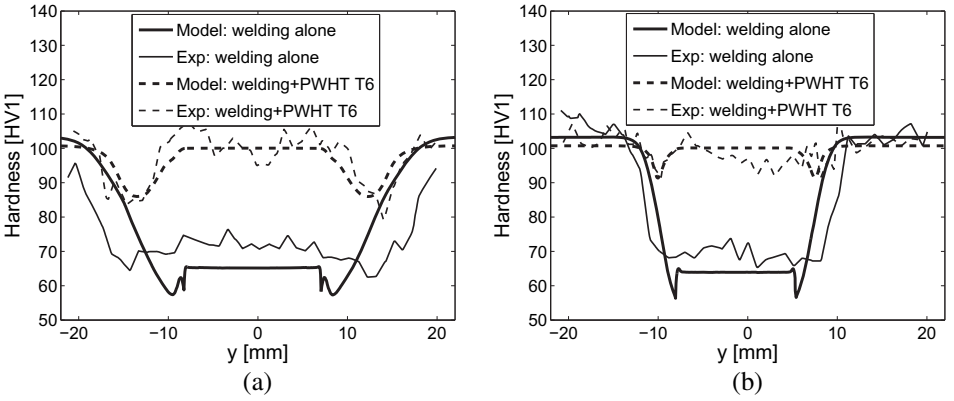

Fig. 45. Comparison of the measured and predicted hardness when a T6 post-welding heat treatment (PWHT) is considered for the 6005A welds. The rotational speed is equal to 1000 rpm and the advancing speed is equal to (a) 200 mm/min and (b) 1000 mm/min.

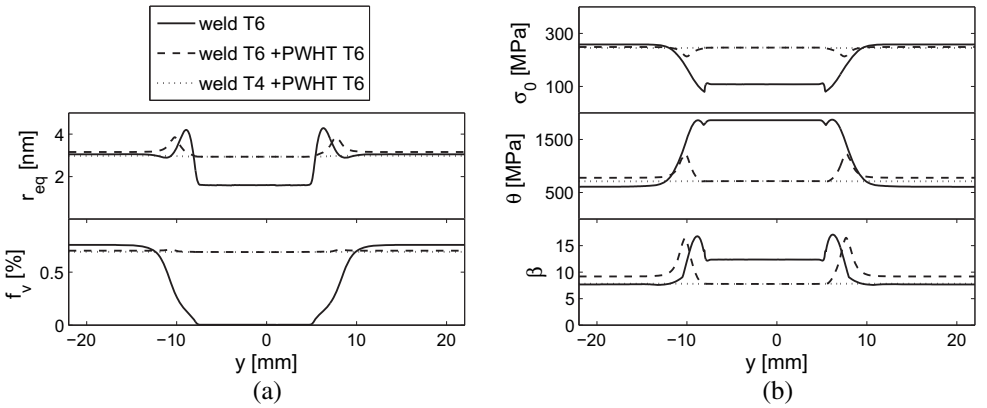

Fig. 46. Effect of a T6 post-welding heat treatment (PWHT) comparing two initial states of base material (T4 and T6) on the predictions of (a) the microstructure evolution (r_{eq} is the mean equivalent precipitate radius and f_v is the precipitate volume fraction), (b) the yield strength σ_0 and the strain hardening (parameters θ and β) models for a 6005A-T6 weld made with an advancing speed equal to 1000 mm/min and a rotational speed equal to 1000 rpm.

Fig. 46 compares the results of the microstructure evolution, yield strength and strain hardening models before and after the PWHT for the weld produced with an advancing speed equal to 1000 mm/min and a rotational speed equal to 1000 rpm. After the PWHT, the base material precipitate radius is restored in the weld nugget and new fine precipitates are formed in the weak HAZ, reducing the mean precipitate radius. The volume fraction is almost equal to the base material value throughout the weld. Consequently, the local yield strength is significantly improved and the strain hardening capacity is reduced in all zones of the weld. Table 11 compares the transverse tensile properties predicted before and after the PWHT. The pseudo yield strength is tremendously improved (by 62% for the weld produced at 200 mm/min and by a factor of 2 for the weld produced at 1000 mm/min). The smaller improvement in strength in the low advancing speed weld compared to the high advancing speed

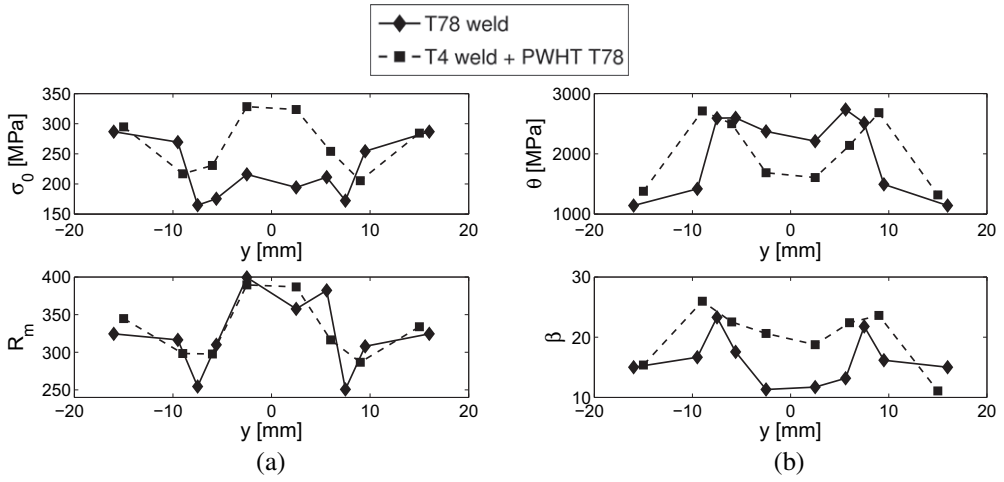

Fig. 47. Comparison of the measured local tensile properties for a 6056-T78 weld and a 6056-T4 weld with a post-welding heat treatment (PWHT) T78. (a) Yield strength σ_0 and ultimate tensile strength R_m and (b) Strain hardening parameters θ and β. The weld was produced with an advancing speed equal to 1100 mm/min and a rotational speed equal to 1100 rpm; results based on Gallais et al. [34].

Table 13
Measured transverse tensile properties of two FSW welds in Al alloy 6056. Effect of a post-welding heat treatment. The weld was produced with an advancing speed equal to 1100 mm/min and a rotational speed equal to 1100 rpm. Results from Gallais et al. [34]. R_p is the pseudo yield strength, R_m is the pseudo ultimate tensile strength and e_u is the pseudo uniform elongation. Note that in these welds the gage length is equal to 30 mm (while a gage length of 50 mm is generally used in the welds presented earlier).

Weld state	R_p (MPa)	R_m (MPa)	e_u (%)
Weld T78	184	265	5.6
Weld T4 + PWHT T78	207	273	3.1

weld is caused by the high volume fraction of large precipitates (see Table 10) in the low advancing speed weld which no longer produce precipitates with a size corresponding to the transition radius r_{trans} after the PWHT. The precipitates already present before the PWHT only keep growing during the PWHT, leading to a decrease of the strength. Due to the decrease in strain hardening capacity of the various zones of the weld, the pseudo uniform elongation increases by only 30%. The pseudo ultimate tensile strength increases by 6% for the weld produced with an advancing speed equal to 1000 mm/min but significantly decreases (by 50%) for the weld obtained with an advancing speed equal to 50 mm/min. In both welds, the fracture strain is reduced by 28%.

Fig. 46 also compares the predictions of the model chain when welding from T4 state and then performing the PWHT. The model predicts almost a full recovery of the properties of the base material even in the HAZ compared to a weld performed in T6 state and then post-weld heat treated. Fracture is predicted in the base material.

No simulation results for the 6056-T78 welds are presented since the precipitation model has only been validated for temperatures higher than 200 °C and is thus not adapted to predict the behavior of the alloy during an aging treatment. However, it could be interesting to compare the results obtained on the 6005A alloy with an alloy presenting a higher content in alloying elements. For this reason, experimental results of 6056 welds performed on the T4 state and post-weld heat treated to the T78 state are presented and discussed here (based on experiments by Gallais et al. [34]).

Fig. 47 presents the local yield strength and strain hardening parameters of the T78 weld and of the T4 weld with a PWHT of the T78-type. The strength of the alloy is significantly improved in the weak zone. In the weld center, the yield strength is improved but, due to a larger strain hardening ability of

Table 14
Summary of the effect of the various routes for process optimization suggested in Section 5 on the strength and ductility of 6005A and 6056 Al welds.

Optimization routes	Strength	Pseudo uniform elongation	Fracture strain
Process design			
Advancing speed ↗	↗↗	↗↗	↘ if advancing speed low ↗ if advancing speed high
Rotational speed ↘	∼	∼	∼
Preheating	6005A: ∼ 6056: ↘	6005A: ↗↗ 6056: ↘	6005A: ↘ 6056: ↗
Cooling rate ↘	6005A: ∼ 6056: ↘	6005A: ↘ 6056: ∼	6005A: ↗ 6056: ↗↗
Cooling rate ↗	6005A: ∼ 6056: ↗	6005A: ↗ 6056: ↗↗	6005A: ∼ 6056: ↗
Highly conductive backing plate	6005A: ↗↗ 6056: ↗	6005A: ↘ 6056: ↗↗	6005A: ↘ 6056: ↗↗
Alloy design			
Alloying elements ↗	↘	↘	6005A: ↘↘ 6056: ↗↗
Intermetallics ↘	Unaffected	Unaffected	∼
Underaged initial state	↘	↗	↗
Post-welding heat treatment			
T6 PWHT	↗↗	↘ if advancing speed low ↗ if advancing speed high	↘↘

the post-weld heat treated samples, the ultimate tensile strength is not improved. Table 13 presents the transverse tensile properties of both welds. The yield strength and the pseudo ultimate tensile strength increase by 13% and 3% respectively. Oppositely, the pseudo uniform elongation decreases by 45%. The low improvement in strength of PWHT welds can be explained by the significant heterogeneous precipitation in the weld center during welding, limiting the amount of solid solution remaining for the production of strengthening precipitates after aging.

As a conclusion, for the 6005A, a T6 post-welding heat treatment (PWHT) is the most interesting route suggested in this study in order to improve the tensile properties of a friction stir weld, if the fracture strain is not a major design parameter. The welding in T4 state followed by a PWHT causes complete recovery of the base material tensile properties. Nevertheless, such a PWHT is practically impossible for very large structures. Furthermore, this post-welding heat treatment slightly over-ages the base material. Regarding the 6056 welds, the strength is only slightly improved by the PWHT and the ductility is significantly reduced. Hence, increasing the processing complexity by applying such a heat treatment on the welded structure, is only justified for alloys in which heterogeneous precipitation is not favored (like for the 6005A alloy).

5.4. Summary

Table 14 summarizes the main results of this section in terms of the possible routes for properties optimization. First order improvements of the strength and/or the ductility can be expected if the workpiece is preheated, if cooling is enhanced during the welding process (e.g. by welding with a high advancing speed and through the use of a highly conductive backing plate) or by performing a post-welding heat treatment.

6. Conclusions

Integrated computational engineering is a modern way to simulate complex material systems and to accelerate insertion of new materials and processes into common engineering practice. Friction stir welding (FSW) of age-hardenable Al alloys is a good illustration of this approach. FSW is indeed a complex process involving a combination of many physical phenomena such as the generation of high temperatures combined with large plastic deformations, thermal and material flows, dissolution/coarsening of fine precipitates and recrystallization, resulting in heterogeneous material microstructures across the welded joints. All those phenomena occur simultaneously during the welding process and determine the end use properties of the welded products. One may develop many physics based models to describe independently the evolutions resulting from these phenomena but it would be a gigantic task, almost impossible and, in any case, uneconomical in terms of computing time, to try to fully inter-couple all these models. Therefore, the integration into a model chain appears to be the most reasonable and promising approach to optimize all parameters of such a manufacturing process. Integration is more than juxtaposing existing models; it requires expertise at all steps to select the appropriate models, the right assumptions and to determine the most relevant experimental and identification schemes to validate them, taking into account that the computing time and experimental efforts must remain within acceptable limits. This is where the scientific challenges sit and where "the devil enters in the details".

The objective for the FSW process is to minimize the knock-down factors on the weld mechanical properties by a control of the thermal cycles associated to the welding process and of the evolution of the strengthening precipitates, all being intimately related. More precisely, in order to illustrate the optimization strategy for process parameters selection and alloy design, the focus in this paper has been laid upon the critical load corresponding to the onset of plastic deformation (the pseudo yield strength), on the maximum load carried by the joint (the pseudo ultimate tensile strength) and on the associated elongation (pseudo uniform elongation) as well as on the fracture strain. These end use properties important for structural integrity and for forming operations depend not only on the base material composition and temper but also on the relative dimension and strength of the various zones across the welded joints influenced by the FSW parameters as well as on a possible heat

treatment after welding. The number of parameters which can be used for process optimization, and the somewhat intricate relationships between these parameters and the overall knock down factor, justifies an integrated modeling effort. Table 14 summarized the improvements in terms of tensile properties that can be reached by playing with different available parameters.

Here are some of the key points regarding the selection and assumption for each constituent of the model chain:

- *The thermal model* must capture the temperature cycles in the workpieces. Accounting for a simplified material flow field within a purely thermal approach allows capturing the temperature redistribution associated to material convection as well as the asymmetry in the temperature profile while significantly reducing the calculation time compared to a fully coupled model.
- *The precipitation model* must be able to predict the precipitate nucleation, growth, coarsening and dissolution as a function of the local thermal history. Accounting for the competition between precipitate dissolution and coarsening allows the prediction of the complex microstructure evolution in the heat affected zone. Furthermore, accounting for heterogeneous precipitation in alloys containing a high content of alloying elements is essential to correctly capture the hardening related to precipitation, solid solution and GP zones.
- *The yield strength and strain hardening models* must predict the local tensile properties from a knowledge of the main microstructural features. Concerning the yield strength model, it is essential to account for the difference in strengthening by natural aging of high alloyed Al (e.g. the 6056 alloy) compared to low alloyed Al (e.g. the 6005A alloy). Concerning strain hardening, the size and distribution of precipitates significantly affect the strain hardening ability due to the storage of Orowan loops and the influence on dislocation glide delocalization. The description of the strain hardening ability is of prime importance if the ductility and fracture behavior of the welded alloy is a major design parameter.
- *The finite element model of a transverse tensile test coupled with a damage model* must finally enable the prediction of the end-use properties of the weld even though the distribution of mechanical properties in that sample is highly heterogeneous. The mismatch and distribution of strength throughout the weld zones needs to be correctly captured, both for the local behavior but also because of their influence on the evolution of the stress triaxiality, to produce reliable predictions of the tensile strength properties. The use of a micro-mechanics damage model providing a direct link between the void nucleation, growth and coalescence mechanisms and the intermetallic particles volume fraction and shape is needed to capture the variations of the ductility expressed either in terms of the pseudo uniform elongation or the fracture strain.

The development of an integrated model chain procedure requires the validation of its various elements. The process model is generally validated by measurements of local temperature and visualization of the material flow; it may also require the measurement or a predictive estimate of the loads on the tooling. The microstructure evolution model is generally validated based on characterization analysis (e.g. optical microscopy for the grain size, SEM for micrometric size phases and TEM for nanometric size precipitates). Simpler but indirect techniques such as differential scanning calorimetry (DSC) provide an estimate of the relative change in the precipitate volume fraction. In the particular case of the ''size class model'' selected in this paper, an initial size class distribution is required. This distribution could also be generated by the model but, then, a very reliable nucleation law must be used and validated. Provided the precipitate composition is well known, Small Angle Scattering (by X-rays, SAXS, or by neutrons, SANS), although not easily applicable to 6xxx series Al alloys, is a powerful technique to access nonetheless the volume fraction but also the precipitate size distribution [146,255]. The yield stress, strain hardening and damage models must also be validated by mechanical tests performed on the heat treated and welded materials. These tests include hardness indentation, tensile tests, three point bend tests (SE(B)), and tests on notched and on fracture mechanics compact tension specimens (CT).

The development of all the models in the model chain may not be always required and each one of them can of course be replaced by appropriate experimental data. As examples, in an application to Al 6xxx series friction stir welds:

- the thermal model can be replaced by measured temperatures cycles (e.g. [63]),
- the precipitate evolution model can be replaced by TEM measurements (even though this is probably more time consuming than developing and validating a model) and SAXS or SANS measurements [146],
- the yield strength and strain hardening model can be replaced by extracting micro-tensile specimens in the various regions of the weld [6,42].

It was one of the challenge of the model presented in this paper to voluntarily include simplifications that are compatible with limited calculation times required for performing extensive optimization analysis. Enhancements can of course always be considered if needed, but this would be at the expense of the computing time.

- Concerning the thermal model, for the 6xxx series Al, the strain rate associated to the material rotation around the tool is not significantly impacting the hardening of the weld contrarily to its first order effect on the thermal cycles. Now, in order to model strain hardenable Al alloys (e.g. 5xxx series Al alloys) or dissimilar welds, the material flow around the tool should be accounted for. Indeed, for strain hardenable Al alloys recrystallization is dictated by the locally large strain rates and temperatures in the weld nugget.
- Concerning the microstructure evolution model, the models presented here already account for several sophisticated aspects inherent to the precipitation in 6xxx series Al alloys but the presence of different types of meta-stable precipitates could be considered if necessary [142,149]. The nucleation laws were kept to the simplest representation which do not fully account for the formation of GP zones after welding and hence natural aging is treated by post-processing. In the case of the treatment of peak aged materials, the model used here is sufficient to describe the microstructure evolution but the treatment of under-aged conditions involving nucleation on GP zones requires a specific validation of the model describing the nucleation kinetics at low temperatures. Note also that the approach would remain similar for other Al series (2xxx, 7xxx) though with a complete (and time consuming) re-identification of the parameters.
- The strain hardening model used in the present study is relatively new and needs further validation and developments. For instance, including kinematic hardening will be mandatory when dealing with cyclic loading problems.
- Considering the damage model, for instance, if applied to high strength aluminum alloys (e.g. 7xxx series), the formation of precipitate free zones (PFZ) should be accounted for, see Refs. [10,225,226].

The model chain could also be enriched in order to predict other weld properties like residual stress distribution, crack propagation, fatigue and corrosion resistance. The residual stress distribution can be treated by a thermomechanical analysis of the welding process, see recent Refs. [78,256–258]. Fracture toughness (i.e. prediction of K_{IC}) and crack propagation (i.e. prediction of the J–R curve) can be predicted by Gurson type damage models but this requires a fully coupled approach with damage based FE calculation, see e.g. Refs. [228,242,259–261]. The fatigue resistance of the processed material is a major issue in particular in aeronautical applications, see Golestaneh et al. [262] for a fatigue crack growth model in FSW welds. Another important possible extension concerns corrosion issues associated to microstructure evolutions and residual stresses in Al alloy friction stir welds [263]. Modeling of the corrosion behavior of Al alloys is at the very beginning [264] and the progress will directly impact the transfer to friction stir welding applications.

Acknowledgements

The authors would like to acknowledge L. Ryelandt, S. Ryelandt and M. Sinnaeve as well as the technical staff of iMMC and ONERA for support for the experiments. This research was carried out under the University attraction Poles (IAP) Programme Phase VI, Project M3PHYSTO, financed by the Belgian State, Federal Office for Scientific, Technical and Cultural Affaires. The calculations have been performed on the CISM-UCL, Belgium computer facilities.

Nomenclature

a (m) lattice parameter of the matrix
A_0 (kJ/mol) energy barrier parameter for precipitate nucleation
A_f (m) minimum cross-section of a broken specimen
$A_{HV\ (HV/Pa)}$ slope of the linear regression between HV and σ_0
A_i (m) initial cross-section of a tensile specimen
b (m) magnitude of Burger's vector
B_{HV} (HV) parameter of the linear regression between HV and σ_0
C function of S_v and f (damage model)
C_0 content of the base alloy in precipitation controlling element
CC_A (W/m^2 K) contact conductivity between workpiece and backing plate under the shoulder
CC_B (W/m^2 K) contact conductivity between workpiece and backing plate at the back of the tool
C_e^i equilibrium solute concentration of element i at the precipitate/matrix interface
C_{e0}^i pre-exponential term to C_e^i
C_{int}^i solid solution concentration of element i at the precipitate matrix interface
C_{lim} limit solid solution content for natural aging
cp (J/kg K) material specific heat
C_p^i precipitate content in element i
C_{pin} relative proportion of friction heat dissipated at tool/pin interface
$C_{pin\ tip}$ relative proportion of friction heat dissipated at tool/pin tip interface
$C_{shoulder}$ relative proportion of friction heat dissipated at tool/shoulder interface
C_{ss}^i solid solution concentration of element i in the matrix
D_i (m^2/s) diffusion coefficient of element i
D_0^i (m^2/s) pre-exponential term to D_i
e elongation
e_u ultimate tensile strain
e_x, e_y, e_z unit vectors parallel to the x, y and z direction respectively
f volume fraction of primary voids
f_2 volume fraction of secondary voids
f_0 initial volume fraction of primary voids
f_0^{eff} effective initial volume fraction of primary voids
$\overline{F}_j$ (N) mean strength of type j precipitates
F_{jk} (N) strength of precipitate of type j in size class k
f_{nucl} nucleated volume fraction of voids
f_p volume fraction of particles responsible for damage
f_v^j volume fraction of precipitates of type j
f_v total volume fraction of precipitates
F_z (N) force on the welding tool in z direction
g function of S_v and f (damage model)
G (Pa) shear modulus
h_1 function of S_v and f (damage model)
h_2 function of S_v and f (damage model)
h_B (m) thickness of the backing plate
h_{back} convection coefficient under the backing plate (not for present thermal model)
h_p (m) pin height
HV (HV1) Vickers hardness
J tensor associated to the void axis
J_0 (#/m^3 s) pre-exponential term to the nucleation rate
J_{nucl} (#/m^3 s) nucleation rate
K solubility product of a precipitate
k^* parameter equal to 1 if $r > r_{trans}$ and equal to 0 if $r < r_{trans}$
K_∞ equilibrium solubility product across a planar interface
K_0 pre-exponential term to K_∞

k_1 (m^{-1}) proportionality constant for dislocation storage
k_2 proportionality constant for dynamic recovery
K_2 secondary voids growth rate
k_β constant linking yield strength to dynamic recovery rate β
k_i (Pa wt.%$^{2/3}$) constant for the effect of the content of element i in solid solution on yield strength
K_{NA} (Pa) constant for the natural aging model
k_s parameter for void nucleation
$k_{\theta dp}$ (Pa) constant for the dynamic precipitation effect on the storage parameter θ
l (m) mean precipitates distance in the glide plane of a dislocation
L_0 (m) mean distance between moving dislocations of opposite sign
$L_{i\,j\,k\,l}$ (Pa) elastic moduli
l_j (m) precipitates distance in the glide plane of a dislocation for type j precipitates
M Taylor factor
M_z (Nm) torque along z axis
n strain hardening exponent
N_A (mol^{-1}) Avogadro number
n_{class} number of precipitates size classes
n_{el} number of elements composing a precipitate
$N_{j,0}$ (#/m^3) number of potential nucleation sites for precipitation of type j
N_{jk} (#/m^3) density of precipitates of type j in size class k
n_{type} number of types of precipitates
P (W) total mechanical power
P_d projector tensor
P_{in} (W) total mechanical power dissipated by friction and plastic deformation during welding
$p(m)$ mean probability for a moving dislocation to meet m precipitates encircled by an Orowan loop
$p_{shoulder}$ (Pa) pressure under the shoulder
q parameter of the damage model calibrated as a function of f_0 and W_0
Q_d^i (J/mol) activation energy for diffusion of element i
Q_e (J/mol) apparent solvus boundary enthalpy
q_S (W/m^2) specific surface heat source
Q_S (W) total power dissipated at the tool/workpiece interface during welding
q_V (W/m^2) specific volume heat source
Q_V (W) total power dissipated by plastic deformation during welding
r (m) mean precipitate radius
R (Pa) engineering stress
r_a (m) radial distance from tool axis
r_c (m) critical precipitate radius
r_{cl} (m) precipitate radius corresponding to the loss of coherency
r_{eq} (m) mean equivalent precipitate radius (assuming it is a sphere)
r_g geometric factor depending on the void arrangement
R_g (J/K mol) universal gas constant
r_i (m) pin radius
r_{jk} (m) precipitate radius of type j in class k
r_L Lankford coefficient for anisotropy
R_m (Pa) ultimate tensile strength
R_{mBM} (Pa) ultimate tensile strength of base material
r_{min} (m) minimum radius of the thermomechanically affected zone (TMAZ)
r_o (m) shoulder radius
R_p (Pa) yield strength
r_{trans} (m) radius of transition between dislocation shearing and bypassing precipitates
R_x, R_y, R_z (m) radius of voids in the x, y and z direction, respectively
S_v logarithmic aspect ratio of voids

S_{v0} initial value of S_v
t (s) time
T (K) temperature
t_d (s) traveling time associated to the mean spacing between two dislocations of opposite sign
T_{in} (K) initial workpiece temperature
T_{max} (K) maximum temperature
t_{preci} (s) inverse of the frequency of precipitates distribution
v (m/s) advancing speed
v_j (m/s) rate of dissolution or coarsening of precipitates of type j
V_m (m^3/mol) molar volume of Mg_2Si
$v_{material}$ (m/s) material velocity at the tool/workpiece interface
V_p (m^3) volume of the TMAZ
v_r (m/s) relative velocity of two moving dislocations
v_{tool} (m/s) tool velocity at the tool/workpiece interface
W void aspect ratio
W_0 initial void aspect ratio
W_p aspect ratio of particles responsible for damage
x (m) welding direction
X tensor associated to the void axis
x_i atomic composition of element i in a precipitate
y (m) transverse direction
y_0 (m) annihilation distance between two dislocations of opposite sign in a pure material
y_a (m) annihilation distance between two dislocations of opposite sign in an alloy
y_{preci} (m) annihilation distance between two dislocations of opposite sign when at least one precipitate surrounded by an Orowan loop is met during the time required to encounter another moving dislocation
z (m) through thickness direction
Z Zeldovitch factor
α constant of the dislocation density contribution to flow stress
α_2 function of S_v and f (damage model)
α_d damage model parameter (function of n)
α_e precipitate elongation ratio
β dynamic recovery rate strain hardening parameter
β_0 dynamic recovery rate strain hardening parameter of a pure material
β^* (s^{-1}) atomic impingement rate
β_{min} minimum of β at the peak strength
β_{preci} dynamic recovery rate hardening parameter associated to y_{preci}
β_Γ dislocation line tension constant
γ proportion of P_{in} associated to volume heat sources
Γ (N) dislocation line tension
γ_d geometric factor depending on the voids arrangement
γ_{int} (J/m^2) precipitate/matrix interface energy
γ_p local plastic shear strain
δ ratio of material velocity to tool velocity at the tool/workpiece interface
ΔG^* (J/mol) energy barrier for precipitation
ΔG_e (J/m^3) elastic strain energy change associated to precipitate nucleation
ΔG_v (J/m^3) volume free energy change associated to precipitate nucleation
δ_K Kronecker tensor
Δr (m) range of precipitate radius inside a size class
$\Delta\varepsilon_{nucl}$ strain interval over which voids nucleate
$\Delta\sigma_{nucl}$ stress interval over which voids nucleate
ε_f macroscopic true fracture strain
ε^p plastic strain tensor

ε_p equivalent plastic strain
$\varepsilon_{p,nucl2}$ equivalent plastic strain for nucleation of secondary voids
$\bar{\varepsilon}_y^p$ mean plastic strain
ε_u true strain at the onset of necking
ζ parameter of heat source generated by plastic deformation
η factor of power loss in the tool
η_d function of S_v and f (damage model)
θ (Pa) dislocation storage strain hardening parameter for an alloy
θ_0 (Pa) dislocation storage strain hardening parameter for a pure material
θ_{IV} (Pa) stage IV strain hardening rate
θ_a angular position along the tool axis
θ_{dp} (Pa) dynamic precipitation contribution to the storage parameter θ
κ function of S_v and f (damage model)
λ (W/mK) material thermal conductivity
λ_d particle distribution factor
μ friction coefficient
ν number of precipitates encountered before two moving dislocations meet
ν_φ number of precipitates having an Orowan loop efficiently stored around it encountered before two moving dislocations meet
ρ (#/m^3) dislocation density
ρ_a (kg/m^3) material density
ρ_{init} (#/m^3) initial dislocation density
σ (Pa) Cauchy stress tensor
σ_0 (Pa) true yield stress
σ_0^{max} (Pa) maximum yield strength
$\sigma_{0/NA}$ (Pa) yield strength after natural aging
σ' (Pa) deviatoric tensor part of the Cauchy stress tensor
σ_c (Pa) critical stress for primary void nucleation
σ_{c2} (Pa) critical stress for secondary void nucleation
σ_d (Pa) grain size contribution to the flow stress
σ_{eq} (Pa) von Mises equivalent stress
σ_f (Pa) friction stress of a the pure material (Al)
σ_h^g (Pa) generalized hydrostatic stress
σ_{pl} (Pa) dislocation density contribution to the flow stress
σ_{preci}^j (Pa) contribution to the flow stress of the precipitates of type j
σ_{princ}^{max} (Pa) overall maximum principal stress
$\left(\sigma_{princ}^{particle}\right)^{max}$ (Pa) maximum principal stress in the particle
σ_{sat} (Pa) saturation stress
σ_{SHT}^{init} (Pa) yield strength after a solution heat treatment
σ_{SHT}^{NA} (Pa) yield strength after a solution heat treatment and natural aging
σ_{ss} (Pa) solid solution contribution to the flow stress
σ_u (Pa) flow stress at necking
σ_y (Pa) flow stress
τ_0 (Pa) flow shear stress at the beginning of yielding
$\tau_{contact}$ (Pa) shear stress at the tool/workpiece interface
τ_y (Pa) flow shear stress
φ efficiency of dislocation storage
Φ flow potential
φ_j wetting function
χ void spacing
ω (rad/s) rotational speed

References

[1] Thomas WM, Nicholas ED, Needham JC, Murch MG, Templesmith P, Dawes CJ. GB patent application no. 9125978.8, December 1991; US patent no. 5460317, October 1995.
[2] Benzerga AA, Besson J, Pineau A. Anisotropic ductile fracture – part II: theory. Acta Mater 2004;52:4639–50.
[3] Lassance D, Fabrègue D, Delannay F, Pardoen T. Micromechanics of room and high temperature fracture in 6xxx Al alloys. Prog Mater Sci 2007;52:62–129.
[4] Pineau A, Pardoen T. Failure mechanisms of metals. In: Comprehensive structural integrity encyclopedia, vol. 2. Elsevier; 2007[Chapter 6].
[5] Simar A, Nielsen KL, de Meester B, Tvergaard V, Pardoen T. Micro-mechanical modelling of ductile failure in 6005A aluminium using a physics based strain hardening law including stage IV. Eng Fract Mech 2010;77(13):2491–503.
[6] Nielsen KL, Pardoen T, Tvergaard V, de Meester B, Simar A. Modelling of plastic flow localisation and damage development in friction stir welded 6005A aluminium alloy using physics based strain hardening law. Int J Solids Struct 2010;47(18–19):2359–70.
[7] Chéhab B, Bréchet Y, Véron M, Jacques PJ, Parry G, Mithieux J-D, et al. Micromechanics of high-temperature damage in dual-phase stainless steel. Acta Mater 2010;58(2):626–37.
[8] Benzerga AA, Leblond JB. Ductile fracture by void growth to coalescence. Adv Appl Mech 2010;44:169–305.
[9] Allison J, Backman D, Christodoulou L. Integrated computational materials engineering: a new paradigm for the global materials profession. J Mater Nov 2006;25:27.
[10] Pardoen T, Scheyvaerts F, Simar A, Tekoğlu C, Onck PR. Multiscale modeling of ductile failure in metallic alloys. C R Phys 2010;11:326–45.
[11] Dons AL. The Alstruc homogenization model for industrial aluminum alloys. J Light Met 2001;1:133–49.
[12] Gandin CA, Bréchet Y, Rappaz M, Canova G, Ashby M, Shercliff H. Modelling of solidification and heat treatment for the prediction of yield stress of cast alloys. Acta Mater 2002;50:901–27.
[13] Grong O, Shercliff HR. Microstructural modelling in metals processing. Prog Mater Sci 2002;47:163–282.
[14] Cram DG, Zurob HS, Bréchet Y, Hutchinson CR. Modelling discontinuous dynamic recrystallization using a physically based model for nucleation. Acta Mater 2009;57:5218–28.
[15] Mishra RS, Ma ZY. Friction stir welding and processing. Mater Sci Eng R 2005;50:1–78.
[16] Nandan R, DebRoy T, Bhadeshia HKDH. Recent advances in friction-stir welding – process, weldement structure and properties. Prog Mater Sci 2008;53:980–1023.
[17] Threadgill PL, Leonard AJ, Shercliff HR, Withers PJ. Friction stir welding of aluminium alloys. Int Mater Rev 2009;54(2):49–93.
[18] Shercliff HR, Lovatt AM. Selection of manufacturing processes in design and the role of process modelling. Prog Mater Sci 2001;46(3–4):429–59.
[19] Kamp N, Sullivan A, Robson JD. Modelling of friction stir welding of 7xxx aluminium alloys. Mater Sci Eng A 2007;466:246–55.
[20] Fujii H, Cui L, Maeda M, Nogi K. Effect of tool shape on mechanical properties and microstructure of friction stir welded aluminum alloys. Mater Sci Eng A 2006;419:25–31.
[21] Mahoney M, Nelson T, Sorenson C, Packer S. Friction stir welding of ferrous alloys: current status. Mater Sci Forum 2010;638–642:41–6.
[22] Mahoney M, Nelson T. Friction stir welding butt-and T-joints in thin HSLA-65 steel plate with low distortion. In: Proc 8th int symp FSW 2010, Timmendorfer Strand, Germany; 2010.
[23] Larsson H, Karlsson H, Stolty S, Bergqvist EL. Joining of dissimilar Al-alloys by friction stir welding. In: Proc 2nd int symp FSW 2000, Gothenburg, Sweden; 2000.
[24] Shibayanagi T, Maeda M. Characteristics of microstructure in dissimilar FSW joints of 5083/6061 Al alloys. In: Proc 5th int symp FSW 2004, Metz, France; 2004.
[25] Gerard H, Ehrstrom JC. Friction stir welding of dissimilar alloys for aircraft. In: Proc 5th int symp FSW 2004, Metz, France; 2004.
[26] Steuwer A, Peel MJ, Withers PJ. Influence of welding speed on the properties of AA5083-AA6082 dissimilar friction stir welds. In: Proc 6th int symp FSW 2006, Saint-Sauveur, Canada; 2006.
[27] Khodir SA, Shibayanagi T. Friction stir welding of dissimilar AA2024 and AA7075 aluminium alloys. Mater Sci Eng B 2008;148:82–7.
[28] Cavaliere P, De Santis A, Panelle F, Squillace A. Effect of welding parameters on mechanical and microstructural properties of dissimilar AA-6082-AA2024 joints produced by friction stir welding. Mater Des 2009;30:609–16.
[29] Jonckheere C, Simar A, de Meester B. Mechanical properties of dissimilar friction stir welds joining 6xxx to 2xxx aluminium alloys. In: Proc 8th int symp FSW 2010, Timmendorfer Strand, Germany; 2010.
[30] Simar A, Jonckheere C, Deplus K, Pardoen T, de Meester B. Comparing similar and dissimilar friction stir welds of 2017-6005A aluminium alloys. Sci Technol Weld Join 2010;15(3):254–9.
[31] Yamamoto M, Gerlich A, North TH, Shinozaki K. Cracking in dissimilar Mg alloy friction stir spot welds. Sci Technol Weld Join 2008;13(7):583–92.
[32] Chen T. Process parameters study on FSW joint of dissimilar metals for aluminium-steel. J Mater Sci 2009;44:2573–80.
[33] Lee CY, Choi DH, Yeon YM, Jung SB. Dissimilar friction stir spot welding of low carbon steel and Al–Mg alloy by formation of IMCs. Sci Technol Weld Join 2009;14(3):216–20.
[34] Gallais C, Simar A, Fabrègue D, Denquin A, Lapasset G, de Meester B, et al. Multiscale analysis of the strength and ductility of AA 6056 aluminum friction stir welds. Metal Mater Trans 2007;38A(5):964–81.
[35] Liu G, Murr LE, Niou CS, Mc Clure JC, Vega FR. Microstructural aspects of the friction-stir welding of 6061-T6 aluminum. Scripta Mater 1997;37:355–61.
[36] Su JQ, Nelson TW, Mishra RS, Mahoney MW. Microstructural investigation of friction stir welded 7050-T651 aluminium. Acta Mater 2003;51:713–29.

[37] Rhodes CG, Mahoney MW, Bingel WH, Spurling RA, Bampton CC. Effects of friction stir welding on microstructure of 7075 aluminum. Scripta Mater 1997;36:69–75.
[38] Cabibbo M, Meccia E, Evangelista E. TEM analysis of a friction stir-welded butt joint of Al–Si–Mg alloys. Mater Chem Phys 2003;81:289–92.
[39] Lee WB, Yeon YM, Jung SB. Evaluation of the microstructure and mechanical properties of friction stir welded 6005 aluminum alloy. Mater Sci Technol 2003;19:1513–8.
[40] Sato YS, Park SHC, Kokawa H. Distribution of tensile property and microstructure in friction stir weld of 6063 aluminum. Metal Mater Trans A 2001;32:3023–31.
[41] von Strombeck A, dos Santos JF, Torster F, Laureano P, Koak M. Fracture toughness behaviour of FSW joints on aluminium alloys. In: Proc 1st int symp FSW 1999, Thousand Oaks, California, USA; 1999.
[42] Simar A, Bréchet Y, de Meester B, Denquin A, Pardoen T. Sequential modeling of local precipitation, strength and strain hardening in friction stir welds of an aluminium alloy 6005A-T6. Acta Mater 2007;55:6133–43.
[43] Chao YJ, Qi X. Thermal and thermomechanical modeling of friction stir welding of aluminum alloy 6061-T6. J Mater Process Manuf Sci 1998;7:215–33.
[44] Zahedul M, Khandkar H, Khan JA. Thermal modeling of overlap friction stir welding for Al-alloys. J Mater Process Manuf Sci 2001;10:91–105.
[45] Song M, Kovacevic R. Thermal modeling of friction stir welding in a moving coordinate system and its validation. Int J Mach Tools Manuf 2003;43:605–15.
[46] Khandkar MZH, Khan JA, Reynolds AP. Prediction of temperature distribution and thermal history during friction stir welding: input torque based model. Sci Technol Weld Join 2003;8(3):165–74.
[47] Soundararajan V, Zekovic S, Kovacevic R. Thermo-mechanical model with adaptive boundary conditions for friction stir welding of Al 6061. Int J Mach Tools Manuf 2005;45:1577–87.
[48] Hamilton C, Dymek S, Sommers A. A thermal model of friction stir welding in aluminium alloys. Int J Mach Tools Manuf 2008;48:1120–30.
[49] Simar A, Lecomte-Beckers J, Pardoen T, de Meester B. Effect of boundary conditions and heat source distribution on temperature distribution in friction stir welding. Sci Technol Weld Join 2006;11(2):170–7.
[50] Frigaard O, Grong O, Midling OT. A process model for friction stir welding of age hardening aluminum alloys. Metal Mater Trans A 2001;32:1189–200.
[51] Shi Q, Dickerson T, Shercliff HR. Thermo-mechanical FE. modelling of friction stir welding of Al-2024 including tool loads. In: Proc 4th int symp FSW 2003, Park City, Utah, USA; 2003.
[52] Mc Cune RW, Ou H, Armstrong CG, Price M. Modelling friction stir welding with the finite element method – a comparative study. In: Proc 5th int symp FSW 2005, Metz, France; 2005.
[53] Tang W, Guo X, McClure JC, Murr LE. Heat input and temperature distribution in friction stir welding. J Mater Process Manuf Sci 1998;7:163–72.
[54] Gallais C, Denquin A, Bréchet Y, Lapasset G. Precipitation microstructures in an AA6056 aluminium alloy after friction stir welding: characterisation and modelling. Mater Sci Eng A 2008;496:77–89.
[55] Hamilton C, Sommers A, Dymek S. A thermal model of friction stir welding applied to Sc-modified Al–Zn–Mg–Cu extrusions. Int J Mach Tools Manuf 2009;49:230–8.
[56] Ferro P, Bonollo F. A semianalytical thermal model for friction stir welding. Metal Mater Trans A 2010;41:440–9.
[57] Schmidt H, Hattel J. Thermal modelling of friction stir welding. Scripta Mater 2008;58:332–7.
[58] Arora A, Zhang Z, De A, DebRoy T. Strains and strain rates during friction stir welding. Scripta Mater 2009;61(9):863–6.
[59] Schmidt H, Hattel J, Wert J. An analytical model for the heat generation in friction stir welding. Model Simul Mater Sci Eng 2004;12:143–57.
[60] Schmidt H, Hattel J, Wert J. Modelling of the contact condition at the tool/matrix interface in friction stir welding. In: Cerjak H, Bhadeshia HKDH, Kozeschnik E, editors. Math model weld phenom, vol. 7. Graz: Maney Publishing; 2005. p. 925–41.
[61] Schmidt H, Hattel J. Modelling heat flow around tool probe in friction stir welding. Sci Technol Weld Join 2005;10(2):176–86.
[62] Heurtier P, Jones MJ, Desrayaud C, Driver JH, Montheillet F, Allehaux D. Mechanical and thermal modelling of friction stir welding. J Mater Process Technol 2006;171:348–57.
[63] Simar A, Pardoen T, de Meester B. Effect of rotational material flow on temperature distribution in friction stir welds. Sci Technol Weld Join 2007;12(4):324–33.
[64] Jacquin D, de Meester B, Simar A, Deloison D, Montheillet F, Desrayaud C. A simple Eulerian thermomechanical modeling of friction stir welding. J Mater Process Technol 2011;211(1):57–65.
[65] Bendzsak GJ, North TH, Smith CB. An experimentally validated 3D model for friction stir welding. In: Proc 2th int symp FSW 2000, Gothenburg, Sweden; 2000.
[66] Shercliff HR, Colegrove PA. Modelling of friction stir welding. In: Cerjak H, Bhadeshia HKDH, editors. Mathematical modeling of weld phenomena 6. Graz: Maney Publishing; 2002. p. 927–74.
[67] Ulysse P. Three-dimensional modeling of the friction stir-welding process. Int J Mach Tools Manuf 2002;42:1549–57.
[68] Seidel TU, Reynolds AP. Two-dimensional friction stir welding process model based on fluid mechanics. Sci Technol Weld Join 2003;8(3):175–83.
[69] Askari A, Silling ST, London B, Mahoney M. Modeling and analysis of friction stir welding process. In: Proc FSW visu modell seminar, GKSS, Germany; 2003.
[70] Colegrove PA, Shercliff HR. Two-dimensional CFD modelling of flow round profiled FSW tooling. Sci Technol Weld Join 2004;9(6):483–92.
[71] Colegrove PA, Shercliff HR. Development of Trivex friction stir welding tool part 1 – two-dimensional flow modelling and experimental validation. Sci Technol Weld Join 2004;9(4):345–51.
[72] Colegrove PA, Shercliff HR. Development of Trivex friction stir welding tool part 2 – three-dimensional flow modelling. Sci Technol Weld Join 2004;9(4):352–61.
[73] Colegrove PA, Shercliff HR. Modelling the friction stir welding of aerospace alloys. In: Proc 5th int symp FSW 2004, Metz, France; 2004.

[74] Colegrove PA, Shercliff H. 3-Dimensional CFD modelling of flow round a threaded friction stir welding tool profile. J Mater Process Technol 2005;169(2):320–7.
[75] Colegrove PA, Shercliff HR, Zettler R. Model for predicting heat generation and temperature in friction stir welding from the material properties. Sci Technol Weld Join 2007;12(4):284–97.
[76] Nandan R, Roy GG, DebRoy T. Numerical simulation of three-dimensional heat transfer and plastic flow during friction stir welding. Metal Mater Trans A 2006;37:1247–59.
[77] Bastier A, Maitournam MH, Dang Van K, Roger F. Steady state thermomechanical modelling of friction stir welding. Sci Technol Weld Join 2006;11(3):278–88.
[78] Bastier A, Maitournam MH, Roger F, Dang Van K. Modelling of the residual state of friction stir welded plates. J Mater Process Technol 2008;200:25–37.
[79] De Vuyst T, Madhavan V, Ducoeur B, Simar A, de Meester B, D'Alvise L. A thermo-fluid modelling approach for computing temperature cycles and residual stresses in FSW. In: Proc 7th int symp FSW 2008, Japan; 2008.
[80] Kim D, Badarinarayan H, Kim JH, Kim C, Okamoto K, Wagoner RH, et al. Numerical simulation of friction stir butt welding process for AA5083-H18 sheets. Eur J Mech Solids 2010;29:204–15.
[81] Xu S, Deng X, Reynolds AP, Seidel TU. Finite element simulation of material flow in friction stir welding. Sci Technol Weld Join 2001;6(3):191–3.
[82] Fourment L, Guerdoux S, Miles M, Nelson T. Numerical simulation of the friction stir welding process using both Lagrangian and Arbitrary Lagrangian Eulerian formulations. In; Proc 5th int symp FSW 2005, Metz, France; 2005.
[83] Guerdoux S, Fourment L. A 3D numerical simulation of different phases of friction stir welding. Model Simul Mater Sci Eng 2009;17(7):075001.
[84] Assidi M, Fourment L, Guerdoux S, Nelson T. Friction model for friction stir welding process simulation: calibrations from welding experiments. Int J Machine Tools Manuf 2010;50:143–55.
[85] Buffa G, Hua J, Shivpuri R, Fratini L. A continuum based FEM model for friction stir welding-model development. Mater Sci Eng A 2006;419:389–96.
[86] Schmidt H, Hattel J. A local model for the thermomechanical conditions in friction stir welding. Model Simul Mater Sci Eng 2005;13(1):77–93.
[87] Schmidt H, Hattel J. Analysis of the velocity field in the shear layer in FSW – experimental and numerical modelling. In: Proc 6th int symp FSW 2006, Saint-Sauveur, Canada; 2006.
[88] Zhang HW, Zhang Z, Chen JT. 3D modeling of material flow in friction stir welding under different process parameters. J Mater Process Technol 2007;183:62–70.
[89] Tartakovsky AM, Grant G, Sun X, Tae Hong S, Khaleel M. Smooth particle hydrodynamics (SPH) model for friction stir welding (FSW) of dissimilar materials. In: Proc 6th int symp FSW 2006, Saint-Sauveur, Canada; 2006.
[90] Sheppard T, Wright DS. Determination of flow stress. Metal Technol 1979;6:215–23.
[91] Colegrove P, Painter M, Graham D, Miller T. Three-dimensional flow and thermal modelling of the friction stir welding process. In: Proc 2nd int symp FSW 2000, Gothenburg, Sweden; 2000.
[92] De Vuyst T, D'Alvise L, Simar A, de Meester B, Pierret S. Finite element modeling of friction stir welding of aluminium alloy plates-inverse analysis using a genetic algorithm. Weld World 2005;49(3/4):47–55.
[93] ABAQUS. User's manual, version 6.3. Providence, RI; 2002.
[94] Rosakis P, Rosakis AJ, Ravichandran G, Hodowany J. A thermodynamic internal variable model for the partition of plastic work into heat and stored energy in metals. J Mech Phys Solids 2000;48(3):581–607.
[95] Dong P, Lu F, Hong JK, Cao Z. Coupled thermomechanical analysis of friction stir welding process using simplified models. Sci Technol Weld Join 2001;6(5):281–7.
[96] Lambrakos SG, Fonda RW, Milewski JO, Mitchell JE. Analysis of friction stir welds using thermocouple measurements. Sci Technol Weld Join 2003;8(5):385–90.
[97] Davis JR, Allen P, Lampman SR, Zorc TB, Henry SD, Daquila JL, et al. Metals handbook. Properties and selection: nonferrous alloys and special-purpose materials, vol. 2. OH: ASM International; 1990.
[98] Juvinall RC, Marshek KM. Fundamentals of machine component design. 2nd ed. New York: John Wiley and Sons; 1991.
[99] Miao WF, Laughlin DE. Precipitation hardening in aluminum alloy 6022. Scripta Mater 1999;40(7):873–8.
[100] Dutta I, Allen SM. A calorimetric study of precipitation in commercial aluminium alloy 6061. J Mater Sci Lett 1991;10:323–6.
[101] Gupta AK, Lloyd DJ. The precipitation in a super purity Al–Mg–Si alloy. In: 3rd int conf aluminium alloys 1992, Trondhiem, Norway; 1992.
[102] Edwards GA, Stiller K, Dunlop GL, Couper MJ. The precipitation sequence in Al–Mg–Si alloys. Acta Mater 1998;46(11):3893–904.
[103] Gupta AK, Lloyd DJ, Court SA. Precipitation hardening processes in an Al–0.4%Mg–1.3%Si–0.25%Fe aluminum alloy. Mater Sci Eng A 2001;301:140–6.
[104] Miao WF, Laughlin DE. Effects of Cu content and pre-aging on precipitation characteristics in aluminum alloy 6022. Metal Mater Trans A 2000;31:361–71.
[105] Esmaeili S, Wang X, Lloyd DJ, Poole WJ. On the precipitation-hardening behavior of the Al–Mg–Si–Cu alloy AA6111. Metal Mater Trans A 2003;34:751–63.
[106] Chakrabarti DJ, Laughlin DE. Phase relations and precipitation in AlMgSi alloys with Cu additions. Prog Mater Sci 2004;49:389–410.
[107] Sagalowicz L, Lapasset G, Hug G. Transmission electron microscopy of a precipitate which forms in the Al–Mg–Si system. Philos Mag Lett 1996;74:57–66.
[108] Dif R, Warner T, Bechet D, Ribes H. 6056-T78: a corrosion resistant copper-rich 6xxx alloy for aerospace applications. In: ICAA 6 conference on aluminium alloys: their physical and mechanical properties 1998, Toyohashi, Japan; 1998.
[109] Marioara CD, Andersen SJ, Janssen J, Zandbergen HW. Atomic model for GP-zones in a 6082 Al–Mg–Si system. Acta Mater 2001;49:321–8.
[110] Marioara CD, Andersen SJ, Zandbergen HW, Holmestad R. The influence of alloy composition on precipitates of the Al–Mg–Si system. Metal Mater Trans A 2005;36A:691–702.

[111] Cuniberti A, Tolley A, Castro Riglos MV, Giovachini R. Influence of natural aging on the precipitation of an AlMgSi alloy. Mater Sci Eng A 2010;527:5307–11.
[112] Anderson SJ, Zandbergen HW, Jansen J, Traeholt C, Tundal U, Reiso O. The crystal structure of the β'' phase in Al–Mg–Si alloys. Acta Mater 1998;46(9):3283–98.
[113] Murayama M, Hono K. Pre-precipitate clusters and precipitation processes in Al–Mg–Si alloys. Acta Mater 1998;47:1537–48.
[114] Matsuda K, Sakaguchi Y, Miyata Y, Uteni Y, Sato T, Kamio A, et al. Precipitation sequence of various kinds of metastable phases in Al–1.0 mass% Mg2Si–0.4 mass% Si alloy. J Mater Sci 2000;35:179–89.
[115] Lynch JP, Brown LM, Jacobs MH. Microanalysis of age-hardening precipitates in aluminium alloys. Acta Metal 1982;30:1389–95.
[116] Westengen H, Ryum N. Precipitation reactions in an aluminium 1 wt.% Mg_2Si alloy. Zeitschrift Fur Metallkunde 1979;70:528–35.
[117] Burger GB, Gupta AK, Jeffrey PW, Lloyd DJ. Microstructural control of aluminum sheet used in automotive applications. Mater Charact 1995;35:23–39.
[118] Olea CAW, Roldo L, dos Santos JF, Strohaecker TR. A sub-structural analysis of friction stir welded joints in an AA6056 Al-alloy in T4 and T6 temper conditions. Mater Sci Eng A 2007;454–455:52–62.
[119] Simar A. A multiscale multiphysics investigation of aluminum friction stir welds – from thermal modelling to mechanical properties through precipitation evolution and hardening. PhD thesis 2007, Université catholique de Louvain, Louvain-la-Neuve, Belgium; 2007.
[120] Lohne O, Dons AL. Quench sensitivity in aluminum–magnesium–silicon alloys containing manganese or chromium. Scand J Met 1983;12:34–6.
[121] Es-Said OS, Morris JG, Merchant HD. Homogenization and annealing of aluminium and copper alloys. In: Merchant HD, Crane J, Chia EH, editors. Warrendale. PA: TMS; 1988. p. 183–207.
[122] Shercliff HR, Ashby MF. A process model for age hardening of aluminium alloys-I. The model. Acta Metal Mater 1990;38:1789–802.
[123] Shercliff HR, Ashby MF. A process model for age hardening of aluminium alloys-II. Applications of the model. Acta Metal Mater 1990;38:1803–12.
[124] Myhr OR, Grong O. Process modelling applied to 6082-T6 aluminium weldments-I. Reaction kinetics. Acta Metal Mater 1991;39(11):2693–702.
[125] Midling OT, Grong O. A process model for friction stir welding of Al–Mg–Si alloys and Al–SiC metal matrix composites-II. HAZ microstructure and strength evolution. Acta Metal Mater 1994;42(5):1611–22.
[126] Bratland DH, Grong O, Shercliff H, Myhr OR, Tjotta S. Modelling of precipitation reactions in industrial processing. Acta Mater 1997;45(1):1–22.
[127] Bjorneklett BI, Grong O, Myhr OR, Kluken AO. A process model for the heat-affected zone of microstructure evolution in Al–Zn–Mg weldments. Metal Mater Trans A 1999;30:2667–77.
[128] Russell MJ, Sherciff HR. Analytical modelling of microstrcture development in friction stir welding. In: Proc 1st int symp FSW 1999, Thousand Oaks, USA; 1999.
[129] Esmaeili S, Lloyd DJ, Poole WJ. Modeling of precipitation hardening for the naturally aged Al–Mg–Si–Cu alloy AA6111. Acta Mater 2003;51:3467–81.
[130] Esmaeili S, Lloyd DJ, Poole WJ. A yield strength model for the Al–Mg–Si–Cu alloy AA6111. Acta Mater 2003;51:2243–57.
[131] Wang X, Poole WJ, Esmaeili S, Lloyd DJ, Embury JD. Precipitation strengthening of the aluminum alloy AA6111. Metal Mater Trans A 2003;34:2913–24.
[132] Starink MJ, Wang SC. A model for the yield strength of overaged Al–Zn–Mg–Cu alloys. Acta Mater 2003;51:5131–50.
[133] Esmaeili S, Lloyd DJ. Modeling of precipitation hardening in pre-aged AlMgSi(Cu) alloys. Acta Mater 2005;53:5257–71.
[134] Lopez R, Ducoeur B, Chiumenti M, de Meester B, Agelet de Saracibar C. Modeling precipitate dissolution in hardened aluminium alloys using neural networks. Int J Mater Form 2008;Suppl. 1:1291–4.
[135] Yazdanmehr M, Bahrami A, Mousavi Anijdan SH. A precipitation-hardening model for non-isothermal ageing of Al–Mg–Si alloys. Comput Mater Sci 2009;45:385–7.
[136] Christian JW. The theory of phase transformations in metals and alloys, part I. Oxford: Pergamon Press; 1975.
[137] Myhr OR, Grong O. Process modelling applied to 6082-T6 aluminium weldments-II. Applications of model. Acta Metal Mater 1991;39(11):2703–8.
[138] Wagner R, Kampmann R. Phase transformation in materials of materials science and technology. In: Cahn RW, Haasen P, Kramer EJ, editors. Materials science and technology, vol. 5. Germany: VCH; 1991. p. 213–303. 7th ed., chapter 4.
[139] Deschamps A, Bréchet Y. Influence of predeformation and ageing of an Al–Zn–Mg alloy-II. Modeling of precipitation kinetics and yield stress. Acta Mater 1999;47:293–305.
[140] Myhr OR, Grong O. Modelling of non-isothermal transformations in alloys containing a particle distribution. Acta Mater 2000;48:1605–15.
[141] Myhr OR, Grong O, Andersen SJ. Modelling of the age hardening behaviour of Al–Mg–Si alloys. Acta Mater 2001;49:65–75.
[142] Myhr OR, Grong O, Klokkehaug S, Fjaer HG. Modelling of the microstructure and strength evolution during ageing and welding of Al–Mg–Si alloys. In: Bhadeshia HKDH, editor. Mathematical modelling of weld phenomena, vol. 6. London: Manley Publishing; 2002.
[143] Robson JD, Prangnell PB. Dispersoïd precipitation and process modelling in zirconium containing commercial aluminium alloys. Acta Mater 2001;49:599–613.
[144] Liu HJ, Fujii H, Maeda M, Nogi K. Comparative study on fracture locations of friction stir welded joints for different types of aluminum alloys. In: Proc 4th int symp FSW 2003, Park City, Utah, USA; 2003.
[145] Robson JD, Jones MJ, Prangnell PB. Extension of the N-model to predict competing homogeneous and heterogeneous precipitation in Al–Sc alloys. Acta Mater 2003;51:1453–68.
[146] Nicolas M, Deschamps A. Characterisation and modelling of precipitate evolution in an Al–Zn–Mg alloy during non-isothermal heat treatments. Acta Mater 2003;51:6077–94.

[147] Myhr OR, Grong O, Fjaer HG, Marioara CD. Modelling of the microstructure and strength evolution in Al–Mg–Si alloys during multistage thermal processing. Acta Mater 2004;52:4997–5008.
[148] Robson JD. A new model for prediction of dispersoïd precipitation in aluminium alloys containing zirconium and scandium. Acta Mater 2004;52:1409–21.
[149] Kamp N, Sullivan A, Tomasi R, Robson JD. Modelling of heterogeneous precipitate distribution evolution during friction stir welding process. Acta Mater 2006;54:2003–14.
[150] Khan IN, Starink MJ, Yan JL. A model q for precipitation kinetics and strengthening in Al–Cu–Mg alloys. Mater Sci Eng A 2008;472:66–74.
[151] Perez M, Dumont M, Acevedo-Reyes D. Implementation of classical nucleation and growth theories for precipitation. Acta Mater 2008;56:2119–32.
[152] Gouttebroze S, Mo A, Grong O, Pedersen KO, Fjaer HG. A new constitutive model for the finite element simulation of local hot forming of aluminum 6xxx alloys. Metal Mater Trans A 2008;39:522–34.
[153] Fazeli F, Sinclair CW, Bastow T. the role of excess vacancies on precipitation kinetics in Al–Mg–Sc alloys. Metal Mater Trans A 2008;39:2297–305.
[154] Rollett AD, Manohar P. The Monte Carlo method. In: Raabe D, Roters F, Barlat F, Chen L-Q, editors. Continuum scale simulation of engineering materials. Germany: Weinheim; 2004. p. 7–114.
[155] Reinhard P-G, Suraud E. Introduction to cluster dynamics. Germany: Wiley; 2004.
[156] Porter DA, Easterling KE. Phase transformations in metals and alloys. 2nd ed. Taylor and Francis; 2004.
[157] Godard D. Influences de la précipitation sur le comportement thermomécanique lors de la trempe d'un alliage Al–Zn–Mg–Cu. PhD thesis, Institut polytechnique de Lorraine; 1999.
[158] Maugis P, Gouné M. Kinetics of vanadium carbonitrite precipitation in steel: A computer model. Acta Mater 2005;53:3359–67.
[159] Fazeli F, Poole WJ, Sinclair CW. Modeling the effect of Al_3Sc precipitates on the yield stress and work hardening of an Al–Mg–Sc alloy. Acta Mater 2008;56:1909–18.
[160] Gupta AK, Lloyd DJ, Court SA. Precipitation hardening in Al–Mg–Si alloys with and without excess Si. Mater Sci Eng A 2001;316:11–7.
[161] Poole WJ, Wang X, Lloyd DJ, Embury JD. The shearable–non-shearable transition in Al–Mg–Si–Cu precipitation hardening alloys: implications on the distribution of slip, work hardening and fracture. Philos Mag 2005;85(26–27):3113–35.
[162] Song M. Modeling the hardness and yield strength evolutions of aluminium alloy with rod/needle-shaped precipitates. Mater Sci Eng A 2007;443:172–7.
[163] Zhu AW, Starke EA. Strengthening effect of unshearable particles of finite size: a computer experimental study. Acta Mater 1999;46:3263–9.
[164] Wang SC, Lefebvre F, Yan JL, Sinclair I, Starink MJ. VPPA welds of Al-2024 alloys: Analysis and modelling of local microstructure and strength. Mater Sci Eng A 2006;431:123–36.
[165] Hall EO. The deformation and ageing of mild steel: III discussion of results. Proc Phys Soc B London 1951;64:747.
[166] Petch NJ. The cleavage strength of polycrystals. J Iron Steel Inst 1953;174:25–8.
[167] Starink MJ, Deschamps A, Wang SC. the strength of friction stir welded and friction stir processed aluminium alloys. Scripta Mater 2008;58:377–82.
[168] Hofmann DC, Vecchio KS. Thermal history analysis of friction stir processed and submerged friction stir processed aluminum. Mater Sci Eng A 2007;465:165–75.
[169] Nabarro FRN. Theory of crystal dislocations. Oxford: University Press; 1967.
[170] Gerold V. Precipitation hardening. In: Nabarro FRN, editor. Dislocations in solids, vol. 4. Amsterdam: North-Holland; 1979. p. 234.
[171] Ardell AJ. Precipitation hardening. Metal Mater Trans A 1985;16:2131–65.
[172] Nembach E. Order strengthening: recent developments, with special reference to aluminiumlithium-alloys. Prog Mater Sci 2000;45(4):275–338.
[173] Friedel J. Dilocations. Oxford: Pergamon Press; 1964.
[174] Brown LM, Ham RK. Strengthening methods in crystals. New York: John Wiley and Sons; 1971.
[175] Mecking H, Kocks UF. Kinetics of flow and strain-hardening. Acta Metal 1981;29:1865–75.
[176] Estrin Y, Mecking H. A unified phenomenological description of work hardening and creep based on one-parameter models. Acta Metal 1984;32(1):57–80.
[177] Kocks UF, Mecking H. Physics and phenomenology of strain hardening: the FCC case. Prog Mater Sci 2003;48:171–273.
[178] Voce E. Practical strain-hardening function. Acta Metal 1955;51:21926.
[179] Deschamps A, Bréchet Y, Necker CJ, Saimoto S, Embury JD. Study of large strain deformation of dilute solid solutions of Al–Cu using channel-die compression. Mater Sci Eng A 1996;207:143–52.
[180] Deschamps A, Esmaeili S, Poole WJ, Militzer M. Strain hardening in relation to microstructure in precipitation hardening materials. J Phys IV France 2000;10:151–6.
[181] Esmaeili S, Cheng LM, Deschamps A, Lloyd DJ, Poole WJ. The deformation behaviour of AA6111 as a function of temperature and precipitation state. Mater Sci Eng A 2001;319–321:461–5.
[182] Cheng LM, Poole WJ, Embury JD, Lloyd DJ. The influence of precipitation on the work-hardening behavior of the aluminum alloys AA6111 and AA7030. Metal Mater Trans A 2003;34:2473–81.
[183] Fribourg G, Bréchet Y, Deschamps A, Simar A. Microstructure-based modelling of isotropic and kinematic strain hardening in a precipitation hardening aluminium alloy. Acta Mater 2011;59:3621–35.
[184] Dumont D, Deschamps A, Bréchet Y. On the relationship between microstructure, strength and toughness in AA7050 aluminium alloy. Mater Sci Eng A 2003;356:326–36.
[185] Westermann I, Hopperstad OS, Marthinsen K, Holmedal B. Ageing and work-hardening behaviour of a commercial AA7108 aluminium alloy. Mater Sci Eng A 2009;524:151–7.
[186] Deschamps A, Nieuwczas M, Bley F, Bréchet Y, Embury JD, Le Sinq L, et al. Low-temperature dynamic precipitation in a supersaturated Al–Zn–Mg alloy and related strain hardening. Philos Mag A 1999;79(10):2485–504.
[187] Marthinsen K, Nes E. A general model for metal plasticity. Mater Sci Eng A 1997;234–236:1095–8.

[188] Nes E. Modelling of work hardening and stress saturation in FCC metals. Prog Mater Sci 1998;41:129–93.
[189] Nes E, Pettersen T, Marthinsen K. On the mechanism of work hardening and flow stress saturation. Scripta Mater 2000;43:55–62.
[190] Marthinsen K, Nes E. Modelling strain hardening and steady state deformation of Al–Mg alloys. Mater Sci Technol 2001;17:376–88.
[191] Nes E, Marthinsen K, Ronning B. Modelling the evolution in microstructure and properties during processing of aluminium alloys. J Mater Process Technol 2001;117:333–40.
[192] Nes E, Marthinsen K. Modeling the evolution in microstructure and properties during plastic deformation of fcc-metals and alloys – an approach towards a unified model. Mater Sci Eng A 2002;322:176–93.
[193] Roters F, Raabe D, Gottstein G. Work hardening in heterogeneous alloys – a microstructural approach based on three internal state variables. Acta Mater 2000;48:4181–9.
[194] Goerdeler M, Gottstein G. A microstructural work hardening model based on three internal state variables. Mater Sci Eng A 2001;309–310:377–81.
[195] Goerdeler M, Crumbach M, Schneider M, Gottstein G, Neumann L, Aretz H, et al. Dislocation density based modeling of work hardening in the context of integrative modeling of aluminium processing. Mater Sci Eng A 2004;387–389:266–371.
[196] Estrin Y. Dislocation-density-related constitutive modeling. In: Krausz AS, Krausz K, editors. Unified constitutive laws of plastic deformation. San Diego: Academic Press; 1996. p. 9–106.
[197] Barlat F, Glazov MV, Brem JC, Lege DJ. A simple model for dislocation behavior, strain and strain arte hardening evolution in deforming aluminium alloys. Int J Plasticity 2002;18:919–39.
[198] Poole WJ, Lloyd DJ. Modelling the stress–strain behaviour of aluminium alloy AA6111. In: Nie JF, Morton AJ, Muddle BC, Inst Mater Eng Australasia Ltd., editors. Proc 9th int conf Al alloys; 2004.
[199] Reynolds AP, Baxter SC. Kinematic hardening in a dispersion strengthened aluminum alloy: experiment and modeling. Mater Sci Eng A 2000;285:265–79.
[200] Proudhon H, Poole WJ, Wang X, Bréchet Y. The role of internal stresses on the plastic deformation of the Al–Mg–Si–Cu alloy AA6111. Philos Mag 2008;88(5):621–40.
[201] Teixeira JD, Bourgeois L, Sinclair CW, Hutchinson CR. The effect of shear resistant, plate-shaped precipitates on the work hardening of Al alloys: towards a prediction of the strength-elongation correlation. Acta Mater 2009;57:6075–89.
[202] Bréchet Y, Louchet F. On the stability of Orowan loops around coherent spherical ordered precipitates. Acta Metal 1989;37(9):2469–73.
[203] Argon AS, Haasen P. A new mechanism of work hardening in the late stages of large strain plastic flow in FCC and diamond cubic crystals. Acta Mater 1993;390(41):3289–306.
[204] Liu YL. A study on flow stress of AlSiC composites deformed in a large range of strain. Scripta Mater 1996;35:2539.
[205] Gurson AL. Continuum theory of ductile rupture by void nucleation and growth: part I – yield criteria and flow rules for porous ductile media. J Eng Mater Technol 1977;99:2–15.
[206] Broek D. The role of inclusions in ductile fracture and fracture toughness. Eng Fract Mech 1973;5:55–66.
[207] Huber G, Bréchet Y, Pardoen T. Predictive model for void nucleation and void growth controlled ductility in quasi-eutectic cast aluminium alloys. Acta Mater 2005;53:2739–49.
[208] Asserin Lebert A, Besson J, Gourgues AF. Fracture of 6056 aluminium sheet materials: effect of specimen thickness and hardening behavior on strain localization and toughness. Mater Sci Eng A 2005;395:186–94.
[209] Liu G, Sun J, Nan CW, Chen KH. Experiment and multiscale modeling of the coupled influence of constituents and precipitates on the ductile fracture of heat-treatable aluminum alloys. Acta Mater 2005;53(12):3459–68.
[210] Liu G, Zhang GJ, Wang RH, Hu W, Sun J, Chen KH. Heat treatment-modulated coupling effect of multi-scale second-phase particles on ductile fracture of aged aluminum alloys. Acta Mater 2007;55:273–84.
[211] Kuijpers NCW, Kool WH, Koenis PTG, Nilsen KE, Todd I, van der Zwaag S. Assessment of different techniques for quantification of α-Al(FeMn)Si and β-AlFeSi intermetallics in AA 6xxx alloys. Mater Charact 2003;49:409–20.
[212] Kuijpers NCW, Kool WH, van der Zwaag S. DSC study on Mg–Si phases in as cast AA6xxx. Mater Sci Forum 2002;396–402:675–80.
[213] Hirasawa H. Precipitation process of Al–Mn and Al–Cr supersaturated solid solution in presence of age hardening phases. Scr Metal 1975;9:955–8.
[214] Lodgaard L, Ryum N. Precipitation of dispersoids containing Mn and/or Cr in Al–Mg–Si alloys. Mater Sci Eng A 2000;283:144–52.
[215] Pineau A. Review of fracture micromechanisms and a local approach to predicting crack resistance in low strength steels. In: Francois D et al., editor. Advances in fracture research, Proc ICF 5. Cannes, France: Pergamon; 1981. p. 553–77.
[216] Tvergaard V. Material failure by void growth to coalescence. Adv Appl Mech 1990;27:83151.
[217] Rice JR, Tracey DM. On the ductile enlargement of voids in triaxial stress. J Mech Phys Solids 1969;17:201–17.
[218] Argon AS, Im J, Safoglu R. Cavity formation from inclusions in ductile fracture. Metal Trans A 1975;6:825–37.
[219] Urreta SE, Louchet F, Ghilarducci. Fracture behaviour of an Al–Mg–Si industrial alloy. Mater Sci Eng A 2001;302:300–7.
[220] Thomason PF. Ductile fracture of metals. Oxford: Pergamon Press; 1990.
[221] Tvergaard V. Ductile fracture by cavity nucleation between larger voids. J Mech Phys Solids 1982;30:265–86.
[222] Faleskog J, Shih CF. Micromechanics of coalescence – I. Synergistic effects of elasticity, plastic yielding and multi-size-scale voids. J Mech Phys Solids 1997;45:21–50.
[223] Fabrègue D, Pardoen T. A constitutive model for elasticplastic solids containing primary and secondary voids. J Mech Phys Solids 2008;56:719–41.
[224] Fabrègue D, Pardoen T. Corrigendum to ‘‘A constitutive model for elasticplastic solids containing primary and secondary voids’’. J Mech Phys Solids 2009;57:869–70.
[225] Pardoen T, Dumont D, Deschamps A, Bréchet Y. Grain boundary versus transgranular ductile failure. J Mech Phys Solids 2003;51:637–65.
[226] Steglich D, Brocks W, Heerens J, Pardoen T. Anisotropic ductile fracture of Al 2024 alloys. Eng Fract Mech 2008;75(12):3692–706.

[227] Pardoen T, Hutchinson JW. An extended model for void growth and coalescence. J Mech Phys Solids 2000;48:2467–512.
[228] Pardoen T, Hutchinson JW. Micromechanics-based model for trends in toughness of ductile metals. Acta Mater 2003;51:133–48.
[229] Tvergaard V. On localization in ductile materials containing voids. Int J Fract 1982;18:237–51.
[230] Needleman A, Tvergaard V. An analysis of ductile rupture in notched bars. J Mech Phys Solids 1984;32:461–90.
[231] Gologanu M, Leblond JB, Perrin G, Devaux J. Recent extensions of Gurson's model for porous ductile metals. In: Suquet P, editor. Continuum micromechanics. Berlin: Springer-Verlag; 1995. p. 61–106.
[232] Eshelby JD. The determination of the elastic field of an ellipsoidal inclusion and related problems. Proc Roy Soc London, Ser A 1957;241:376–96.
[233] Berveiller M, Zaoui A. An extension of the self-consistent scheme to plastically flowing polycrystals. J Mech Phys Solids 1979;26:325–40.
[234] Beremin FM. Cavity formation from inclusions in ductile fracture of A508 steel. Metal Trans A 1981;12:723–31.
[235] Berdin C. Damage evolution laws and fracture criteria. In: Besson J, editor. Local approach to fracture, Paris; 2004. p. 147–74.
[236] Tekoğlu C, Pardoen T. A micromechanics based damage model for composite materials. Int J Plasticity 2010;26(4):549–69.
[237] Pardoen T. Numerical simulation of low stress triaxiality ductile fracture. Comput Struct 2006;84(26–27):1641–50.
[238] Lecarme L, Tekoglu C, Pardoen T. Void growth and coalescence in ductile solids with stage III and stage IV strain hardening. Int J Plasticity, in press, doi:10.1016/j.ijplas.2011.01.004.
[239] Scheyvaerts F, Pardoen T, Onck PR. A new model for void coalescence by internal necking. Int J Damage Mech 2010;19(1):95–126.
[240] Scheyvaerts F, Onck PR, Tekoglu C, Pardoen T. The growth and coalescence of ellipsoidal voids in plane strain under combined shear and tension. J Mech Phys Solids 2011;59(2):373–97.
[241] Bron F, Besson J, Pineau A. Ductile rupture in thin sheets of two grades of 2024 aluminum alloy. Mater Sci Eng 2004;380A:356–64.
[242] Morgeneyer TF, Besson J, Proudhon H, Starink MJ, Sinclair I. Experimental and numerical analysis of toughness anisotropy in AA2139 Al-alloy sheet. Acta Mater 2009;57:3902–15.
[243] Shabrov MN, Sylven E, Kim S, Sherman DH, Chuzhoy L, Briant CL, et al. Void nucleation by inclusion cracking. Metal Mater Trans A 2004;35:1745–55.
[244] Lassance D, Scheyvaerts F, Pardoen T. Growth and coalescence of penny-shaped voids in metallic alloys. Eng Fract Mech 2006;73(8):1009–34.
[245] Simar A, Bréchet Y, de Meester B, Denquin A, Pardoen T. Microstructure, local and global mechanical properties of friction stir welds in aluminium alloy 6005A-T6. Mater Sci Eng A 2008;486:85–95.
[246] Frigaard O, Grong O, Bjorneklett B, Midling O. Modelling of the thermal and microstructure fields during friction stir welding of aluminium alloys. In: Proc 1st int symp FSW 1999, Thousand Oaks, California, USA; 1999.
[247] Colegrove PA, Shercliff HR. Experimental and numerical analysis of aluminium alloy 7075-T7351 friction stir welds. Sci Technol Weld Join 2003;8(5):360–8.
[248] Hill R. A theory of the yielding and plastic flow of anisotropic metals. Proc Roy Soc London 1948;193:281–97.
[249] Staron P, Kocak M, Williams S. Residual stresses in friction stir welded Al sheets. Appl Phys A 2002;74:S1161–2.
[250] Luan G, Li G, Li C, Dong C. DC-LSND friction stir welding. In: Proc 7th int symp FSW 2008, Awaji Island, Japan; 2008.
[251] Richards DG, Prangnell PB, Withers PJ, Williams SW, Nagy T, Morgan S. Efficacy of active cooling for controlling residual stresses in friction stir welds. Sci Technol Weld Join 2010;15(2):156–65.
[252] Dumolt SD, Laughlin DE, Williams JC. Formation of a modified β' phase in aluminium alloy 6061. Scripta Metal 1984;18:1347–50.
[253] Heinz B, Skrotzki B. Characterization of a friction-stir-welded aluminum alloy 6013. Metal Mater Trans B 2002;33(3):489–98.
[254] Elangovan K, Balasubramanian V. Influences of post-weld heat treatment on tensile properties of friction stir-welded AA6061 aluminum alloy joints. Mater Character 2008;59(9):1168–77.
[255] Deschamps A, Bley F, Livet F, Fabrègue D, David L. In-situ small-angle X-ray scattering study of dynamic precipitation in an Al–Zn–Mg–Cu alloy. Philos Mag 2003;83(6):677–92.
[256] Zhang Z, Zhang HW. The simulation of residual stresses in friction stir welds. J Mech Mater Struct 2007;2(5):951–64.
[257] Qin XL, Michaleris P. Elasto-visco-plastic analysis of welding residual stress. Sci Technol Weld Join 2009;14(7):606–15.
[258] Fratini L, Macaluso G, Pasta S. Residual stresses and FCP prediction in FSW through a continuous FE model. J Mater Process Technol 2009;15–16:5465–74.
[259] Xia L, Shih CF. Ductile crack growth. 1. A numerical study using computational cells with microstructurally-based length scales. J Mech Phys Solids 1995;43(2):233–59.
[260] Negre P, Steglich D, Brocks W. Crack extension in aluminium welds: a numerical approach using the Gurson–Tvergaard–Needleman model. Eng Fract Mech 2004;71:2365–83.
[261] Karabin ME, Barlat F, Shuey RT. Finite element modeling of plane strain toughness for 7085 aluminum alloy. Metal Mater Trans A 2009;40A:354–76.
[262] Golestaneh AF, Ali A, Zadeh M. Modelling the fatigue crack growth in friction stir welded joint of 2024-T351 Al alloy. Mater Des 2009(September):2928–37.
[263] Lim S, Kim S, Lee CG, Kim S. Stress corrosion cracking behavior of friction-stir-welded Al 6061-T651. Metal Mater Trans A 2005;36:1977–80.
[264] Blanc C, Freulon A, Lafont M-C, Kihn Y, Mankowski G. A Modelling the corrosion behaviour of Al2CuMg coarse particles in copper-rich aluminium alloys. Corrosion Sci 2006;48:3838–51.